JOINT TRANSPORTATION
RESEARCH PROGRAM
INDIANA DEPARTMENT OF TRANSPORTATION
AND PURDUE UNIVERSITY

Full-Scale Dynamic Wireless Power Transfer and Pilot Project Implementation

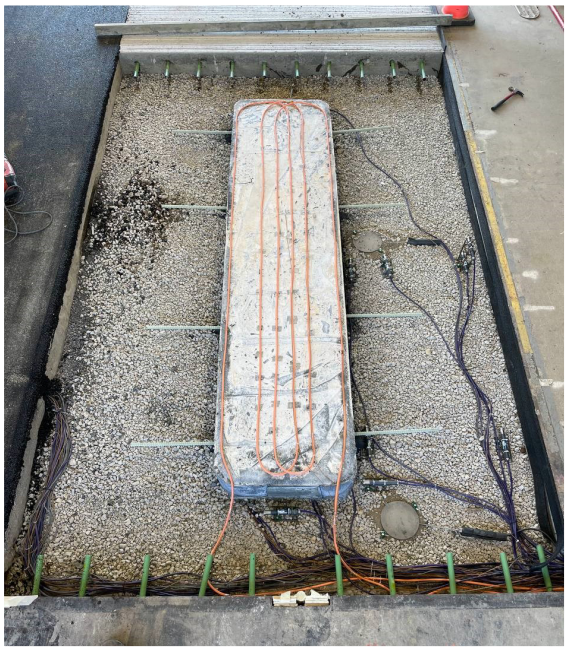

Oscar Andrés Moncada, Zainab Imran, Connor Vickers, Konstantina Gkritza, Steven Pekarek, Dionysios Aliprantis, Aaron Brovont, Behnam Jahangiri, John E. Haddock

SPR-4607 • Report Number: FHWA/IN/JTRP-2024/11 • DOI: 10.5703/1288284317744

RECOMMENDED CITATION

Moncada, O. A., Imran, Z., Vickers, C., Gkritza, K., Pekarek, S., Aliprantis, D., Brovont, A., Jahangiri, B., & Haddock, J. E. (2024). *Full-scale dynamic wireless power transfer and pilot project implementation* (Joint Transportation Research Program Publication No. FHWA/IN/JTRP-2024/11). West Lafayette, IN: Purdue University. https://doi.org/10.5703/1288284317744

AUTHORS

Oscar Andrés Moncada
Graduate Research Assistant
Lyles School of Civil Engineering
Purdue University

Zainab Imran
Graduate Research Assistant
Elmore Family School of Electrical and Computer Engineering
Purdue University

Connor Vickers
Graduate Research Assistant
Elmore Family School of Electrical and Computer Engineering
Purdue University

Konstantina Gkritza, PhD
Professor of Civil Engineering and Agricultural and Biological Engineering
Lyles School of Civil Engineering
Purdue University

Dionysios Aliprantis
Professor of Electrical and Computer Engineering
Elmore Family School of Electrical and Computer Engineering
Purdue University

Aaron Brovont
Research Assistant Professor
Elmore Family School of Electrical and Computer Engineering
Purdue University

Behnam Jahangiri
Post Doctoral Research Assistant
Lyles School of Civil Engineering
Purdue University

John E. Haddock, PhD, PE
Professor of Civil Engineering
Director of the Indiana Local Technical Assistance Program
Lyles School of Civil Engineering
(765) 496-3996
jhaddock@purdue.edu
Corresponding Author

Steven Pekarek, PhD
Dr. Edmund O. Schweitzer, III Professor of Electrical and Computer Engineering
Elmore Family School of Electrical and Computer Engineering
Purdue University

JOINT TRANSPORTATION RESEARCH PROGRAM

The Joint Transportation Research Program serves as a vehicle for INDOT collaboration with higher education institutions and industry in Indiana to facilitate innovation that results in continuous improvement in the planning, design, construction, operation, management and economic efficiency of the Indiana transportation infrastructure. https://engineering.purdue.edu/JTRP/index_html

Published reports of the Joint Transportation Research Program are available at http://docs.lib.purdue.edu/jtrp/.

NOTICE

ACKNOWLEDGMENTS

This research project was enabled by the support from the Joint Transportation Research Program (JTRP), the Indiana Department of Transportation (INDOT), and ASPIRE—an Engineering Research Center program by the National Science Foundation (NSF), grant no. EEC-1941524. The team extends its appreciation to all ASPIRE members whose collective efforts have substantially contributed to the development of this project, with special recognition to Behnam Jahangiri, Robert Swanson, Vatan Mehar, and Anthony Agostino. Additional gratitude is extended to the University of Texas El Paso (UTEP) team for their work on the finite element models this study was based on, with special thanks extended to Hector Cruz Lopez, Dr. Soheil Nazarian, and Dr. Cesar Tirado. Acknowledgment is also extended to the INDOT personnel for their assistance and support in conducting test operations at the APT facility, particularly to Brent Richter, Dwayne Harris, Mike Moredock, Ross Butcher, and Kirk Germond.

TECHNICAL REPORT DOCUMENTATION PAGE

1. Report No. FHWA/IN/JTRP-2024/11	**2. Government Accession No.**	**3. Recipient's Catalog No.**
4. Title and Subtitle Full-Scale Dynamic Wireless Power Transfer and Pilot Project Implementation		**5. Report Date** March 2024 **6. Performing Organization Code**
7. Author(s) Oscar Andrés Moncada, Zainab Imran, Connor Vickers, Konstantina Gkritza, Steven Pekarek, Dionysios Aliprantis, Aaron Brovont, Behnam Jahangiri, and John E. Haddock		**8. Performing Organization Report No.** FHWA/IN/JTRP-2024/11
9. Performing Organization Name and Address Joint Transportation Research Program Hall for Discovery and Learning Research (DLR), Suite 204 207 S. Martin Jischke Drive West Lafayette, IN 47907		**10. Work Unit No.** **11. Contract or Grant No.** SPR-4607
12. Sponsoring Agency Name and Address Indiana Department of Transportation (SPR) State Office Building 100 North Senate Avenue Indianapolis, IN 46204		**13. Type of Report and Period Covered** Final Report **14. Sponsoring Agency Code**

15. Supplementary Notes

Conducted in cooperation with the U.S. Department of Transportation, Federal Highway Administration.

16. Abstract

Considering the challenges hindering the widespread adoption of electric vehicles (EVs) and heavy-duty electric vehicles (HDEVs), the integration of dynamic wireless power transfer (DWPT) technology into roadways has gained interest. By embedding DWPT components into pavement, electrical power can be delivered to an EV or HDEV as they are in motion. Yet, large-scale implementation depends on further in-depth research, both to explore optimal construction methods and to understand the impact of embedment on the pavement's resultant behavior. The objective of this project was trifold: (1) design and evaluate a transmitter-receiver topology for DWPT, (2) enhance the understanding of the interaction between the pavement and the embedded DWPT system, and (3) support the design and installation of a 230 kW DWPT system pilot for HDEVs on an existing INDOT roadway. A three-phase transmitter-receiver topology for DWPT was developed and validated, enabling the transmission of power across a wide range of vehicle classes while reducing the power oscillation that has been encountered in existing single-phase designs. To empirically evaluate the impact of DWPT on pavement, two pavement sections—one flexible and one rigid, were designed and constructed at an Accelerated Pavement Test (APT) facility. Following validation of the DWPT design through structural, thermal, and electromagnetic testing, Purdue University developed plans to establish a Dynamic Wireless Power Transfer Testbed (DWPTT) along ¼-mile of US-231 near West Lafayette. This testbed will serve as a critical platform for the transition of DWPT technology from APT sections to a practical roadway environment.

17. Key Words dynamic wireless power transfer, three-phase DWPT, pavement structure, pavement performance, electric vehicles	**18. Distribution Statement** No restrictions. This document is available through the National Technical Information Service, Springfield, VA 22161.

19. Security Classif. (of this report) Unclassified	**20. Security Classif. (of this page)** Unclassified	**21. No. of Pages** 63	**22. Price**

Form DOT F 1700.7 (8-72) Reproduction of completed page authorized

EXECUTIVE SUMMARY

Introduction

Electric vehicles (EVs), including heavy-duty electric vehicles (HDEVs), have gained attention as promising alternatives to internal combustion engine (ICE) vehicles due to their potential reduction of greenhouse gas emissions and pollution. However, the widespread adoption of EVs has been limited by underdeveloped charging infrastructure and the relatively high cost of batteries required to meet the desired travel range. For heavy-duty trucks, weight is a critical challenge as the mass of the batteries could reduce useful payload capacities to a point where an HDEV is not economically feasible. Hence, the broad integration of EVs into the transportation systems requires a multi-faceted approach that addresses these technical, infrastructural, and financial challenges.

To improve EV adoption, there has been a surge of interest in the use of dynamic wireless power transfer (DWPT) technology. By embedding DWPT components into pavement, electrical power can be delivered to an in-motion EV. This allows a vehicle to maintain its battery state of charge (and potentially increase its charge) as it is driven, translating to a significant reduction in the battery required, enhanced range, and reduced EV costs. Indeed, large-scale implementation of DWPT technology into the national roadway infrastructure could alleviate the major shortcomings that have limited their widespread adoption.

The National Science Foundation funded the Generation 4 Engineering Research Center (Gen4ERC) ASPIRE (Advancing Sustainability through Powered Infrastructure for Roadway Electrification) in 2020, with the objective of developing a "holistic approach to eliminate range and charging as barriers to electric vehicle use." ASPIRE brings together five universities, including Purdue University, to study the diverse challenges of EV charging strategies, adoption, and the coupling of electric and transportation infrastructures. With support from the Indiana Department of Transportation (INDOT) and ASPIRE, Purdue University has taken steps towards implementing and investigating the embedment of DWPT into Indiana roadways. This has included designing the electrical components required to transfer power from a roadway to a vehicle, as well as exploring the thermal and structural impacts of placing the components into a pavement. A description of the designs and impacts is provided in this report.

The following are the project objectives.

- Design and evaluate a transmitter-receiver topology for DWPT.
- Develop an understanding of pavement/DWPT system interaction, including a pavement material response to the DWPT integration.
- Develop a 230-kW DWPT pilot system and support its installation on an existing INDOT roadway.

Findings

The following are the key findings (and methods) of this study.

- Two pavement sections, one flexible and one rigid, with embedded DWPT components, were designed and constructed at the Accelerated Pavement Test (APT) facility in West Lafayette, Indiana. Each test section featured a DWPT unit, an assembly consisting of a concrete slab upon which the transmitter (tx) coil is placed. The construction of the flexible pavement involved milling 2 in. of an existing pavement surface, while the rigid pavement construction required a complete demolition of an existing pavement and reconstruction of a new slab. The DWPT unit in the flexible pavement is composed of Class C concrete and the DWPT unit in the rigid pavement features a commercially available magnetizable concrete, which is composed of ferrite particles embedded within a cement matrix.
- A three-phase transmitter-receiver topology for DWPT was developed and validated. In contrast to existing commercial technologies, the three-phase topology the team developed has magnetic poles that travel transverse to the direction of vehicle movement. A benefit of this approach is that power delivered to vehicles scales directly with receiver length. This enables the construction of a roadway that can provide power across a wide range of vehicle classes. It also reduces the power oscillation that has been encountered in existing single-phase designs. To support studies on the electromagnetic, thermal, and structural performance of the topology, two DWPT systems rated for a peak power of 200 kW were designed. In one design, magnetized concrete was used to form the transmitter core. In the second design, standard (magnetically inert) concrete was used for the transmitter core. Performance estimates indicated that the magnetic-based design exhibited a smaller compensation circuit mass and volume as well as a slight increase in system efficiency. In testing and analyzing misalignment, it was also observed that both designs have similar behavior within $\pm 20\%$ alignment. However, the magnetic-core design demonstrated more pronounced power reduction and sensitivity to misalignment outside this range.
- The position and alignment of the dual-axle wheel on the pavement influenced load distribution. When the center of the dual-axle configuration was placed directly above the edge of the DWPT unit, the load was concentrated at the interface between the asphalt and the concrete, which induced greater deformation and thus higher strain. On the other hand, when the middle of the dual-axle configuration was placed over the edge of the DWPT unit, the tire load spread over a wider area above the DWPT unit. This distribution, coupled with the concrete stiffness, reduced the localized stress and consequently deformation, leading to lower strain values within the asphalt.
- Atypical deflection patterns in the flexible section, as observed from FWD testing, highlight the influence of the embedded DWPT components. This unexpected trend could be attributed to factors such as potential secondary compaction from traffic and the possible stiffening of the asphalt due to waste heat generated by the DWPT mechanism. The FWD results over the rigid section highlight a pronounced increase in deflection values after traffic, which is indicative of reduced structural integrity and associated with the presence of a mid-panel crack.
- The thermal testing at the APT facility shows a rise in pavement temperature upon energization; yet this increased stabilizes over time across all thermocouple depths. This observation suggests that the pavement and coils effectively dissipate heat into the surrounding environment, ensuring sustained operation. The maximum temperature rise during energization was about 7°F for the rigid section and 12°F for the flexible section.
- Among the two pavement sections, only the rigid pavement exhibited visible distress, identified as a mid-panel crack.

Several factors contributed to the crack formation, including inadequate adhesion between concrete interfaces, material variations, construction issues, and nonuniform load distribution. The manual construction procedures, which were employed to prevent disrupting the embedded DWPT components and sensor instrumentation, and the 1-week gap between casting the magnetizable DWPT unit and the surrounding slab might have further influenced the adhesion strength of the rigid pavement section.

- No pronounced distress was present in the flexible pavement section after 25,000 passes. The pavement showed a minimal amount of rutting, with an approximate decrease of 0.3% in vertical distance as measured by the laser scanner before and after traffic.

Implementation

This project enabled the construction of two pavement sections, which essentially served as a proof-of-concept within a controlled testing environment. Embedding DWPT components introduced unique challenges in the conventional construction processes due to the altered geometric composition of the pavement. While specialized manual techniques were employed for this small-scale project, such methods may prove unfeasible for large-scale implementation. Since the construction of the pavement sections highly influences the resulting long-time serviceability of the pavement, further research into appropriate and optimized construction methods should be done.

Purdue University, in collaboration with INDOT and a consulting firm, created the design and specifications for a Dynamic Wireless Power Transfer Testbed (DWPTT) along a ¼-mile roadway located at US 231, between Lindberg Road and Cumberland Avenue, immediately in front of the INDOT subdistrict office in West Lafayette, IN. This testbed will serve as a platform for the transition of DWPT technology from short pavement sections to a practical roadway environment. The pilot aims to further develop and refine installation methods, test the system in a practical roadway environment, and create ways to reduce costs and gain acceptance by EV manufacturers and the community. It also seeks to provide a testing platform to evaluate the reliability, aging, and performance of the pavement. Indeed, one goal will be to share insights with industry members to support the expansion of DWPT into interstate highways.

CONTENTS

LIST OF TABLES

LIST OF FIGURES

1. INTRODUCTION

The transportation sector contributes to approximately 28% of total U.S greenhouse gas emissions, which are largely derived from the combustion of petroleum-based products in internal combustion engine (ICE) vehicles (U.S. EPA, 2024). As the road transportation sector aims to reduce its level of emissions, the long-term objective is to transition from fossil fuel dependency to alternative renewable energy sources. In this context, electric vehicles (EVs), including heavy-duty electric vehicles (HDEVs), have garnered attention as a viable solution to reduce the high emissions generated by the transportation sector, since EVs produce no direct exhaust emissions (U.S. Department of Energy, 2021). However, the widespread adoption of EVs has been hindered by challenges such as underdeveloped charging infrastructure, high capital costs, and driving range limitations (range anxiety) (IEA, 2022), along with broader concerns such as the heightened electricity demand on power generation infrastructures and ecological impacts from increased material demands for battery production (Paoli & Gül, 2022). Weight is an additional challenge, especially for HDEVs, as the battery weight can potentially decrease useful payload capacities to the point of being economically unviable.

In response to these challenges, the integration of Dynamic Wireless Power Transfer (DWPT) technology into roadways has gained significant research interest. Embedding DWPT components into pavement structures could allow EVs to maintain power levels and accrue charge while traveling, which may potentially enhance range and overall efficiency. This innovative approach could mitigate major adoption barriers by enhancing charging infrastructure directly within the roadway and extending driving range. It might also influence EV design by enabling smaller on-board batteries and reduced vehicle weight, thus enhancing economic and operational performance.

Due to its complex and multifaceted nature, the development of DWPT technology has fostered collaborative research across different disciplines, including electrical and civil engineering. Hardware demonstrations and feasibility studies around the world have shown great interest in the DWPT technology. Utah State University constructed an electrified test track and demonstrated that in-motion EVs can be effectively and safely charged through dynamic wireless charging. The Oak Ridge National Laboratory has also focused on quasi- and dynamic-wireless charging solutions (Brecher & Arthur, 2014; Miller et al., 2015). Outside the U.S., pilot programs on DWPT are underway in France, Italy, Sweden, and Israel (ICCS, 2014; Unplugged, 2015). These pilots mostly focus on low-speed, low-power applications. The research by Konstantinou et al. (2021) demonstrated the technical and financial feasibility of providing DWPT for Class 8 and 9 trucks in the state of Indiana. It was found that the required high power (around 230 kW) for large trucks can be effectively transferred across an approximate 10-in. airgap between the roadway and the vehicle. Moreover, the investment in high-power DWPT implementation is projected to be recoverable within a 30-year period, contingent upon a medium to high adoption of the technology (Haddad et al., 2022). The most suitable locations for implementing DWPT lanes were found on interstates that are characterized by high truck traffic (Konstantinou et al., 2021).

Effective implementation of DWPT technology into actual road infrastructures requires further in-depth investigation into the construction methods needed to embed the components, the resulting mechanical behavior of the pavement structure, and the efficiency of high-power transfer capabilities when embedded within an actual roadway. The pavement structure must be capable of properly protecting the embedded DWPT components, while ensuring that the construction methods employed do not compromise the integrity or efficiency of the embedded system and the structure surrounding it (Chen, 2016). Hence, it is imperative to conduct a holistic assessment that encompasses the construction methods needed to ensure that the DWPT components are embedded safely without compromising the integrity of the pavement structure.

1.1 Project Tasks

The aim of this project was to integrate DWPT components into two small-scale pavements and evaluate their mechanical and thermal behavior under accelerated pavement testing loads. In view of the above, a simultaneous multi-phase approach was coordinated to address the project objectives. The three project phases, along with corresponding tasks, are as follows.

1.1.1 Phase 1: Laboratory Testing of Pavement Materials/DWPT Systems

A DWPT testbed was established within the Vehicle Systems Laboratory of Wang Hall at Purdue University. The utility connection to the building transformer servicing the laboratory was upgraded to provide up to 300 kVA at 0.8 pf. A 215-kW commercial (Regatron) power supply was purchased and installed to provide DC power to the testbed. A commercial Wolfspeed inverter was acquired and programmed to provide the high-frequency AC (40 kHz fundamental power) to the transmitter system. The programming of the inverter, along with the development of compensation circuits, transmitter/receiver, and passive rectifier all took place in Phase 1.

- *Task 1.1 Design of the DWPT Electrical System*

The first task involved establishing the design of a DWPT system for laboratory instantiation. Under a previous INDOT effort, design software for a single-phase double-D transmitter/receiver-based system was developed. At the beginning of this effort, alternative topologizes were evaluated, including three-phase transmitter/receivers, which offer the advantage of

smaller conductors and power electronic switches. However, the number of components and connections is greater. Subsequent efforts concentrated on the development of design models for the three-phase topologies to enable evaluation of their performance. The aforementioned advantages of the three-phase design, as well as the reduction in power oscillation observed during the design process, led to the decision to abandon single-phase topologies. The focus of the exploration was then moved to consider the tradeoffs of utilizing magnetizable concrete within the transmitter core versus no magnetic material within the transmitter (coreless). It was found that utilizing the magnetizable concrete allowed a reduction in the amount of copper used in the transmitter conductors. However, the cost of the magnetizable concrete and its performance within a roadway were unknown. Since compensation circuits at the 200-kW power level are relatively costly, the team decided to procure the compensation circuit capacitors and inductors for the magnetized-based design. In parallel, the team decided to advance both the magnetized and coreless topologies for thermal and structural testing within the accelerated pavement test (APT) facility. In addition, the team decided to leverage the compensation circuit components designed for the magnetized system to construct a reduced-power-level (50 kW) coreless design.

- *Task 1.2 Instantiate the DWPT Electrical System*

The second task encompassed the construction of the specified DWPT systems from Task 1. This task included creating the structural framework for both transmitters and receivers, constructing the capacitor networks used in the compensation circuits, programming the inverter controls, and implementing physical connections among all system components for high-power, high-voltage experimentation. Additionally, a data acquisition system was established to monitor time-domain waveforms of voltage, current, power, and magnetic fields.

- *Task 1.3 Experimental Testing of the DWPT Electrical System*

Once the DWPT was instantiated, experiments were conducted to validate the system's performance. Initial testing was conducted under optimal alignment conditions, controlling the inverter/power sink to maintain a roughly 50 kW power transfer. The relatively low power level chosen for testing was due in large part to the worldwide parts shortage that was occurring during/after the 2020 Covid outbreak. Specifically, when the inverter was procured, it was one of the only units in stock at reputable suppliers and had an estimated 18-month lead-time for replacement. This task was crucial for confirming the design models and the expected power transferred from transmitter/receiver, the time-domain waveforms within the transmitter and receiver circuits, and converter efficiencies. All matched well with the predictions of design models.

1.1.2 Phase 2: Accelerated Pavement Testing

In Phase 2, the installation and testing of transmitter coils were carried out within the APT facility. The objective was to confirm the pavement's capacity to endure the structural and thermal loads introduced by the DWPT system. The APT facility was specifically constructed to enable full-scale pavement evaluations under controlled conditions. Within the facility, a pit measuring 20 ft. in length, 20 ft. in width, and 6 ft. in height served as the construction site for pavement test sections, which can accommodate various pavement layers such as subgrade, subbase, base, and either Portland cement concrete (PCC) or asphalt. To mimic the effects of recurring truck traffic, the test pavements were subjected to a load of 9,000 lbs (one half a standard truck axle), applied through two pneumatic truck tires, equivalent to half the load of a standard truck axle.

Within each pavement test section of the APT facility, transmitter coils were installed and assessed for their ability to withstand the structural and thermal stresses induced by the DWPT system. These evaluations focused solely on the interaction between the transmitter and pavement, omitting the installation of a receiver to streamline costs. Each transmitter was embedded within the pavement structure and was equipped with sensor instrumentation to record data on the mechanical and thermal behavior of the structure. Commercial power supplies were used to energize the system, replicating the thermal operational conditions anticipated in actual deployment.

- *Task 2.1 Pavement Test Sections Construction*

This task encompassed leveraging the APT facility to assess roadway performance under expected mechanical and thermal loads. The construction phase encompassed the design of both pavement test sections, the selection of the corresponding materials, coordination with relevant entities (INDOT, contractor, operators, and construction personnel), and application of the construction procedures required for each test section, respectively. The APT facility housed two flexible sections from a previous research project, so preparation work was performed before the test section construction for this project began. Two inches were milled from the surface of one of the existing flexible pavement sections. The second existing flexible pavement section was completely removed, down to the A-6 subgrade, to make way for the new rigid pavement section.

- *Task 2.2 Testing and Data Acquisition*

This task focused on examining the interaction between the pavement and the embedded DWPT system and the pavement's response to traffic loads. The procedure involved conducting several testing operations, including accelerated pavement testing traffic, to subject the pavement to varying load applications while the DWPT transmitters remained turned on. Based upon Finite Element Models (FEM)

predictions, a product of collaboration between Purdue University and the University of Texas El Paso (UTEP), sensor instrumentation was strategically placed within the pavement.

- *Task 2.3 Data Analysis*

This task focused on monitoring, processing, and analyzing the mechanical and thermal response of both pavement test sections, such as vertical stress, longitudinal and transverse strains, and the thermal distribution. The analysis of the gathered data provided insight into the influence the DWPT integration has on the structural integrity and material properties of the pavement.

1.1.3 Phase 3: Pilot Testbed Implementation

The third phase encompassed the design and development of specifications for a pilot testbed of a pavement with embedded DWPT into an existing INDOT highway infrastructure. INDOT, in collaboration with Purdue University, is developing plans to establish a Dynamic Wireless Power Transfer Testbed (DWPTT) along a roughly ¼-mile of roadway in West Lafayette, IN. The pilot DWPT road section has two key objectives: (1) develop and optimize efficient installation methods for the transmitter coils within a practical roadway context; and (2) provide a comprehensive testing and validation platform for the transmitters and associated electronics under realistic conditions, thus allowing for the evaluation of reliability, aging, and performance of the materials and system.

- *Task 3.1 Pilot Project Design*

The DWPT designs developed by the Purdue research team were shared with INDOT/AECOM with the expectation that these designs would be the starting point upon which pilot testbed was based.

- *Task 3.2 Pilot Project Construction*

Purdue, in tandem with INDOT/AECOM developed the technical specifications used in the bid documents for the construction of the pilot system. In addition, Purdue has developed and instantiated transmitter coil construction techniques that were presented to potential contractors.

2. LITERATURE REVIEW

Considering that the transportation sector contributed to over a quarter (28%) of the world's total greenhouse gas emissions in 2021 (U.S. EPA, 2024), its substantial impact on climate change emphasizes the critical need for developing and adopting strategies that significantly reduce greenhouse gas emissions in all areas of transportation. The sector's impact is multifaceted, as it significantly contributes to global emissions, compromises local air quality, and poses potential health risks to the population. Vehicles alone contribute to roughly 10% of global greenhouse gas emissions (IEA, 2021). In this context, short-term measures intended to reduce emissions from vehicles focus on enhancing fuel efficiency and emissions control. Meanwhile, long-term goals aim for a progressive transition from fossil-based to renewable energy sources (IEA, 2020).

Aligning with these objectives, EVs have gained interest as a potential mean to address the emissions impact from the transportation sector, attributed to their zero-tailpipe emissions footprint, a product of their non-reliance on fossil fuel combustion in contrast to ICE vehicles (U.S. Department of Energy, 2021). The EV market continues to experience exponential growth, with the share of EVs in total vehicle sales rising from approximately 4% in 2020 to 14% in 2022, with indications of further growth in the following years (IEA, 2023). Despite a notable rise in electric vehicle sales, they still constitute only a small portion of the overall vehicle market, with widespread adoption hindered by high upfront costs affecting lower-income households and their limited driving range, problematic for those in remote areas or with long-distance travel needs (Yozwiak, 2022). Moreover, the existing network of charging stations may not be sufficient to support a significant escalation in EV adoption (IEA, 2021). Environmental obstacles in the production and disposal of EV batteries, which involve fossil fuel use for energy-intensive manufacturing and processing, alongside the employment of environmentally detrimental materials, further complicate the adoption of electric vehicles (Co et al., 2018). Nonetheless, the environmental and public health benefits of EVs, such as reduced greenhouse emissions, continue to drive technological advancements and affordability improvements (Peters et al., 2020).

Recent years have seen a surge in research efforts and widespread interest in advancing DWPT technology for roadway integration. Noteworthy investigations have been conducted to explore the power transfer capabilities of DWPT technology, evaluate its associated challenges, and achieve advancements in this domain (Bi et al., 2016; Brovont et al., 2023; Chen, 2016; El-Shahat et al., 2019; Majhi et al., 2020). Nevertheless, additional research is essential to gain a deeper understanding of how the embedded DWPT system affects pavement behavior when subjected to different traffic and environmental conditions. Moreover, it is crucial to ensure that the optimal embedment of the components does not compromise the integrity of either the DWPT system or the pavement.

2.1 Wireless Power Transfer

Wireless Power Transfer (WPT) systems allow the transmission of electric power from one point to another through the vacuum of space or the Earth's atmosphere without the use of wires (Brown, 1996). A WPT system involves a transmitter unit that is connected to a main source of power that transforms the electrical power into an electromagnetic field.

In a broader sense, WPT can be classified as far-field (radiative) transmission and near-field (non-radiative) transmission (Popovic, 2017). Near-field WPT systems are able to transfer high power through an electric or magnetic coupling mechanism, while far-field WPT systems typically enable low-power electromagnetic waves over long distances for communication.

Among the various wireless power transfer (WPT) technologies, inductive power transfer (IPT) and capacitive power transfer (CPT) stand out for their ability to transmit power up to megawatt levels over short distances. These systems may achieve high efficiency via inductive or capacitive links, even when handling high-power transfers (Van Mulders et al., 2022). However, their main limitation is the short charging distance capabilities. IPT technology, similar to Nikola Tesla's coil (1904), uses electromagnetic fields for wireless power transmission, employing resonant circuits for high-frequency oscillations.

IPT has been shown to be a practical method for charging EVs because it is safe, convenient, and reliable (Budhia et al., 2011). IPT offers the advantage of a galvanically isolated power transfer to the vehicle without the need for moving mechanical parts that are subject to corrosion, wear, and fatigue; thus, removes safety concerns related to the handling of electrical equipment (Bosshard & Kolar, 2016). In this context, a typical IPT system designed to charge electric vehicle usually consists of an on-board pick-up device installed beneath the vehicle's chassis and an off-board power delivery device embedded in the roadway (Chen, 2016). The off-board IPT system includes a power supply that provides a regulated direct current via a rectifier, a DC-AC converter that delivers high output frequencies in combination with a capacitance to achieve resonance with the transmitter and reduce switching loss; and a transmitter that is mutually coupled with the pick-up-device. The transmitter is composed mainly of conductive coils, ferrite cores, and a backing plate. In an IPT mechanism, voltage induction in the coil occurs based on Ampere's and Faraday's Laws (Covic & Boys, 2013). Ampere's Law states that the magnetic field created by an electric current is proportional to the size of that electric current with a constant of proportionality equal to the permeability of free space. Faraday's Law states that the amount of induced voltage is equal to the rate of change of the magnetic flux.

The performance efficiency of a typical IPT system is affected by various parameters, such as frequency, the distance and lateral misalignments between coils, the applied load, and the magnetic field's geometry (Villa et al., 2009). Power transfer range and misalignment tolerance are critical design criteria that must be addressed to attain higher relative energy transfer (Alphones et al., 2014). The employment of larger coils can improve efficiency across a broader range; however, the system must maintain an acceptable level of efficiency even at higher relative transfer distances. (Alphones et al., 2014) noted some optimization methods to improve the quality factor of the coils such as using Litz wires to decrease skin losses at lower frequencies, while hollow copper tubes can be used to reduce skin losses at higher frequencies.

2.2 Three-Phase DWPT System

Brovont et al. (2023) presented a magnetic design for three-phase DWPT systems. This approach is based on a topology that eliminates the power oscillation and voltage/current sharing problems that plague planar three-phase DWPT systems. It uses a three-phase transmitter coil and a three-phase receiver coil. The coils are arranged in a planar configuration, and they are coupled by a magnetic field. The transmitter coil is driven by a three-phase sinusoidal signal, and the receiver coil is connected to a load. The approach's functionality was analyzed using a combination of a boundary element model-based magnetic field simulator and an electric circuit simulator that included the components of the DC-AC converter, compensation circuits, transmitter/receiver, vehicle AC-DC converter and load. The results of the simulation showed that the proposed design can achieve a high-power transfer efficiency (PTE) of up to 90%. Moreover, it showed reasonable resilience to both misalignment and load variation (change in the load connected to the receiver coil), which means that it can maintain a high-power transfer efficiency even when the receiver coil is misaligned, or the load is varied. Ultimately, this strategy appears to be a promising new approach to three-phase DWPT systems, proving efficient, relatively insensitive to load variation, and implementable using planar coils.

2.3 Pavement with Embedded DWPT

Progress has been made in the power optimization of DWPT technology, yet further in-depth study is required to investigate the construction methods necessary for optimal embedment and to understand the impact the embedded components have on the pavement's mechanical and thermal behavior. The pavement structure should be able to protect the embedded components (Covic & Boys, 2013), while ensuring that the construction methods employed do not compromise the integrity of both the embedded system and the pavement (Chen et al., 2016). Various construction methods for incorporating WPT charging components into pavement structures have been explored (ICCS, 2014; Olson, 2013; Systems Control Technology, Inc., 1994) either through prefabrication-based approaches, where components are produced off-site and then embedded on-site, or direct in-situ procedures, involving installation directly at the site. A series of technical advancements, as highlighted in (Chen et al., 2019), are necessary to foster the sustainable implementation of pavements with embedded DWPT. These include (1) technologies that offer viable charging solutions, (2) the successful incorporation of these technologies into practical

infrastructure, and (3) ensuring efficient functionality and cost-effective maintenance over the infrastructure's lifespan. Concurrently, Ledesma (2015) identifies key aspects for consideration in designing and constructing roads with embedded DWPT—pavement geometry and location, the properties of the protective overlay, and power transfer efficiency considerations. In the case of a WPT system embedded into a roadway, the dielectric properties of the pavement material can also impact the efficiency of power transfer and contribute to potential power losses and waste heat propagation throughout the structure, particularly assuming that the pavement material is non-magnetic. The findings of (Chen, 2016) indicate that the amount of power lost within a roadway with an embedded IPT system is relatively insignificant compared to the amount of power typically transferred in an IPT system. Moreover, (Chen, 2016) suggests that integrating an IPT system into a roadway is unlikely to significantly reduce the overall power transfer efficiency of the system.

The study referenced in (Chen et al., 2016) indicates that incorporating smart features into existing road infrastructure could yield significant advancements in road materials and structures, currently hindered by cost-benefit limitations. However, achieving this requires addressing several challenges, including optimizing road structures to accommodate these systems, developing higher-quality road materials for improved durability, revising traditional construction and maintenance methods, balancing the economic and environmental costs of new functions, and determining financial responsibility for technology failures within roads. A study in (Chen et al., 2019) indicated that while embedding WPT in current road infrastructure does increase CO2 impacts during the system's life cycle, a major portion of these impacts arises from road maintenance and rehabilitation. Given that the frequency of such rehabilitations is largely influenced by the road's structural performance, a high-performing infrastructure is vital for the sustainable, cost-effective implementation of pavements with embedded DWPT.

3. PURDUE DWPT TEST BED CONFIGURATION

3.1 Design of DWPT Electrical System (Three-Phase DWPT)

The team devised a transmitter-receiver topology for dynamic wireless power transfer, as depicted in Figure 3.1, featuring three distinct phases. This configuration outputs a peak power of 200 kW, catering to the requirements of standard Class-8 semi-tractor trailer trucks. The transmitter's design incorporates wye-connected Litz wire conductor cables for the transmitter coil, along with a transformer rectifier, inverter, and an LCC compensation circuit. Detailed design parameters and ratings can be found in Table 3.1. Similarly, the receiver coil follows a comparable design, utilizing a wye-connected Litz wire conductor cable coil with series compensation. The strategic choice of compensation circuits results in load-independent currents in the transmitter windings and voltage source behavior at the receiver coil's output. These features contribute to the design's appealing interoperability and control characteristics. To examine the inherent low power oscillation of the three-phase DWPT system without filtering or active suppression, a resistive load is assumed at the output of the receiver unit.

Addressing an essential hurdle in crafting a three-phase DWPT system involves tackling the imbalance within the mutual terms of the transmitter-receiver inductance matrix. This disparity results in suboptimal sharing of current/voltage among phases and triggers pronounced power oscillation at both the input and output.

To mitigate this challenge, a symmetrical-components (SC) analysis was conducted on the three-phase transmitter-receiver topology, revealing the positive- or negative-sequence T-equivalent circuit depicted in Figure 3.2, where $(x, y) \in \{(1, 2), (2, 1)\}$. The superscripts 1 or 2 denote positive or negative sequences, respectively. The voltage sources in the circuit symbolize the positive- and negative-sequence coupling

TABLE 3.1
Specified Design Parameters, Ratings, and Constraints (Brovont et al., 2022)

Parameter	Description	Value	Units
P_r	Rated average input power	210	kW
V_{in}	dc input voltage	750	V
V_{out}	Rated output voltage	750	V
f_0	Fundamental excitation frequency	85	kHz
d_{tr}	Winding-to-winding distance	26.5	cm
w_{tx}	tx width	85	cm
l_{tx}	tx length	3.65	m
w_{rx}	rx width	66	cm
w_{rc}	rx core width	66	cm
N_{rx}	Number of rx turns	3	turns
t_{rc}	rx core thickness	1	cm
OD_{wire}	Outer diameter of litz wire	1.07	cm

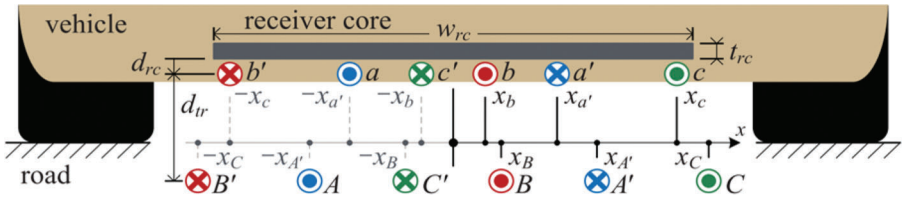

Figure 3.1 Archetypal cross-section of proposed three-phase transmitter-receiver topology (Brovont et al., 2023).

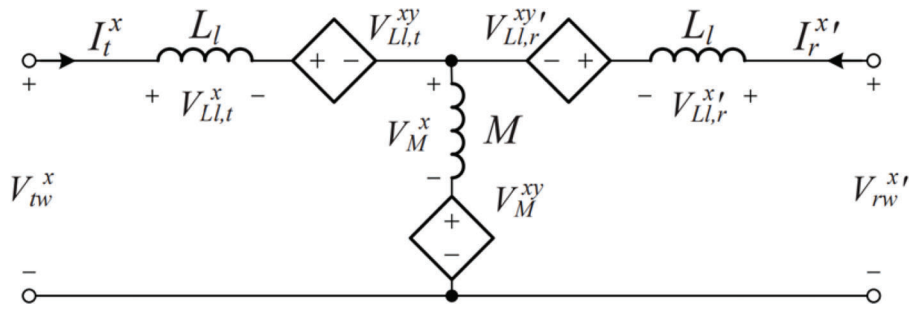

Figure 3.2 SC sequence T-equivalent model of a generic three-phase tx/rx system (Brovont et al., 2023).

terms responsible for the phase imbalance and power oscillation issues. These sequence coupling terms can be eliminated through a meticulous design of the coil layout. Once this is done, the three-phase system can be formulated using the positive-sequence circuit as an equivalent single-phase system. A boundary element method was employed for inductance calculations on a per-length basis. An assumption that both the transmitter and receiver exhibit significant length compared to their widths is made, ensuring a reasonably accurate 2-D approximation. The coils are assumed to be made from 2-AWG Litz wire and the specified receiver core is MN60 ferrite. Exploring alternative transmitter designs, two options were considered: (1) a magnetizable-core design and (2) a coreless configuration. In the coreless configuration, support for the transmitter coil comes from a structurally inert material that is both magnetically and electrically inactive.

The magnetized-based core transmitter was designed with a single turn, while the coreless transmitter incorporates two turns. This achieved comparable per-length mutual inductance for both configurations. Table 3.2 details the per-unit length values of sequence self- and mutual-inductance for both the magnetized-based and coreless designs. These values are used for sizing the receiver and determining compensation circuit component values.

To obtain the total receiver self- and mutual-inductance values, the per-length values are scaled by the receiver length, ℓrx. Calculating the total transmitter self-inductance involves summing the per-length inductances with and without the receiver, scaled by ℓrx and ℓtx $-$ ℓrx, respectively. The configuration of the transmitter-receiver topology allows the receiver length to serve as a tuning parameter for achieving the desired operating point.

Table 3.3 provides a concise overview of critical performance metrics, design parameters, and ratings for both magnetized-based and coreless DWPT systems. The magnetized-based system presents notable advantages, including a reduction in compensation circuit volume and mass, a transmitter winding with a single turn, and a moderate improvement in efficiency. The magnetizable core enhances mutual coupling without significantly increasing transmitter self-inductance. As a result, the magnetized-based transmitter winding demands less reactive power at the specified operating point and allows for a smaller transmitter-side series capacitor when compared to the coreless design. This efficiency enhancement stems from lower conduction loss in the transmitter winding and the transmitter-side series capacitor bank.

TABLE 3.2
TX and RX Per-Length Sequence Self and Mutual Inductances (Brovont et al., 2022)

Inductance [μh/m]	Design		Note
	Magnetizable	Coreless	
L_T	3.46 3.29	7.62 7.47	with rx above without rx above
L_R	25.77	23.87	
L_{TR}	2.33	2.21	

3.2 Instantiate DWPT Electrical System

The proposed transmitter-receiver topology was implemented in a laboratory prototype, depicted in Figure 3.3. The transmitter-receiver unit, configured with two turns each, was dimensioned lengthwise to achieve a sequence mutual inductance (M) of 2.37 μH, closely aligning with the characterized value of 2.41 μH. Measured sequence self-inductances for the transmitter and receiver were 23.4 μH and 14.6 μH, respectively. Imperfect alignment and imbalance in end turns and leads contributed to a characterized sequence coupling factor (σ) of 6.7%.

Compensation circuits, employing LCC for the transmitter and series compensation for the receiver, were tailored for 40-kHz operation. A SiC-based three-phase inverter with 180°-switching converted a regulated dc supply to positive-sequence excitation. At the receiver output, a SiC-based three-phase passive rectifier supplied a resistive load bank. In these proposed designs, electromagnetic fields move transversely to vehicle motion, promoting interoperability across vehicle classes as power transfer scales directly with receiver length. Time-domain simulations confirmed the anticipated operation of the DWPT systems during a charging event. Notably, both designs exhibited minimal power ripple at full alignment due to

TABLE 3.3
Comparison of Magnetized-Based and Coreless Designs: Predicted Performance, Parameters, and Ratings (Brovont et al., 2022)

Parameter	Description	Design		Units
		Magnetizable	Coreless	
N_{tx}	Number of tx winding turns	1	2	turns
l_{rx}	rx active length	1.31	1.38	m
k	Coupling factor (per-length)	24.6	16.4	%
B_{stray}	Stray field at lane edge	23.6	23.1	μT
n	Steady-state efficiency	95.9	95.1	%
m_{comp}	Total comp. circuit mass	154	185	kg
v_{comp}	Total comp. circuit volume	26	32	L
I_t^1	tx phase rms current	207	207	A
I_r^1	rx phase rms current	207	207	A
I_{inv}	Inverter phase rms current	207	207	A
V_{Cftx}	Shunt cap. pk. voltage	675	675	V
V_{CT}	tx series cap. pk. voltage	1.44	3.81	kV
V_{CR}	rx series cap. pk. voltage	5.29	5.15	kV
x_B	tx B coil-side position	4.5	4.3	cm
x'_A	tx coil-side position	18.7	13.1	cm
x_C	tx C coil-side position	42.0	41.4	cm
x_b	rx b coil-side position	3.7	3.8	cm
x'_a	rx a′ coil-side position	11.3	7.5	cm
x_c	rx c coil-side position	31.4	31.4	cm
t_{tc}	tx core thickness	19.1	–	cm
w_{tc}	tx core width	76.4	–	cm
d_{tc}	tx core separation	0.64	–	cm
d_{rc}	rx core thickness	0.8	1.0	cm

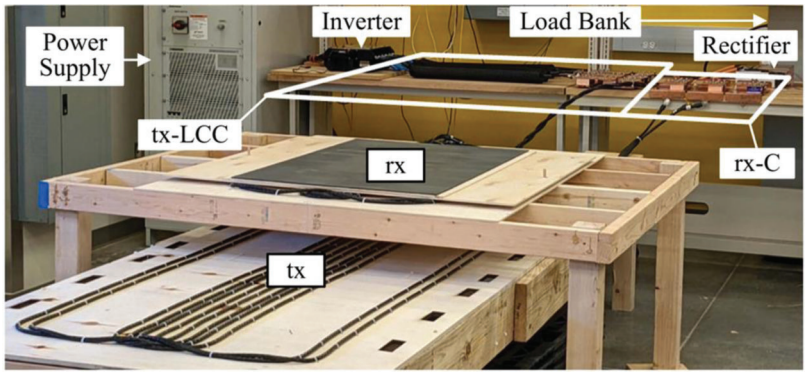

Figure 3.3 Laboratory prototype of proposed three-phase DWPT system (Brovont et al., 2023).

excellent phase balance in the transmitter, receiver, and inverter.

Performance estimates indicate that the magnetized-based design boasts a smaller compensation circuit mass and volume as well as a slight increase in system efficiency. In testing and analyzing misalignment, it was also observed that both designs have similar behavior within ±20% alignment. However, the magnetizable-core design demonstrated more pronounced power reduction and sensitivity to misalignment beyond this range.

4. ACCELERATED PAVEMENT TEST (APT) FACILITY

The APT facility, located in an environmentally controlled building spanning 186 m^2, consists of a test pit, a loading mechanism, and a collection of control and monitoring equipment. The facility features a pit measuring 20 ft. in length, 20 ft. in width, and 6 ft. in height, used for the construction of pavement test sections. The loading mechanism consists of a heavy vehicle prototype mounted on a large steel frame carriage, designed to mimic damage generated from traffic loads on the pavement structure, as shown in Figure 4.1.

The operator control room is equipped with two interconnected computers to manage the software and hardware necessary for controlling the accelerated pavement testing procedures. One of the computers controls the testing operation, while the other one handles data collection, processing, and reduction. The operator room houses a Keysight N8932A dc power supply unit that provides constant current to the DWPT coils, simulating the resistive losses anticipated in a 230 kW three-phase DWPT tx coil formed by a Type 2 4-AWG Litz wire.

The load carriage includes a set of wheels with full-scale tires, driven by a 30 hp motor and a 50 hp drive, enabling speeds of up to 5 mph. Four air pistons, as illustrated in Figure 4.2, exert a constant force of up to 20,000 lbs, are designed to be programmable for either static or dynamic loading modes. These pistons are designed to lift the dual-axle wheel and return them to the starting position of the test lanes when conducting one-directional testing. For this study, a dual tire setup was employed to apply a load of 9,000 lbs. The individual tire footprints had approximate dimensions of 8 in. by 7.5 in. (width and length), with 13.25 in. between the centerlines of the tires. The tires were inflated to 100 psi to simulate standard axle wheel load conditions. Additionally, as shown in Figure 4.3, the carriage is equipped with an automated laser scanner mounted behind the wheel assembly to enable the measurement of longitudinal and transverse pavement profiles over time.

4.1 Pavement Sections Design

For this project, two pavement test sections with embedded DWPT components were designed and constructed: a flexible and rigid pavement section respectively. Each pavement section is integrated with a concrete slab upon which the DWPT components are placed. The entire assembly is referred to as a DWPT unit, as illustrated in Figure 4.4. Both test sections measure 20 ft. in length, 10 ft. in width, and 10 in. in height, as illustrated in the diagram in Figure 4.5. Each DWPT unit, embedded 2 in. underneath the top surface, measures 10 ft. in length, 4 ft. in width, and 8 in. thick. The cross section of both pavement test sections is illustrated in Figure 4.6 and detailed on Table 4.1.

The flexible test section was constructed above a 14 in. subgrade course of lime-treated A-6 soil, over 48 in. of untreated A-6 subgrade soil. The asphalt mixture design consists of a 2-in. thick surface course of 9.5 mm asphalt mixture, a 2-in. thick intermediate course of 19.0-mm asphalt mixture, and a 6-in. thick base course of 19.0-mm asphalt mixture. On the other hand, the rigid test section features a 10-in. PCC surface slab, a 3-in. #8 aggregate subbase, and a 6-in. #53 aggregate base constructed above a 5-in. subgrade course of lime-treated A-6 soil 48 in. of untreated A-6 soil. A joint was built 4 ft. away from the upper edge. The DWPT unit within the flexible pavement is composed of Class C concrete and it is placed in the geometrical center of the section, 4 ft. away from the longitudinal edges and 3 ft. away from the transverse edges. The rigid pavement's DWPT unit is placed 2 ft. away from the upper concrete joint, 2 ft. from the lower edge, and 3 ft. away from both transverse edges. It features a material known as magnetizable concrete; a type of concrete composed of ferrite particles embedded in a cement matrix (Magment, 2016). Figure 4.7 shows a top view of both pavement sections prior to the asphalt or concrete placement.

Figure 4.1 Accelerated pavement testing mechanism (vehicle prototype on steel frame carriage).

Figure 4.2 Air pistons.

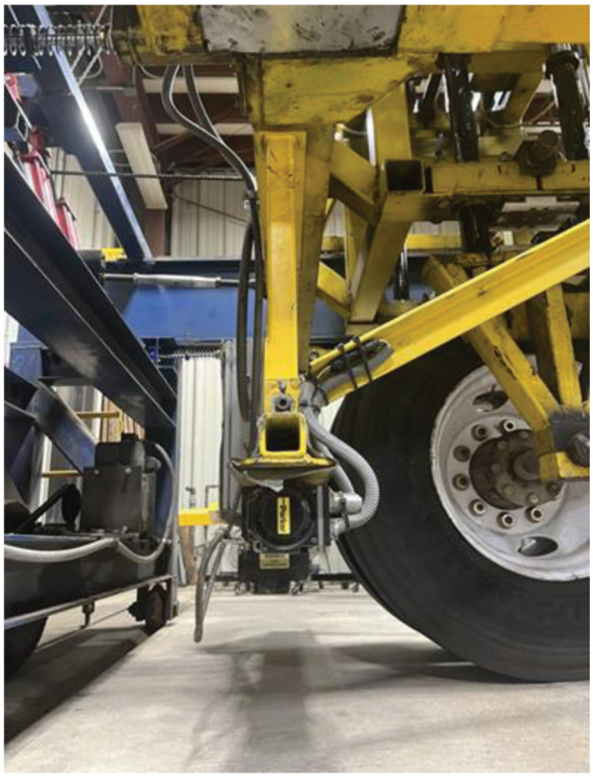

Figure 4.3 Automated laser scanner.

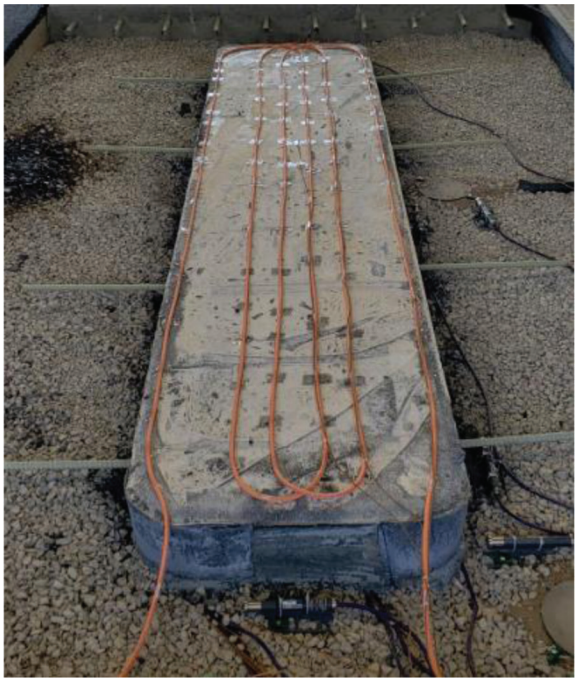

Figure 4.4 Magnetizable concrete DWPT unit in rigid pavement section.

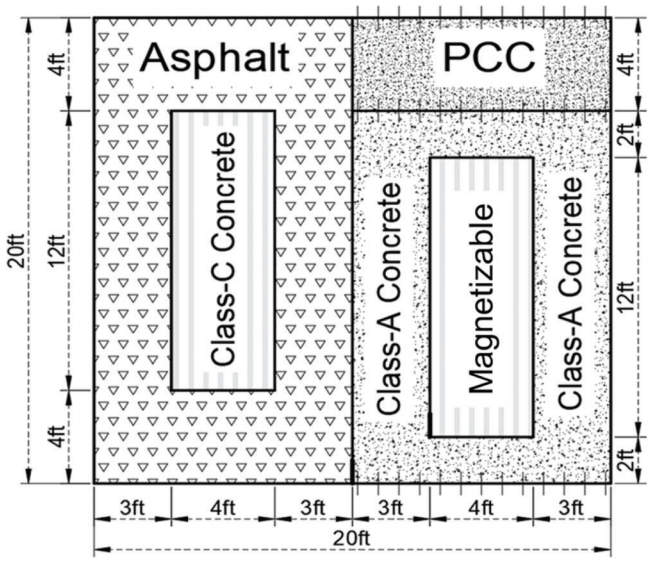

Figure 4.5 Pavement sections design.

4.2 UTEP Finite Element

The University of Texas at El Paso worked in collaboration with the Purdue research team to predict the mechanical responses of the pavement test sections with embedded components through the use of Finite Element Models (FEM). The layer configuration of the pavement sections was replicated in the Abaqus software, and each layer was assigned conventional

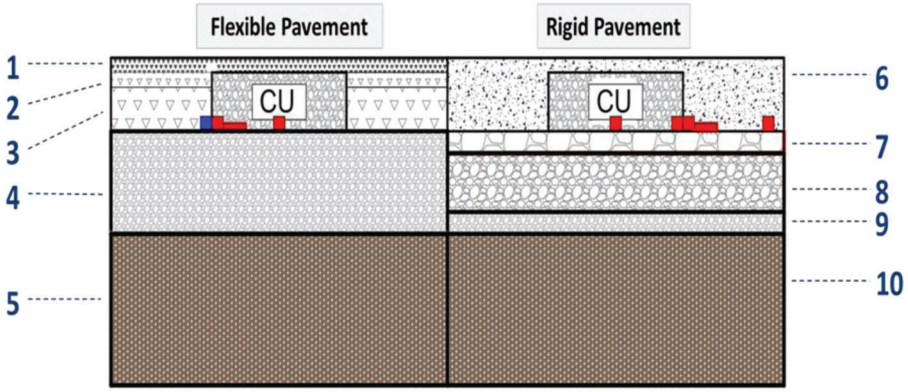

Figure 4.6 Cross section of pavement test sections.

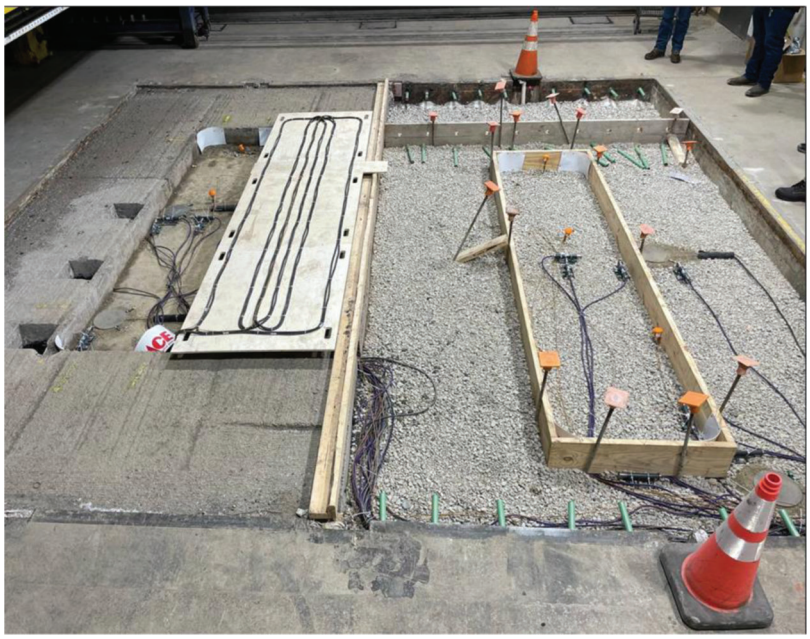

Figure 4.7 Top view of both test sections of the DWPT unit prior to material placement.

TABLE 4.1
Test Sections Layer Configuration Dimensions

Flexible Pavement Layers		Rigid Pavement Layers	
2 in.	9.5 mm HMA Surface	10 in.	PCC
2 in.	19.0 mm HMA Int	3 in.	#8 aggregate
6 in.	19.0 mm HMA Base	6 in.	#53 aggregate
14 in.	1Lime Stabilized A-6	5 in.	Lime Stabilized A-6
48 in.	A-6 Subgrade Soil	48 in.	A-6 Subgrade Soil

material properties. A dual tire loading configuration was used to apply a load of 9,000 lbs. Two combinations of flexible and rigid pavement models, with and without an embedded DWPT unit were considered, as shown in Figure 4.8. To predict the mechanical impact of incorporating the DWPT unit into the pavement structure, the modeling effort produced mechanical responses such as stress, deflection, and strain.

Critical loading locations leading to higher levels of structural damage across the pavement were identified by comparing the mechanical responses when the dual tire was positioned at varying lateral distances from the edge of the DWPT unit. Two tire placement scenarios were considered, edge of tire placement and mid-tire placement (center of the dual-axle configuration), as illustrated in Figure 4.9. This criterion guided the selection of the appropriate locations for placing the instrumentation at the APT facility and for selecting the critical points of interest for the different testing procedures.

The model results demonstrated that the placement location of the tire, whether at the center or the edge of the DWPT unit, influences the strain distribution across the pavement layers. A more pronounced distribution is

Figure 4.8 (a) Cross section of traditional pavement, and (b) cross-section of pavement with embedded DWPT.

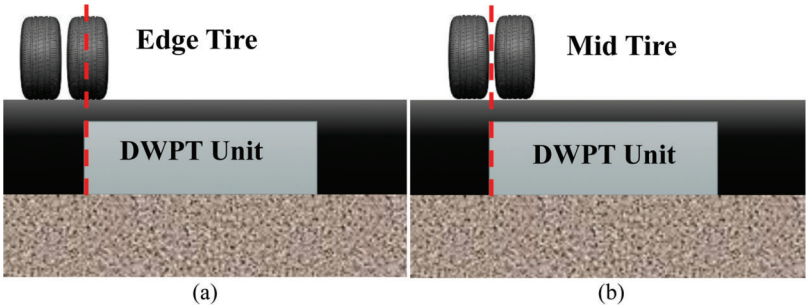

Figure 4.9 Dual-axle wheel placement scenarios: (a) edge tire placement, and (b) mid tire placement.

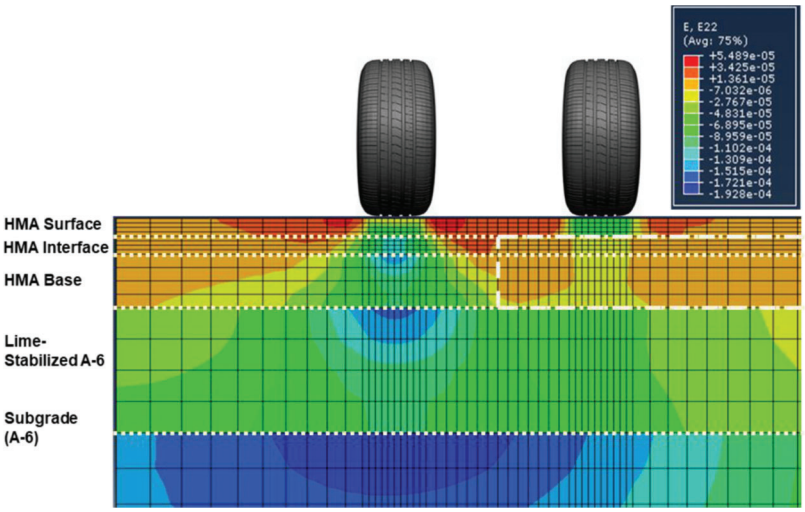

Figure 4.10 Vertical strain distribution: dual-axle wheel placed over the edge of the embedded DWPT unit (UTEP).

observed at the edge where the different materials interface, potentially impacting the expected performance and durability of the pavement. Figure 4.10 illustrates an example of the predicted vertical strain under an applied load over a flexible pavement with an embedded DWPT unit. Tensile behavior is represented by positive values, while compressive behavior is represented by negative values. The model shows that compressive vertical strain develops under the tire as it applies pressure to the pavement surface. However, rather than dissipating the strain evenly throughout the layers, as would be observed in a traditional pavement structure, higher levels of strain are concentrated at the 2-in. HMA surface layer due to the stiffer nature of concrete. Parallelly, high tensile strain concentrations were observed at the edge of the DWPT unit. These areas experiencing tensile strain can lead to upward movement on the surface of the flexible pavement, commonly known as heaving.

4.3 Structural Instrumentation

The sensor instrumentation used to evaluate the pavement's response from both test sections consists of 6 strain gauges within the asphalt (Figure 4.11), 5 strain gauges in the flexible section's DWPT unit, 15 strain

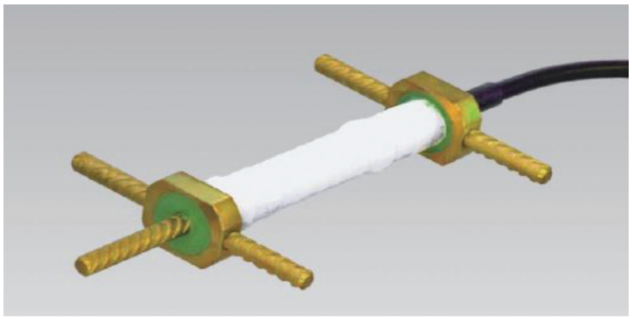

Figure 4.11 Strain gauge embedded in asphalt.

Figure 4.12 Strain gauge embedded in concrete.

Figure 4.13 Earth pressure cell.

gauges in the rigid section (Figure 4.12), 4 earth pressure cells (Figure 4.13) and 18 type K thermocouples (Figure 4.14). The strain gauges and pressure cells were connected to a data acquisition system and reviewed to determine their stability, responsiveness in neutral condition, and external tension or compression stimulus. The data acquisition computer is interfaced with two Vishay Micro-Measurement System model 6000 scanners for capturing and processing the data, as shown in Figure 4.15. Each scanner has 20 input channels with a maximum sampling rate of 10 kHz. By installing four thermocouple cards (model 6020), 20 strain gauge cards (model 6010), and five high-level cards (model 6030), four thermocouples, eighteen strain gauges, and five load cells are monitored simultaneously. The thermocouples are connected to a printed circuit board with 16 channel capacity, as shown in Figure 4.16.

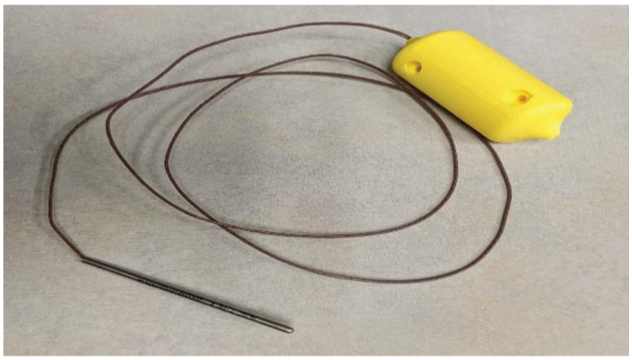

Figure 4.14 Thermocouple type K.

Figure 4.15 Model 6000 scanner.

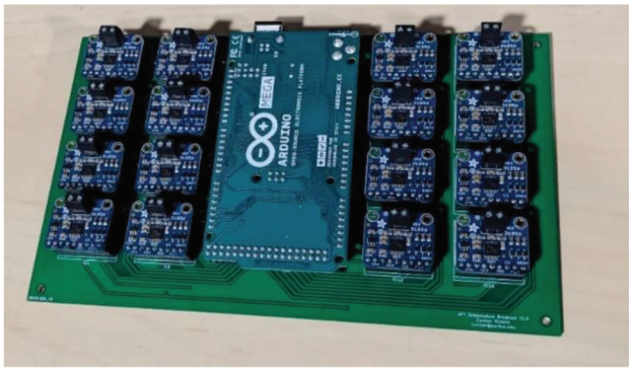

Figure 4.16 Thermocouple circuit board.

The strain gauge sensors were embedded 10-in. underneath the surface layer, directly above the lime stabilized soil, to measure transverse and longitudinal strains at the edges of the DWPT unit. The earth pressure cells were placed 10-in. beneath the surface layer to monitor the subgrade's response to the traffic load and the DWPT system. The thermocouples Type K were placed at different depths within the pavement to measure the temperature distribution within the layered configuration, as shown in Figure 4.17. Nine thermocouples were placed within the flexible pavement section (Table 4.2), while ten thermocouples were placed within the rigid pavement section (Table 4.3). The thermocouples are connected to an Arduino Mega

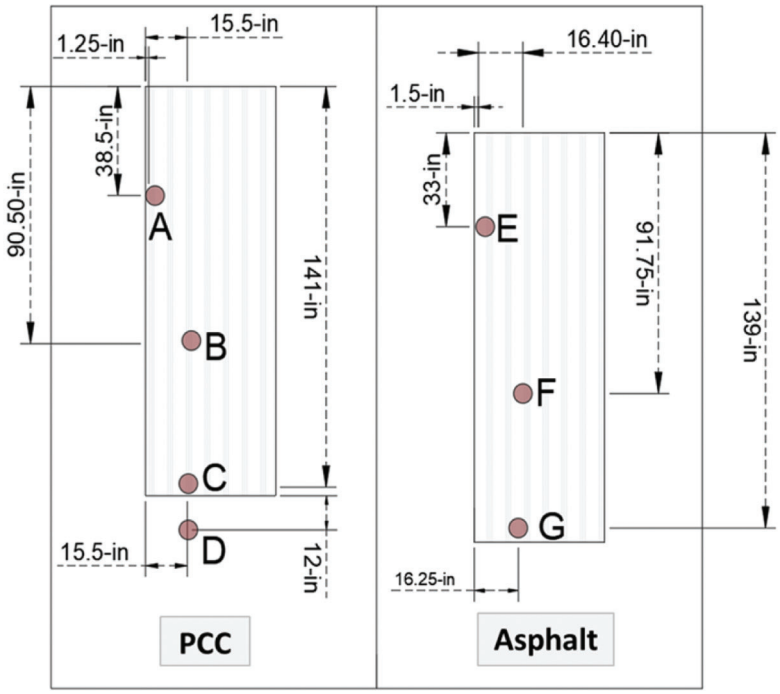

Figure 4.17 Thermocouple placement.

TABLE 4.2
Thermocouples Within Flexible Pavement (Location, Label, and Depth from Surface)

Location	TC #	Depth from Surface [in.]
E	14	3
E	5	4.75
E	12	7.5
F	13	3
F	1	6
F	2	8.5
G	15	3
G	3	7.25
G	4	9

TABLE 4.3
Thermocouples Within Rigid Pavement (Location, Label, and Depth from Surface)

Location	TC #	Depth from Surface [in.]
A	18	3
A	7	4.75
A	11	6.5
B	17	3
B	10	5.75
B	6	7.5
C	16	3
C	9	4.8
C	8	6.5
D	19	4

2560 microcontroller via a data acquisition circuit board. This information is then transmitted to a graphical user interface (GUI) on a computer through a USB power isolator.

5. CONSTRUCTION OF PAVEMENT SECTIONS

This project involved the construction of a flexible and a rigid pavement, both embedded with DWPT components. Execution of this task required detailed planning and clear communication between all the entities involved, given the complex design elements and specific geometric constraints involved. Coordination with INDOT was essential in efficiently managing the construction activities between the different entities involved: the research team, contractor, construction staff, and material suppliers. The construction personnel had to be attentive of detail and extra cautious during the construction operation due to the instrumentation placed and the DWPT components to be embedded. Furthermore, due to the workers' unfamiliarity with the specific pavement design required for the operation, it was essential to ensure clear communication in conveying detailed instructions about manual construction procedures. This included guidance on the precise placement of the tx-coil and the careful approach needed during compaction to avoid damaging any components or sensors. Thus, the installation of the DWPT components required careful handling and placement, as the accurate installation

and placement of the components could influence the wireless power transmission or the mechanical behavior of the structure. Table 5.1 illustrates the construction operation schedule.

5.1 Flexible Pavement Section

As the APT facility housed flexible pavement test sections from a previous INDOT study, the construction of the flexible pavement began by removing 2 in. of the asphalt surface of the existing flexible pavement. A conventional milling machine was employed for this procedure, as shown in Figure 5.1. Once the surface milling was complete, the DWPT unit cross section measuring 12 ft. long and 4 ft. wide was excavated with a crawler excavator (Figure 5.2) to a depth of 8 in. above the lime-treated soil.

The cross section of the flexible section prior to the installation of the DWPT unit is illustrated in Figure 5.3. Considering the geometric constraints of the flexible section, including the embedment of the DWPT unit and the borders of the facility's pit, and given that only 2 in. were milled from the surface, three square spaces of 1 ft. by 1 ft. with a 10-in. depth were milled at the edge of the flexible section's DWPT unit. This approach facilitated the placement of strain gauge sensors 10 in. into the ground, ensuring no damage to the rest of the structure. Seven strain gauge sensors were installed within the flexible pavement and five strain gauges within the DWPT unit, as shown in Figure 5.4. After the sensor installation, the strain gauge sensors were covered with cold mix asphalt, safeguarding them from potential damage during the remaining construction process and securing their stable placement. The choice of cold mix asphalt for this purpose was due to its versatility and ease of application. It has excellent adhesive qualities and quick setting time, providing a protective layer for the

TABLE 5.1
Construction Schedule

Dates (2022)	Task
April 18th	Demolition of the existing pavement
April 18th	Surface milling of existing flexible pavement
April 19th	Placement of the aggregate layers
April 25th–May 2nd	Sensor instrumentation placement
May 2nd	Cast concrete for flexible pavement's DWPT unit
April 26th	Placement of plywood forms on rigid pavement
May 2nd	Cast concrete for rigid pavement's DWPT unit
May 9th	Placement and compaction of asphalt surface
May 9th	Concrete casting for rigid pavement
May 11th–June 3rd	Sampled concrete materials

Figure 5.2 Crawling excavator used to excavate the DWPT unit cross section.

Figure 5.1 Milling machine used to mill the existing asphalt section.

Figure 5.3 Flexible section after milling 2 in. from the surface and excavating the DWPT unit geometrical space.

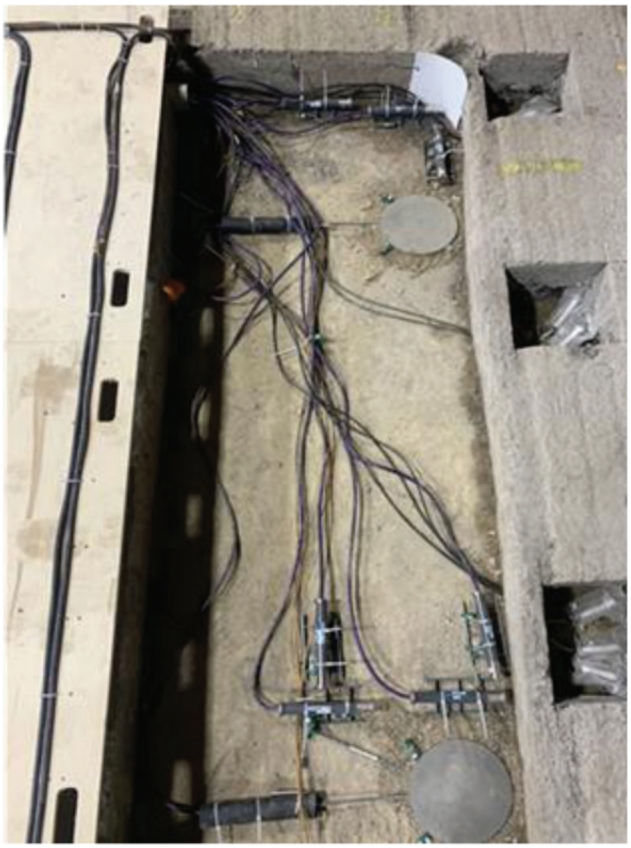

Figure 5.4 Sensor instrumentation placement.

embedded sensors and reducing the time needed for the cold mix to completely harden.

After the sensor instrumentation was placed and their connections to the data acquisition system were ensured, the excavated cross section of the DWPT unit was filled with 8 in. of Class C concrete, as shown in Figure 5.5. To guarantee accurate placement of the DWPT components, the two-turn tx-coil was positioned on plywood and secured with zip ties. Right after the Class C concrete was placed, the plywood was flipped to ensure the components were precisely 2 in. below the pavement surface, as illustrated in Figure 5.6. The board was then carefully removed by cutting the ties and freeing the components.

A tack coat was applied to the surface before the paving operation to ensure adhesion between the existing layer and the new asphalt surface course, as depicted in Figure 5.7. A conventional asphalt paver machine was then used to place 2 in. of the new HMA surface course, ensuring uniform distribution of the asphalt layer, as shown in Figure 5.8. The freshly laid surface course was compacted using a dual-drum vibratory roller, as illustrated in Figure 5.9. To achieve optimal density, the roller was operated in vibratory mode. Each roller pass consisted of one forward and one backward movement. For this operation, the roller made 6 complete passes, totaling 12 individual passes, across the flexible pavement. During the paving operation, the target density of the HMA surface layer was set to 93%, as specified by INDOT. The density of

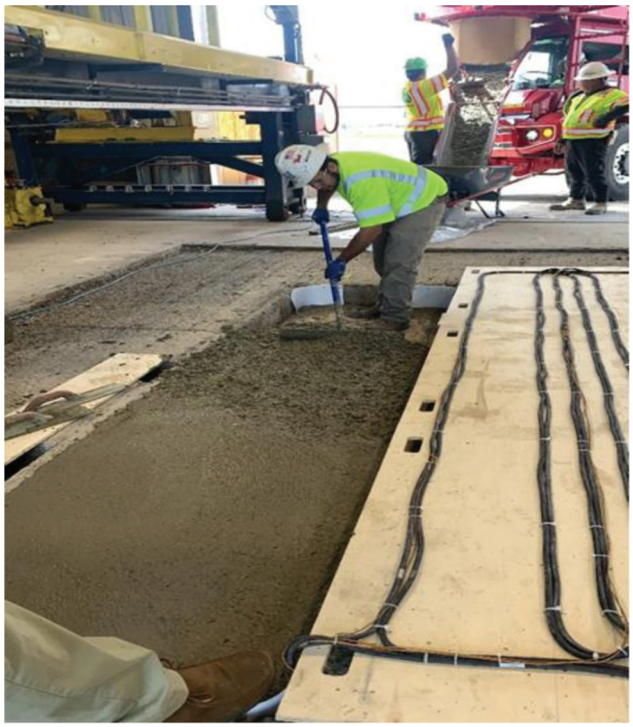

Figure 5.5 Class C concrete casted into flexible pavement.

the 2-in. HMA surface course was measured in accordance with the standard method of test for percent air voids in compacted asphalt mixtures (AASHTO, n.d.), for which four specimens were prepared and tested. The target density was achieved by all of the tested specimens from the HMA surface course, yielding an average percent density of 94.5%. The flexible pavement test section after construction is shown in Figure 5.10.

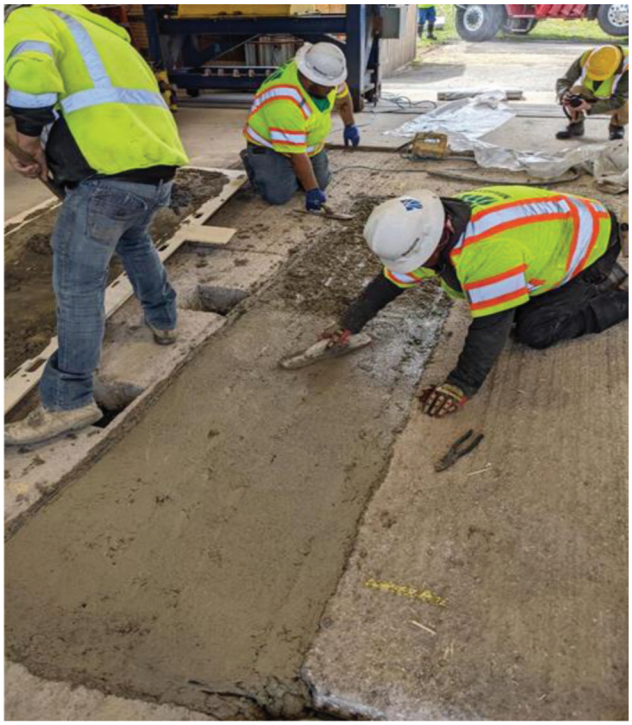

Figure 5.6 Placement of coils over concrete.

5.2 Rigid Pavement Section

Construction of the rigid pavement section started with the demolition and removal of the existing flexible pavement structure from the previous project. For this step, jackhammers and a crawler excavator were used to break apart and excavate the existing pavement to a depth of 24 in., as depicted, in Figure 5.11. Following this, the subgrade surface was smoothed and compacted prior to the placement of a 6-in. layer of fine-graded #53 aggregate, topped by a 3-in. layer of coarse-graded #8 aggregate, as illustrated in Figure 5.12. The layers of #53 aggregate and #8 aggregate were consolidated using a plate compactor machine, as shown in Figure 5.13. Plywood was used to designate the joint segment and the geometrical borders of the DWPT unit. Within the joint outlined by the plywood, ten dowel bars were placed, and another ten were positioned at the transverse edge of the pit, as depicted in Figure 5.14.

Twenty strain gauges were placed over strongback bolster uppers, each 1.25 in. thick, to ensure stable and secure placement. Following the installation of the sensors, as illustrated in Figure 5.15, their wires were

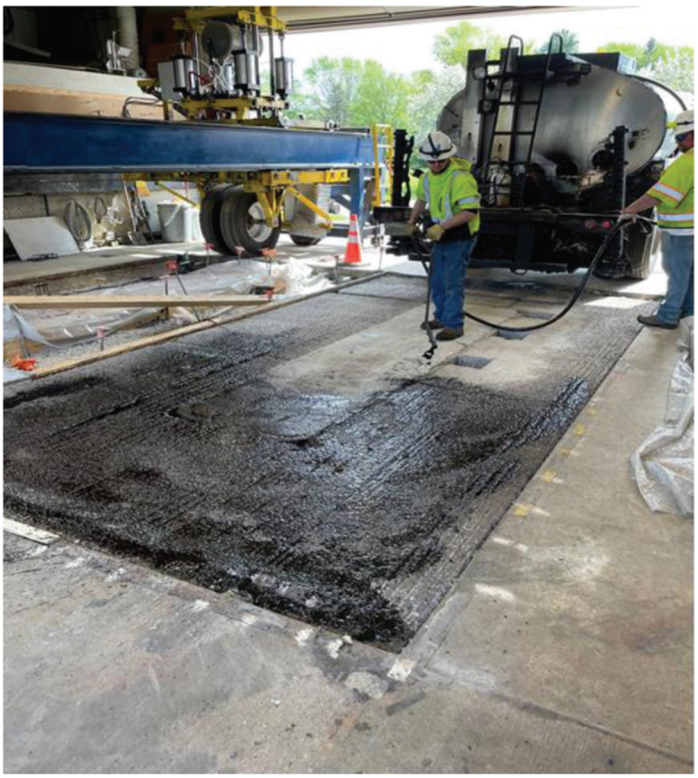

Figure 5.7 Placement of tack coat interface.

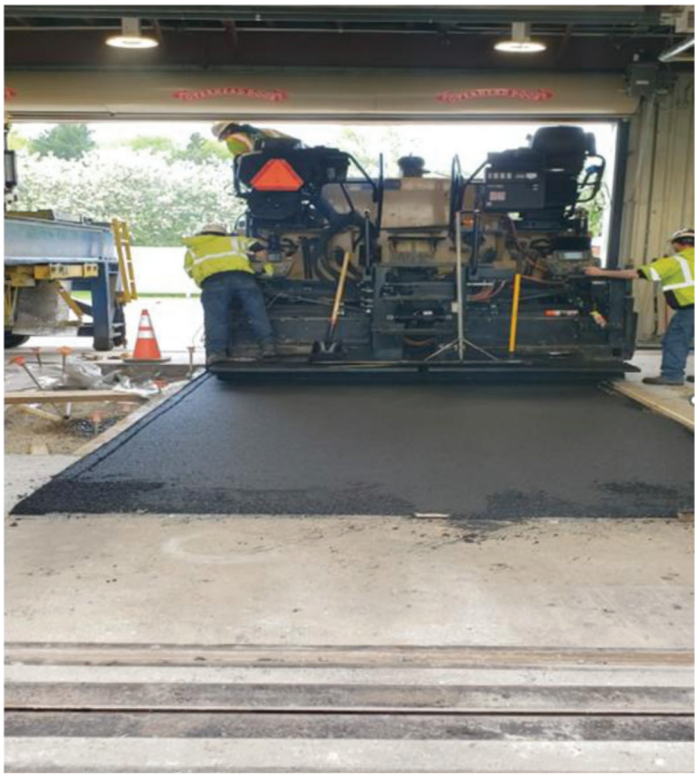

Figure 5.8 Placement of 2-in. HMA surface using asphalt paver.

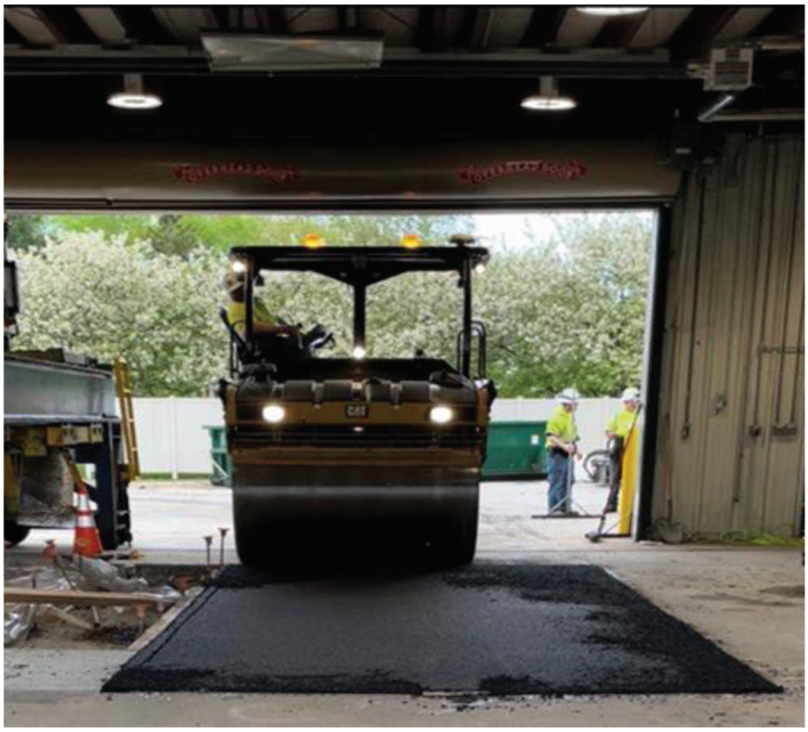

Figure 5.9 Compaction of asphalt course with dual-drum vibratory roller.

Figure 5.10 Flexible pavement section after construction.

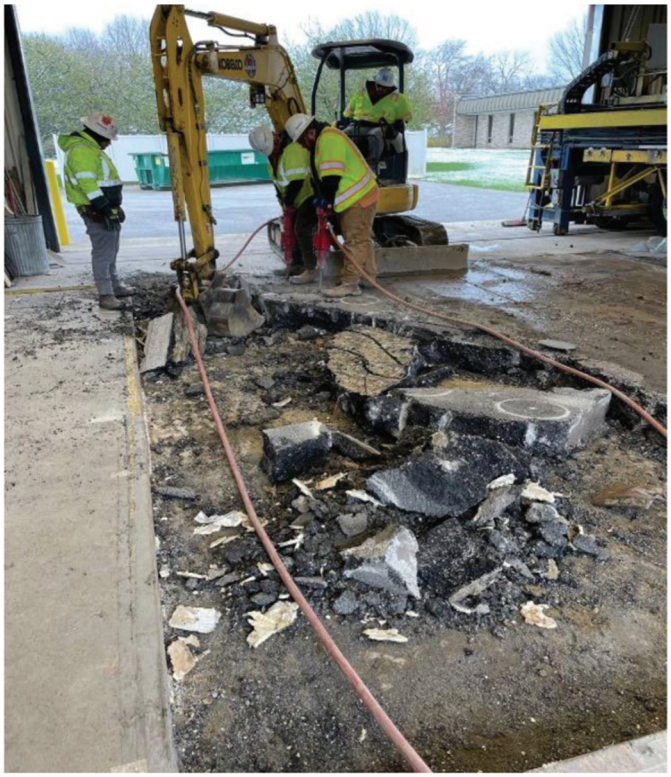

Figure 5.11 Demolition of existing pavement.

routed to the control room for connection to the data acquisition system. This was proceeded by calibration and testing of initial response for each sensor. Once the sensors were placed and tested, Class A PCC was poured for the 4-ft. long joint slab and magnetizable concrete was poured over the rigid pavement's DWPT unit, as shown in Figure 5.16 and Figure 5.17. Extra caution was employed by the construction workers over the entire process due to the presence of instrumentation in the base layer.

The magnetizable concrete used for this project marked the first time it was used for a cast-in-place scenario, as it is typically used for pre-cast slabs. The mixing and placement procedures were handled by the paving contractor. To ensure quality control, a special mixing truck, often used for polymerized concrete mixing for bridge decks, was used to mix the magnetizable concrete in-place. Given the nature of this material, any discrepancies in mixing or handling could potentially alter its performance over the design life.

Figure 5.12 Placement of #8 aggregate.

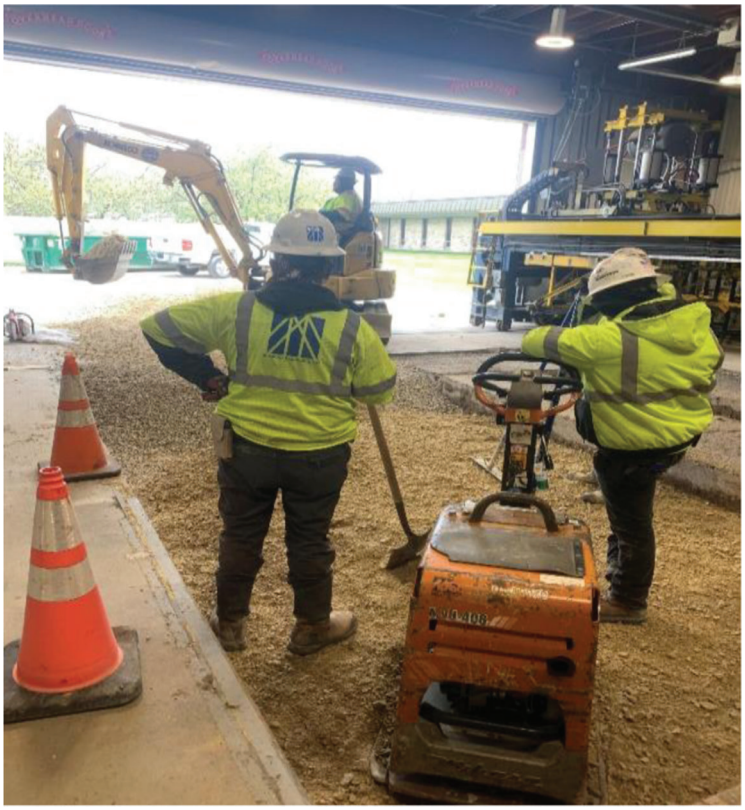

Figure 5.13 Plate compactor used to stabilize aggregate.

Figure 5.14 Plywood used to denote DWPT unit and joint geometry.

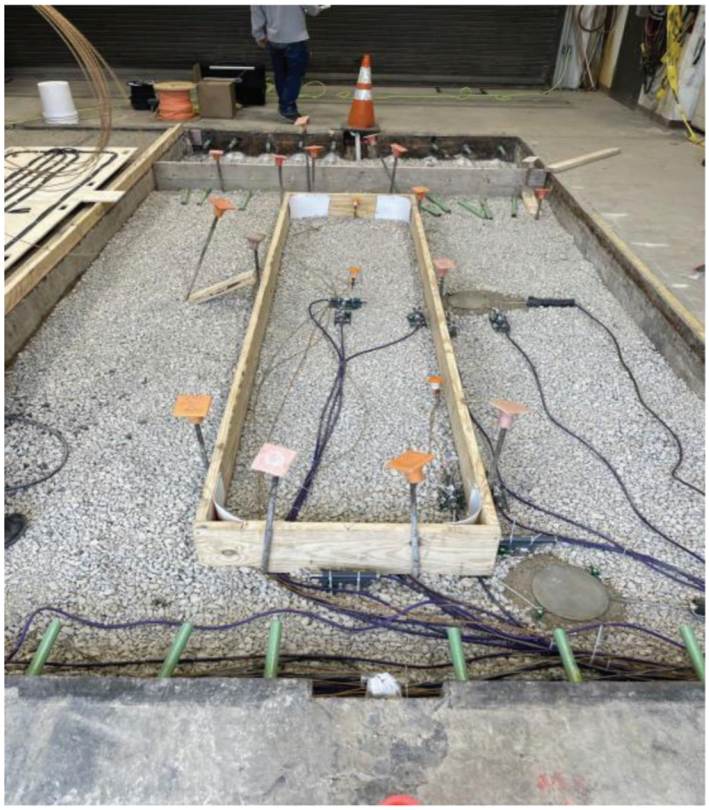

Figure 5.15 Placement of sensor instrumentation and plywood used to denote DWPT unit and joint.

Figure 5.16 Class A concrete poured into joint.

Figure 5.17 DWPT unit made of magnetizable concrete.

Consequently, the potential for faulty construction emphasizes the need for stringent quality control measures to ensure the structural integrity and success of these types of projects.

The DWPT coils were attached to plywood and secured in place with zip ties. Following the placement of the magnetizable concrete into the DWPT unit form and a 1-week curing period, the plywood was carefully flipped over, and the tx coil was positioned above the magnetizable concrete. This step was vital to ensure the precise alignment of the two-turn tx coil. Subsequently, the zip ties were then cut to detach the board. In the final stage, Class A concrete was poured into the remaining areas surrounding the DWPT unit. Right after the concrete was poured, a power vibrator was employed to ensure the removal of air pockets and to achieve a consolidated, uniform concrete matrix. Workers took extra precautions to avoid any disruption to the instrumentation or the embedded components, as shown in Figure 5.18. The completed rigid pavement section is shown in Figure 5.19.

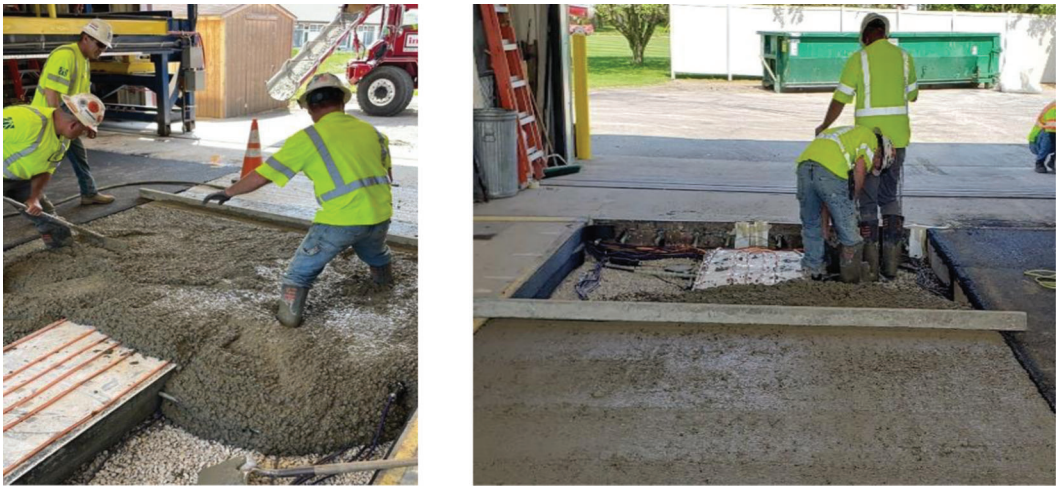

Figure 5.18 Class A concrete placement.

Figure 5.19 Rigid pavement test section after construction.

6. RESULTS

6.1 Experimental Testing of DWPT Electrical System

Operating the DWPT system with a 750 V dc input yielded an output power (P_{load}) of 52 kW. Figure 6.1 displays the plotted measured phase currents of the transmitter and receiver, as well as the load power. The balance between phase currents is evident, and the observed 7.2% power ripple aligns closely with the characterized σ value.

To assess the sensitivity of the proposed three-phase DWPT topology to misalignment, simulations were conducted by incrementally offsetting the receiver center from the transmitter center, ranging from -20 in. to 20 in. in 0.4-in. intervals. The simulations assumed full coverage of the receiver by the transmitter, with a constant resistive load of 2.7 Ω to maintain an output power of 200 kW under perfect alignment. All presented simulation results pertain to steady-state operation. Figure 6.2 illustrates the average power and power ripple at the load versus misalignment for both magnetized-based and coreless designs. In the perfect alignment scenario, the power ripple, indicated by shaded regions, is attributed solely to rectification; beyond this, phase imbalance becomes a factor. The $\pm 20\%$ misalignment band is marked in Figure 6.2, showing that within this range, the performance of magnetized-based and coreless designs is quite similar. Outside this band, the magnetized-based system experiences a more rapid decline in output power, although the impact is not drastic. A notable distinction is the magnetized-based design's heightened sensitivity to the direction of offset. The asymmetry in the field distribution across the widths of the transmitter and receiver cores, due to the 90° phase lead of transmitter currents over receiver currents, is a contributing factor. Despite this directional bias, the coreless system's performance exhibits nearly symmetrical behavior about the aligned

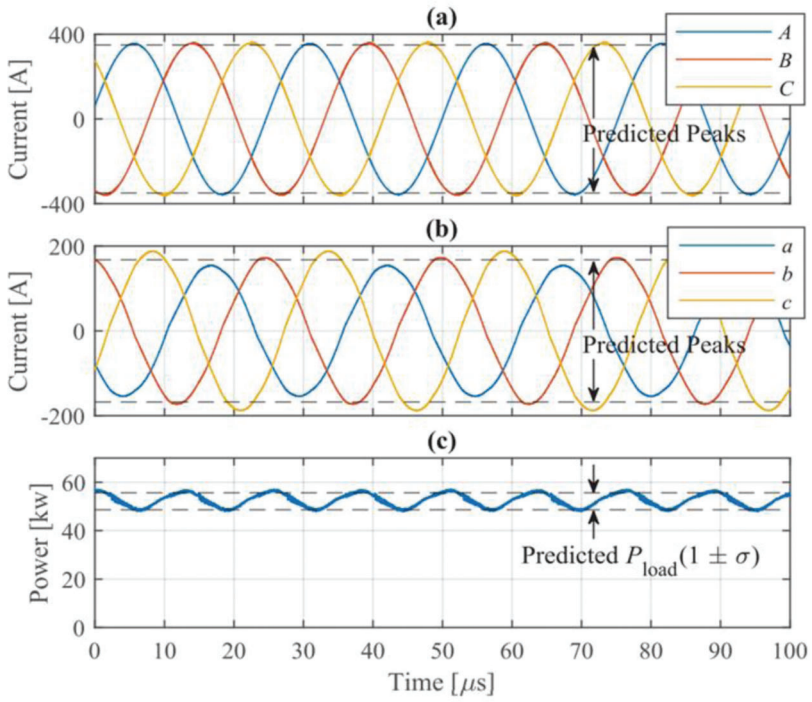

Figure 6.1 (a) Transmitter currents, (b) receiver currents, and (c) load power in prototype test (Brovont et al., 2023).

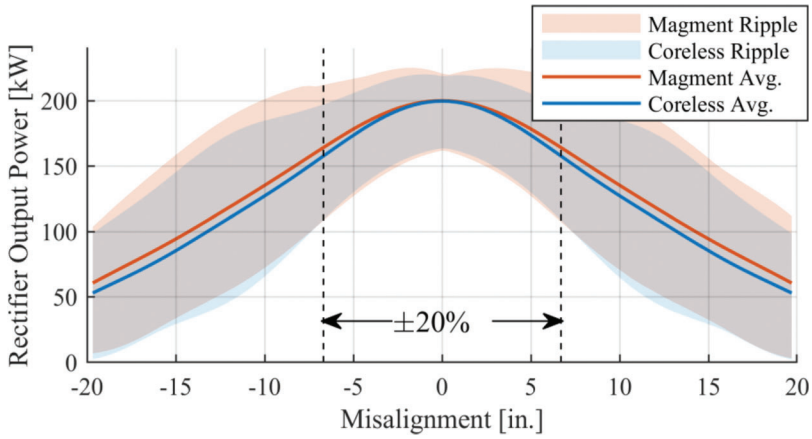

Figure 6.2 Steady state output power vs. misalignment for resistive load (Brovont et al., 2022).

position, whereas the magnetized-based system does not.

Figure 6.3 presents the root mean square (rms) amplitudes of induced receiver currents for both magnetized-based and coreless systems. Figure 6.3(a) reveals an intriguing characteristic of the coreless system, where, at extreme misalignments, the *a*-phase current tends toward zero. The *b*- and *c*-phase current amplitudes converge, with 180° phase angle displacement. Figure 6.3(b) underscores the magnetized-based system's stronger dependence on the offset direction. The portion of the coil closer to the transmitter acts as a single-phase pickup, directing the induced current to return through the farther portions of the coil. Consequently, the outer portions of the coils exhibit behavior akin to an equivalent single-phase double-D winding at significant misalignment.

6.2 Material Properties

6.2.1 Asphalt Paving Materials

Information about the asphalt mixture design, aggregate size, and PG are presented in Table 6.1. The 9.5-mm HMA surface mixture had a performance grade (PG) of 64-22, a conventional mixture PG used for surface courses in Indiana. The intermediate and

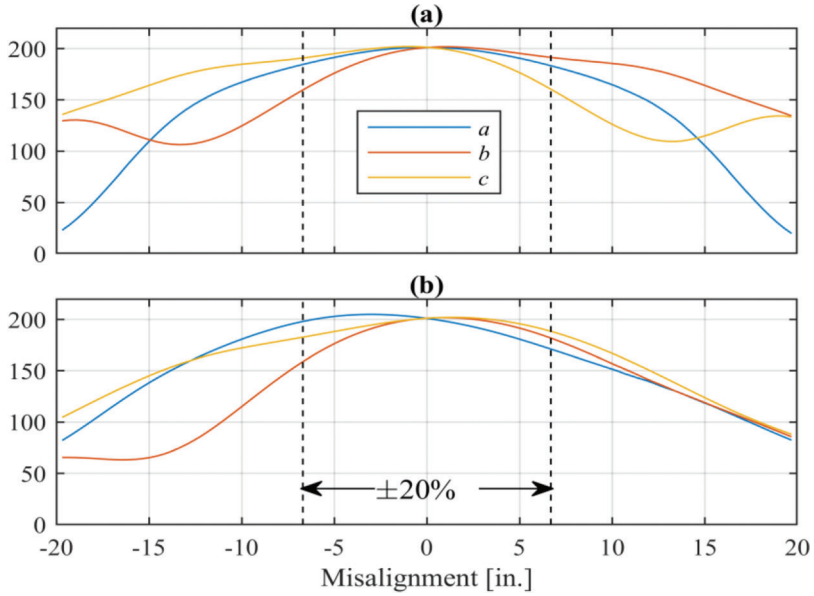

Figure 6.3 Steady state receiver phase current amplitudes vs. misalignment for (a) coreless, and (b) magnetizable core designs (Brovont et al., 2022).

TABLE 6.1
Mixture Design Summary

Layer	Mixture Type	Binder Performance Grade (PG)
Surface	9.5 mm	64-22
Intermediate	19.0 mm	70-22
Base	19.0 mm	64-22

TABLE 6.2
Aggregate Gradations for Pavement Layers

	Surface Dense Graded HMA		Intermediate/Base	
Sieve Size	**% Passing**	**Spec**	**% Passing**	**Spec**
12.5 mm (1/2″)	100	–	100	<90
9.5 mm (3/8″)	97.3	90-100	87.2	–
4.75 mm (No. 4)	75.4	<90	35.2	–
2.36 mm (No. 8)	49.8	32-67	21.3	23-49
1.18 mm (No. 16)	35.2	–	16.3	–
0.6 mm (No. 30)	23.9	–	13.4	–
0.3 mm (No. 50)	12.6	–	11.8	–
0.15 mm (No. 100)	6.6	–	10.7	–
0.075 mm (No. 200)	5.0	2-10	8.2	2-10

base mixtures, while both being 19.0-mm mixtures, vary in binder type with PGs of 70-22, and 64-22, respectively. The aggregate gradation information for the pavement layers, along with corresponding specification control points as specified by INDOT, are presented in Table 6.2. The detailed properties and characteristics of the 2-in. HMA surface mixture used for this study, including binder content, aggregate angularity, and relevant test results, are outlined in Table 6.3.

6.2.2 Concrete Flexural Strength

Flexural strength testing was conducted in accordance with the guidelines of ASTM C78/C78M-22 (ASTM, 2022b). This test involved applying a load at the center of a prismatic concrete specimen supported on two points and measuring the maximum load at the point of failure. This maximum load represents the flexural strength of the concrete. The flexural strength test results for the different concrete samples are

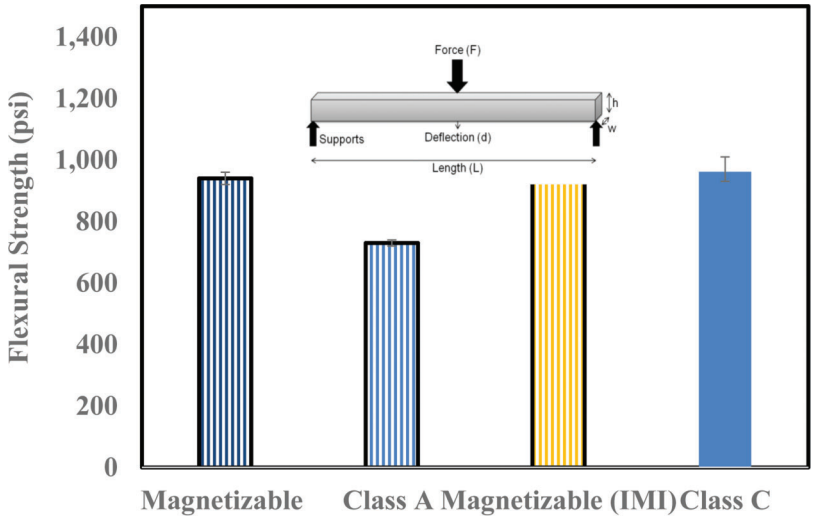

Figure 6.4 Flexural strength test results.

TABLE 6.3
9.5 mm HMA Surface Mixture Properties

Mixture Property	Value
Binder content, %	6.6
G_{mm}	2.487
G_{mb}	2.363
Density–lbs/ft^3	147.5
Air Voids Content, %	5.0
VMA, %	17.6
VFA, %	71.6
Tensile Strength Ratio, %	103.4

TABLE 6.4
Concrete Flexural Strength Test Results

Type of Concrete	Magnetizable	Class A	Class C
Maximum Flexural Strength (psi)	940.00	730.00	961.33

illustrated in Figure 6.4 and noted in Table 6.4. The maximum flexural strength of a material is defined as the maximum bending stress that can be applied to that material before it yields. The average maximum flexural strength values, represented in pounds per square inch (psi), were 940 psi for magnetizable concrete, 730 psi for Class A concrete, and 961.33 psi for Class C concrete. The highest average flexural strength was observed in the Class C concrete, followed by the magnetizable concrete. Class A exhibited the lowest average flexural strength among the samples tested.

6.3 Concrete Compressive Strength

Three samples were taken for each curing period (7, 14, and 28 days). The compressive strength test was conducted in accordance with ASTM C39/C39M-21 (ASTM, 2022a). It stipulates the use of cylindrical molds measuring 6 in. in diameter and 12 in. in height. Fresh concrete was poured into these molds, ensuring that there were no air pockets or inconsistencies. The concrete specimens were then consolidated by conducting 25 rod penetrations per layer as required by ASTM C39, ensuring thorough consolidation, and minimizing the possibility of voids. Figure 6.5 and Table 6.5 illustrate the compressive strength test results. The magnetizable concrete showed an average compressive strength increase from 5,210 psi at 7 days to 6,296 psi at 28 days. For Class A concrete, the average compressive strength increased progressively from 2,915 psi at 7 days to 3,673 psi at 28 days. The Class C concrete demonstrated a gradual increase in average compressive strength, from 5,237 psi at 7 days to 6,060 psi at 28 days.

6.4 Asphalt Dynamic Modulus

The dynamic modulus represents the stiffness of the asphalt mixture when subjected to oscillatory loading, highlighting its linear viscoelastic behavior (AASHTO, 2022). The dynamic modulus is determined by subjecting an asphalt mixture specimen to a sinusoidal stress at a specified temperature and loading frequency. The resulting strain is measured and used to calculate the dynamic modulus. Dynamic modulus testing is performed at various frequencies and temperatures to simulate a range of environmental conditions and loading speeds vehicles exert on the pavement. By analyzing the data through graphical representation, insights can be extracted regarding the mixture's performance over different seasons and traffic conditions. The frequency of applied stress in this test represents the speed of vehicles on the road, with lower frequencies correlating to slow or stationary traffic and higher frequencies indicating faster traffic (Witczak et al., 2002).

To calculate the load duration, procedures in accordance with the formulas provided by Huang (1993) and the specific characteristics of the accelerated

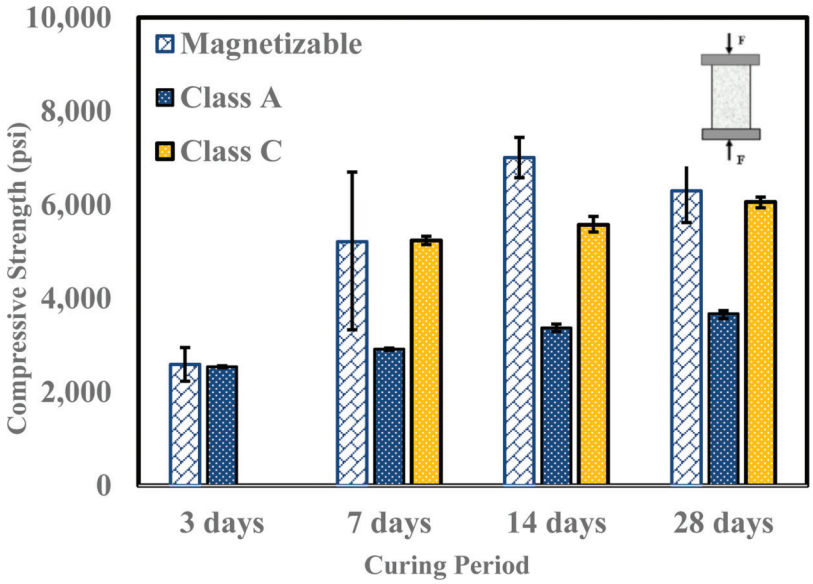

Figure 6.5 Compressive strength test results.

TABLE 6.5
Compressive Strength Test Results

Type of Concrete	Curing Period	Average Compressive Strength (psi)
Magnetizable	7 days	5,210.00
	14 days	7,010.00
	28 days	6,296.67
Class C	7 days	5,237.50
	14 days	5,573.33
	28 days	6,060.00
Class A	7 days	2,915.00
	14 days	3,370.00
	28 days	3,673.33

pavement testing machinery. Given the dual-axle wheel dimensions of 8 in. long and 7.5 in. wide, an applied load of 9,000 lbs, and a tire-induced stress of 100 psi, the tire contact radius a was determined from Equation 6.1, yielding a contact area of 0.625 ft^2 (90 $in.^2$). The determined contact area was subsequently used in Equation 6.2 to calculate the tire contact radius, yielding a value of 0.446 ft. (5.352 in.). Equation 6.3 displays the formula provided by Huang (1993) loading time, where d is the duration of the load (seconds), a is the tire contact radius (ft), s is the vehicle speed (ft/s). With the tire contact radius "a" established and the velocity assigned at 5 mph (7.33 ft/s), the duration of the load d was computed to be roughly 0.73 s. The frequency of the load cycles is defined as the number of times the load is applied and removed per second. The frequency of the load cycles is inversely proportional to the duration of the load, meaning that the frequency increases as the duration of the load decreases. As stated in (Huang, 1993), the frequency can be calculated using Equation 6.4, where f is the frequency (in Hz), and d is the duration of the load (in seconds). By replacing "d" with the value of 0.73 s, the computed frequency yields approximately 1.37 Hz.

$$Tire\ Contact\ Area = \frac{Load\ (lbs)}{Stress\ (psi)} \cdot \text{ft}^2 \qquad \text{(Eq. 6.1)}$$

$$Tire\ Contact\ Radius = \sqrt{\frac{Area}{\pi}} \cdot \text{ft} \qquad \text{(Eq. 6.2)}$$

$$d = \frac{12a}{s} \cdot \text{seconds} \qquad \text{(Eq. 6.3)}$$

$$f = \frac{1}{d} \cdot Hz \qquad \text{(Eq. 6.4)}$$

The Sigmoidal Master Curve graphically represents the dynamic modulus of asphalt mixtures over various frequencies and temperatures, enabling predictions for different loading and environmental scenarios. By fitting lab test data into the Sigmoidal Master Curve, the process becomes more efficient, reducing the number of required frequencies needed for testing. An adjustment for temperatures is necessary because the viscoelastic behavior of asphalt mixtures changes with temperature variations (Witczak et al., 2002). The Sigmoidal Master Curves are constructed at a reference temperature, typically 70, using the principle of time-temperature superposition. By applying this principle, data collected at various temperatures can be shifted logarithmically with time until the curves merge into a single smooth function. The resulting master curve, as a function of time, describes the time dependency of the material (Witczak et al., 2002). The adjusted dynamic modulus (E′ predicted) values presented were obtained through a curve fitting process using the maximus

limiting modulus and reduced frequency. This methodology allows for the estimation of the dynamic modulus values for the different layers at the given testing temperatures, distinguishing them from the experimental dynamic modulus values obtained directly from the tests.

At a frequency of 1.37 Hz, the dynamic modulus for each layer of the pavement structure is depicted in their respective figures—Figure 6.6 for the HMA surface layer Figure 6.7 for the intermediate layer, and Figure 6.8 for the base layer. In this study, the sensors were embedded 10-in. into the pavement, within the base layer. As such, the dynamic modulus for the base layer is of interest, as its extracted value obtained from the master curve can be used for the calculation of fatigue load cycles prediction. Based on a frequency of 1.37 Hz, the base layer denotes an adjusted dynamic modulus of approximately 4 MPa.

6.5 Pre-Traffic Test

Upon the completion of the construction of both the flexible and rigid pavement sections, three non-destructive tests were conducted: ground penetrating radar (GPR), falling weight reflectometer (FWD), and stationary loading. These tests aimed to capture the characteristics of the pavement section before accelerated pavement testing traffic was applied. The results from these tests were used to calibrate the finite element model responses developed by UTEP, enhancing the accuracy of predictions regarding the mechanical behavior of the pavement.

6.5.1 Ground Penetrating Radar (GPR)

As illustrated in Figure 6.9, the Ground Penetrating Radar (GPR) is a non-destructive testing method that employs electromagnetic waves for detecting subsurface objects or features within the soil and pavement layers. The device operates by emitting high-frequency electromagnetic waves into the ground and then receives the waves reflected back from the surface by the various subsurface materials. The device is equipped with a transmitting and a receiving antenna, allowing it to send and collect waves. Subsequently, it converts these responses into a 3D image of the pavement structure. For this project, one of the primary objectives of the GPR test was to observe the interaction between the electromagnetic waves and the magnetizable concrete used in the DWPT unit. GPR readings were conducted over the pavement sections in longitudinal and transverse direction. The non-destructive nature of the GPR test allows for a comprehensive inspection of the pavement without causing any harm to it.

6.5.1.1 GPR over flexible pavement. Figure 6.10 shows a longitudinal GPR reading taken at a distance of 1.5 ft. from the DWPT unit longitudinal edge. In the image, the y-axis corresponds to the electromagnetic waves' travel time emitted by the GPR, measured in nanoseconds, while the x-axis indicates the distance covered along the pavement surface. The sensors embedded in the pavement can be identified by the heavy or wave responses observed at the distances of 4–6 ft, 6–8 ft, and 10–12 ft. These responses align with the placement location of the sensors. Figure 6.11 illustrates a longitudinal GPR reading conducted over the DWPT unit, visibly identified along the x-axis from 5 to 17 ft. The distinctive wave disruption observed is attributed to the dielectric properties of concrete. As the electromagnetic waves emitted by the GPR system meet materials with varying dielectric properties, such as asphalt and concrete, they experience changes in their propagation characteristics. Concrete, with its high density and relatively lower permittivity compared to the surrounding asphalt, influences the reflective behavior of the electromagnetic waves. The disruption in wave propagation results in pronounced reflections and changes in signal intensity, clearly discernible in the GPR reading.

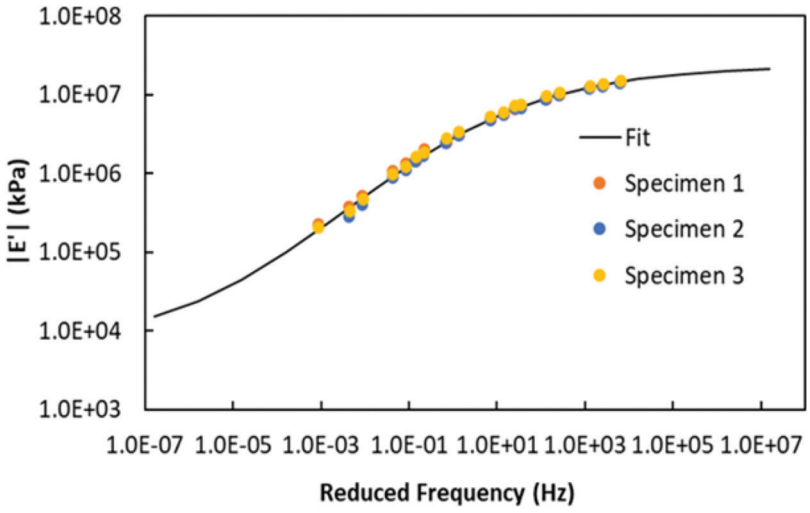

Figure 6.6 Sigmoidal master curve fit for HMA surface layer.

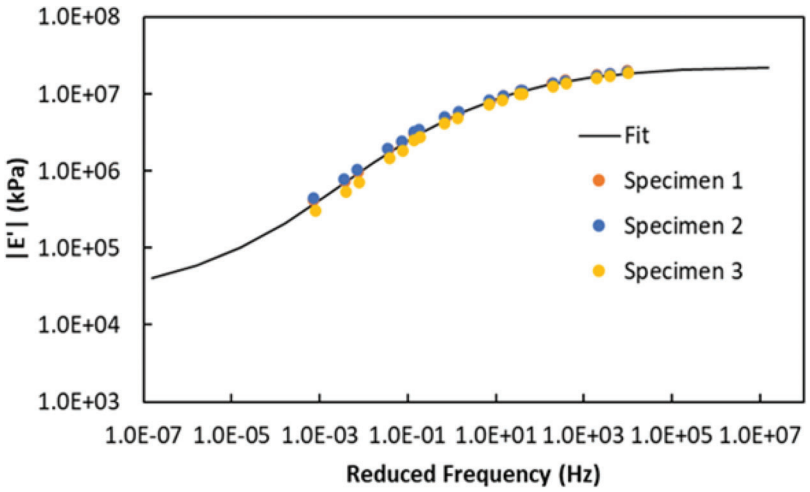

Figure 6.7 Sigmoidal master curve for intermediate layer.

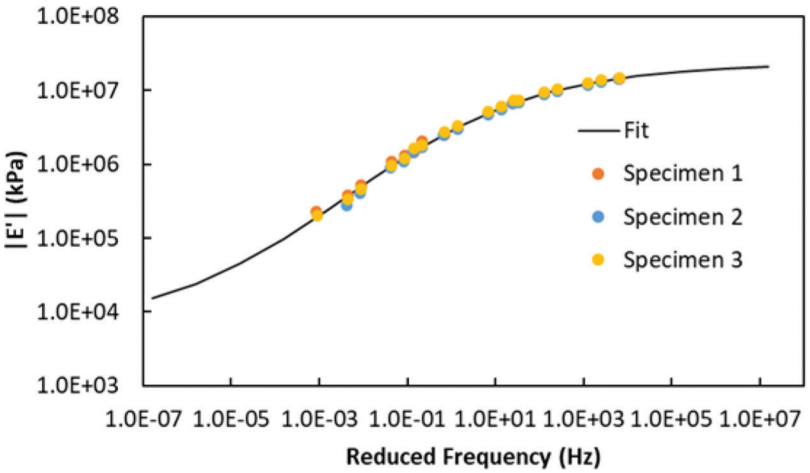

Figure 6.8 Sigmoidal master curve for base layer.

6.5.1.2 GPR over rigid pavement. In Figure 6.12, no clear response or disruption is observed in the longitudinal GPR reading conducted over a location in the rigid pavement without the DWPT unit underneath, indicating a relatively uniform and consistent subsurface composition of the concrete material. On the other hand, Figure 6.13 shows a longitudinal GPR reading over a concrete section with the DWPT unit present, where a notable response is observed from approximately 4 to 16 ft. along the x-axis, marking the DWPT unit's location. This response indicates a disruption in the subsurface composition caused by the presence of the DWPT unit within the concrete structure. Besides the contrasting responses between asphalt and concrete, another observation is the overall clarity of the GPR images in the concrete section. In contrast to the asphalt, where sensor responses and wave disruptions are distinct, the concrete sections show minimal or no sensor responses. The clean appearance in the concrete sections can be attributed to the lesser presence of reflected electromagnetic waves from various subsurface features, resulting in a GPR image that is clearer and less cluttered. The lack of sensor depictions in the concrete section highlights the wave disruptions caused by the DWPT unit. This interaction between the DWPT unit and the concrete material generates noticeable disruptions in the GPR signal, appearing as clear anomalies in the image.

6.5.2 Falling Weight Deflectometer

The falling weight deflectometer (FWD), illustrated in Figure 6.14, is a non-destructive test used for assessing the stiffness of pavements. The device operates by dropping a weight onto the pavement and measuring the resulting deflections in the pavement. The FWD test, designed to mimic the effect of a heavy truck wheel in motion, applies an impulse load to the pavement surface at three different levels: 7,000, 9,000, and 11,000 lbs. Nine geophones are placed longitudinally at various distances from the center of the FWD loading plate to measure the pavement's

response. The objective of the FWD test on this study is to provide an assessment of the pavement's structural condition before and after the application of 25,000 passes. Furthermore, the FWD test results were used to calibrate the FEM for accurate pavement performance prediction. To ensure accurate measurements, the FWD data obtained from the pavement sections was calibrated to account for variations in load and temperature conditions. This calibration was performed using the Indiana Department of Transportation (INDOT) FWD calibration software.

Figure 6.9 Ground penetrating radar (GPR).

6.5.2.1 FWD over flexible favement. FWD tests were performed at six locations over the flexible pavement, determined based on a numerical simulation using a finite element model (Figure 6.15). Location 0 was located in a full-depth asphalt zone, location 5 was in the middle of the DWPT unit, with the remaining locations being along the longitudinal and transverse edges of the DWPT unit. Two phases of FWD tests were performed, the first after construction of the section, before any traffic application, and the second after 25,000 passes had been applied. Although the test temperatures on the respective days differed, the temperature remained stable during each test phase. In order to compare the results of FWD deflections before and after accelerated pavement testing traffic, the results were load- and temperature-calibrated according to the methods outlined in AASHTO 1993 (AASHTO, 1993).

For the test points from 0 through 5, a decrease in deflections is observed after traffic, as shown in Figure 6.16. These observations closely mirror the findings of a prior study on a similar accelerated pavement testing study (Nantung et al., 2021). In their research, the authors reported higher deflection values before loading as compared to those after loading, pointing out that exposure to increased temperatures could be a reason for this decrease in deflections. Exposure to heat expedites the aging of the asphalt binder, leading to aging of the asphalt mixture and an overall increase in the pavement's stiffness. For the FWD data of this project, an explanation for this deflection reduction could be increased asphalt stiffness due to the waste heat potentially generated due to the constant current supplied to the embedded DWPT components during traffic testing. Furthermore, the decreased deflections may have been also influenced by a potential secondary

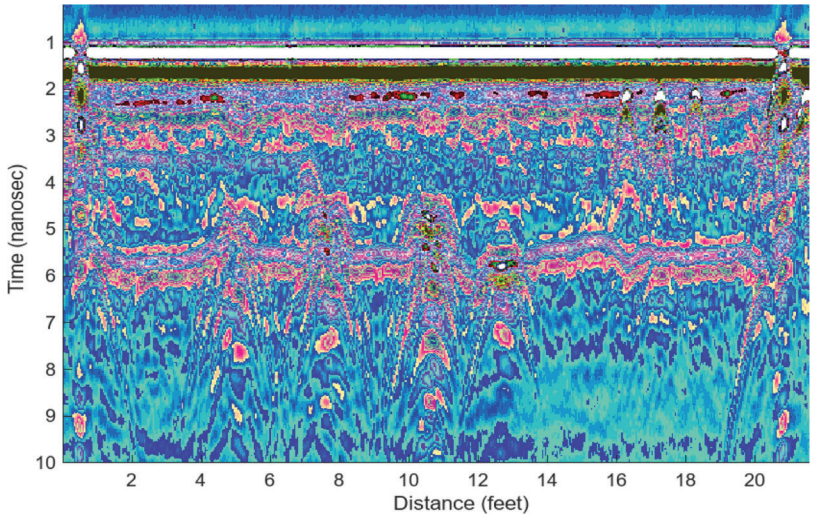

Figure 6.10 GPR longitudinal reading over full depth asphalt area (no DWPT unit).

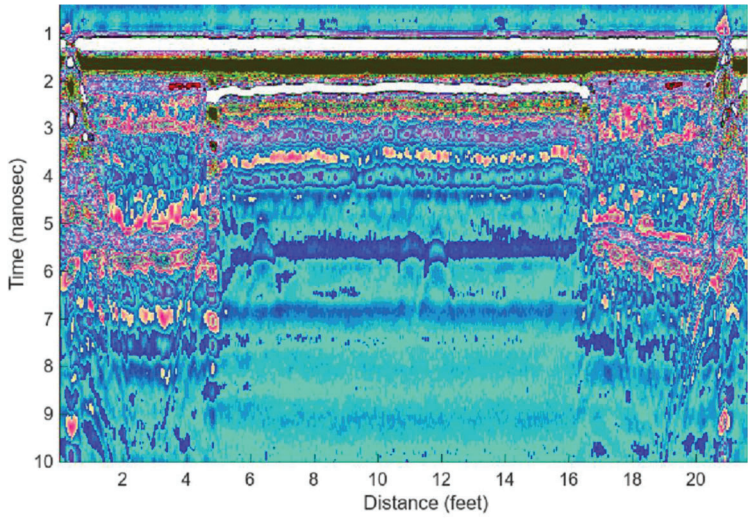

Figure 6.11 GPR longitudinal reading over flexible pavement DWPT unit.

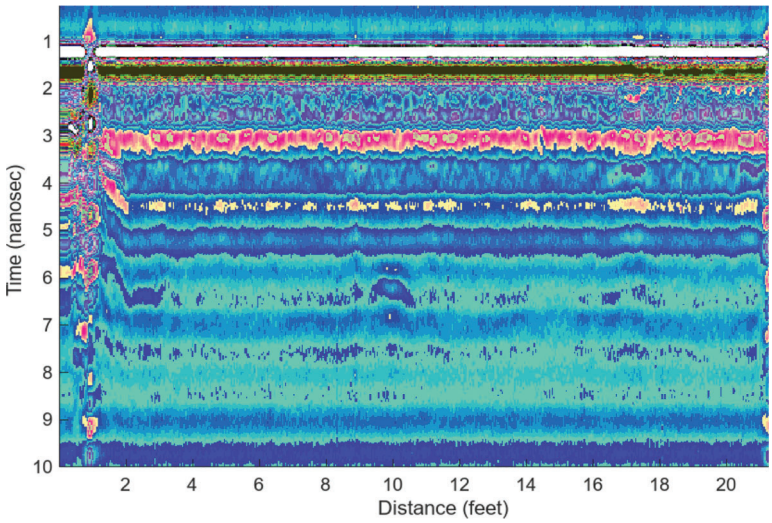

Figure 6.12 GPR longitudinal reading over rigid pavement (no DWPT unit).

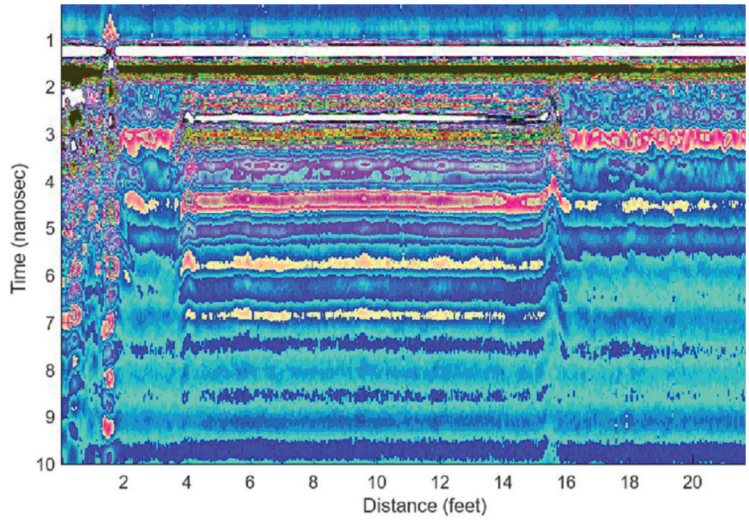

Figure 6.13 GPR longitudinal reading over rigid pavement DWPT unit.

Figure 6.14 Falling weight deflectometer (FWD).

compaction of the asphalt surface due to accelerated pavement testing traffic. As the asphalt layer undergoes further densification from the traffic, the internal voids within the pavement may decrease, leading to an increase in stiffness and a corresponding reduction in deflections.

6.5.2.2 FWD over rigid pavement. FWD tests were performed at six locations over the rigid pavement, determined based on a numerical simulation using a finite element model (Figure 6.17). Opposite to the flexible pavement's FWD results, the FWD data for the rigid section all test points, besides point 8, displayed an increase in deflections after traffic, as shown in Figure 6.18. This trend is typically indicative of the expected impact of traffic on pavement surfaces. Test points 6 and 9 denoted usual deflection values post-traffic, signaling stable structural performance in these sections. Contrarily, test point 8, positioned over the joint section, does not adhere to standard testing practices which don't recommend testing above a joint; thus, it was disregarded from further analysis. Distinctly, test points 7, 10, and 11 denoted distinct deviations. These points are situated over a transverse mid-panel crack and show markedly higher deflections, suggesting a reduction in the structural integrity around the crack. The formation of the crack will be discussed in detail in Section 7.2.

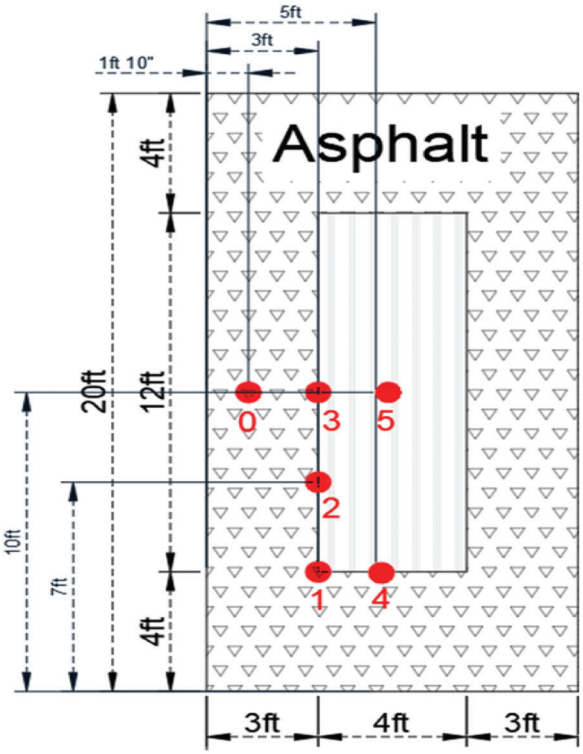

Figure 6.15 FWD and static load test positions based on FEM results.

6.5.3 Static Loading Test

The static load test was conducted to evaluate the strain distribution at the base of the flexible pavement due to the embedment of a concrete DWPT unit. The test involved applying a constant load with the dual tire loading configuration for 60 seconds at a temperature of 65°F, over the same test locations as for the FWD test (Figure 6.15), with the exception of Pt-5. During the load application, the sensors recorded for 60 seconds the transverse and longitudinal strains resulting from the load-induced stress. Once the load is removed, the sensors capture for 60 additional seconds the

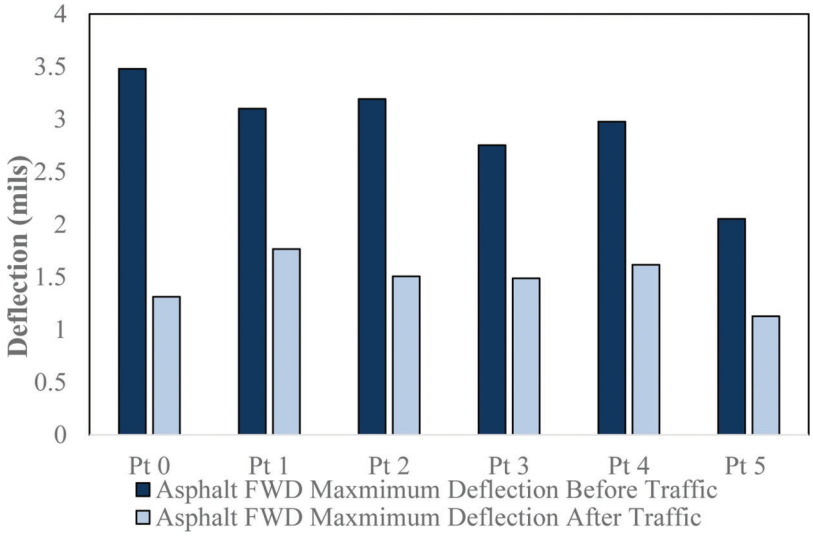

Figure 6.16 FWD over flexible pavement before and after 25,000 passes.

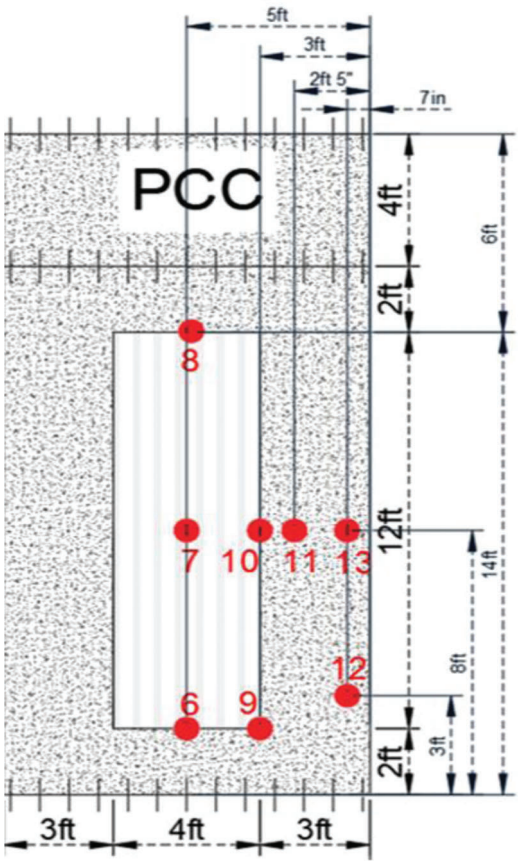

Figure 6.17 FWD and static load test positions over rigid pavement based on FEM results.

viscoelastic recovery. For each test point, two tire placement scenarios were considered: edge-tire (ET) placement and mid-tire (MT) placement (center of the dual-axle configuration). The collected sensor data was used to characterize the viscoelastic behavior of the asphalt material within the FEM simulations.

Figure 6.19 shows the asphalt strain gauges (ASG) results of Pt-3 for ET placement configuration. In the case of Pt 3, the ASGs used were #36, #35, and #34. Within the asphalt, the shape of deformation denotes a progressive increase in strain during the 60 s of static load application. As observed, the increase in strain was pronounced during the first seconds of loading but gradually stabilized until the 60 s mark. Following unloading, the strain recovery experiences a rapid decrease in the first seconds but also stabilizes until the 120 s mark. As observed, after 120 s of testing, a certain level of strain was not recovered and was considered as permanent deformation. This behavior highlights the viscoelastic nature of asphalt. On the other hand, Figure 6.20 illustrates the concrete strain gauge (CSG#26) result of Pt 3 for ET placement configuration, highlighting the contrast in strain response between both materials. As a consequence of the higher stiffness of concrete, not only were the peak strain levels notably lower, but the peak was also reached within the initial seconds of testing, followed by a slight decrease in strain attributable to the inherent creep behavior of concrete. When a consistent load is applied to the concrete, the strain levels may decrease due to the material's relaxation capability. Upon removal of the static load, the highly elastic nature of the concrete DWPT unit induces a quick recovery, resulting in a final deformation value that is nearly zero.

Since the plotted data for the remaining test points, collected from the other strain gauges within the asphalt and concrete, resemble those of Pt-3, the complete data considering ET and MT configuration for each testing point is summarized in the following figures: Figure 6.21 displays the result for Pt 0, Figure 6.22 for Pt 1, Figure 6.23 for Pt 2, Figure 6.24 for Pt 3, and Figure 6.25 for Pt-4. As observed in the different figures, for all test points except Pt-0, the ET placement configuration consistently showed the highest strain

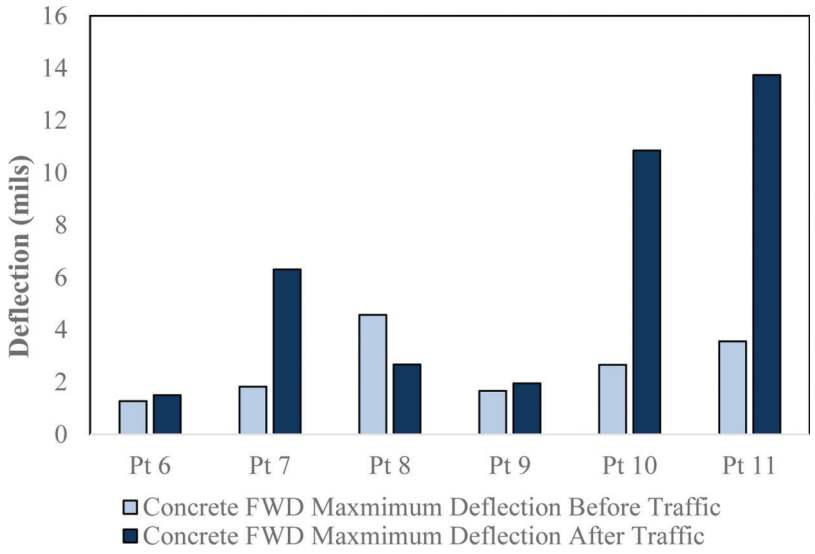

Figure 6.18 FWD over rigid pavement before and after 25,000 passes.

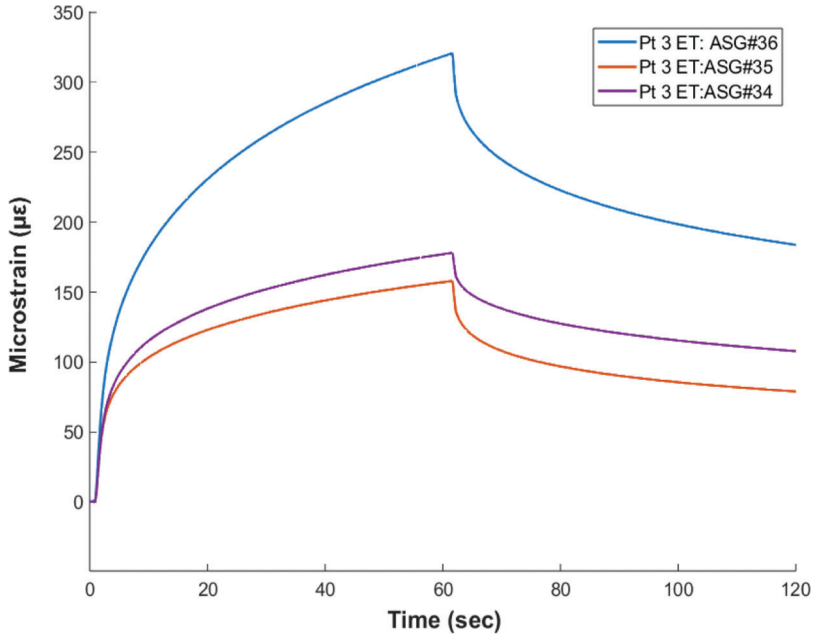

Figure 6.19 Strain development during static load test over location three ET scenario (asphalt strain gauge response).

measurements. Regarding Pt-0, since the ET placement was located further away from ASG sensors #34, #35, and #36, the levels of measured strains were considerably lower. However, given the placement of the sensor instrumentation, the sensors designated for Pt-0 were the nearest available option.

The difference in strain distribution between ET and MT placement is attributed to the fact that in the ET configuration, the load of one wheel is applied directly above the edge of the DWPT unit, while in the MT configuration, the center of the dual wheel is positioned above the edge of the DWPT unit. The observed differential strain response can be attributed to the specifics of load distribution across the tire's contact area. When the edge of the tire is placed directly above the DWPT unit, the load is concentrated in the interface between the asphalt and the concrete. This concentration can induce greater deformation, and thus higher strain, due to the focalized application of stress and the difference in load distribution between both materials. On the other hand, when the middle of the dual-axle configuration is placed over point 3, the load from the tire spreads over a wider area above the DWPT unit. This distribution, coupled with the concrete's brittleness, reduces the localized stress and consequently the deformation, leading to lower strain values within the asphalt. This interpretation also aligns with the basic principles of pavement mechanics, which

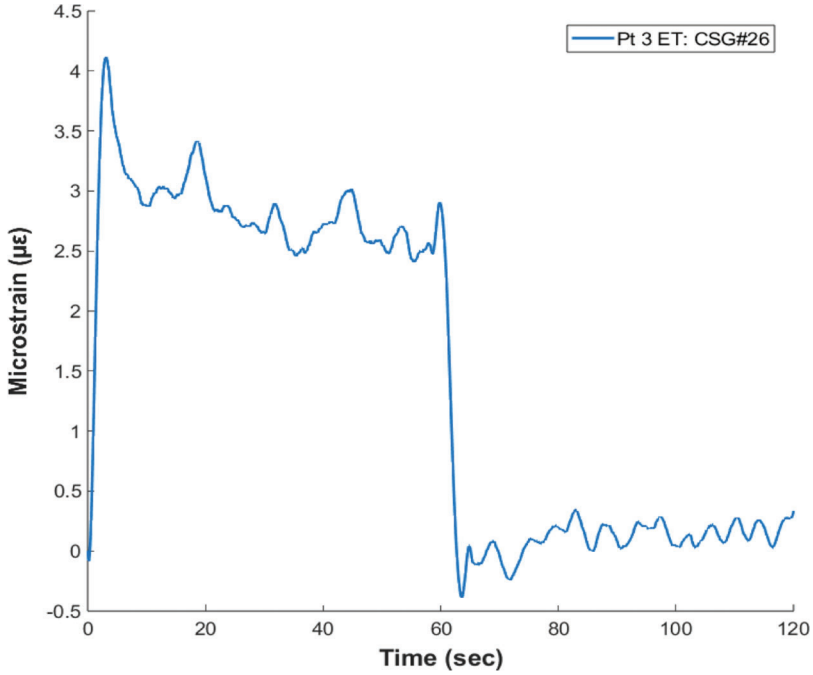

Figure 6.20 Strain development during static load test over location three ET scenario (concrete strain gauge response).

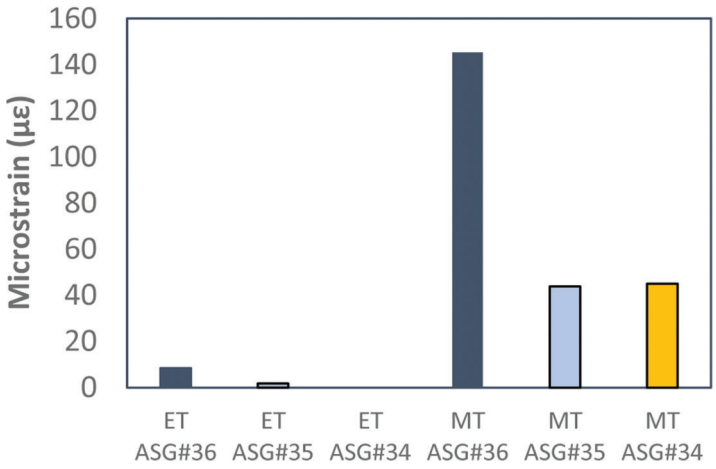

Figure 6.21 Maximum strain reached at 60 seconds of static load at Pt 0 (ET & MT).

dictate that stress (and therefore strain) will be greater in regions where force is applied over smaller areas (Huang, 1993).

6.6 Traffic Test

The traffic test consisted of subjecting the pavement to repeated wheel passes during which the mechanical responses and temperature responses were monitored by collecting data on strain development, stress due to load application, and thermal behavior. The objective of the traffic testing was to assess the pavement's performance under realistic traffic conditions, while simultaneously calibrating the Finite Element Method (FEM) simulation that formed the basis of this study. The dual axle wheel was set to travel at 5 mph and the temperature of the room was maintained between 68°F to 82°F. Testing was conducted under limited environmentally controlled conditions as the building is not thermally insulated. During the duration of the traffic test, the DWPT components were energized by the power supply to mimic the resistive losses of a 230 kW three-phase DWPT. Using an insulated Litz wire setup, the single-turn DWPT coils in rigid pavement is forecasted to have resistive losses of 374.43 W, while the losses for the two-turn DWPT coils in the flexible pavement are predicted at 762.71 W.

As mentioned before, the FEM initial predictions guided the placement of instrumentation and the selection of critical points of interest for the different

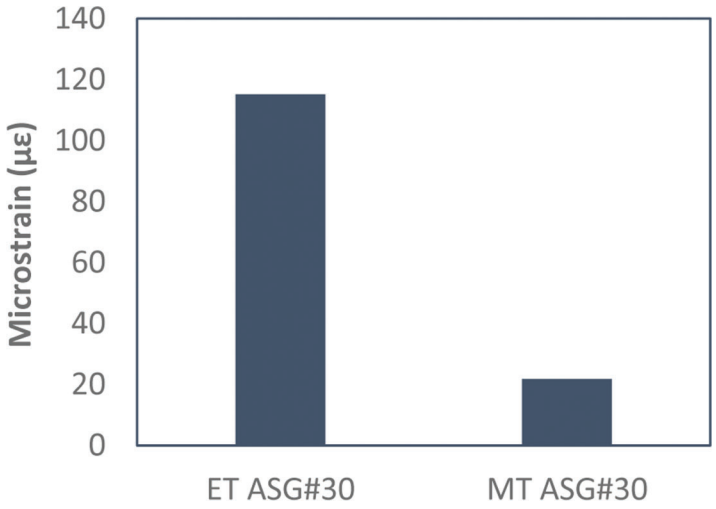

Figure 6.22 Maximum strain reached at 60 seconds of static load at Pt 1 (ET & MT).

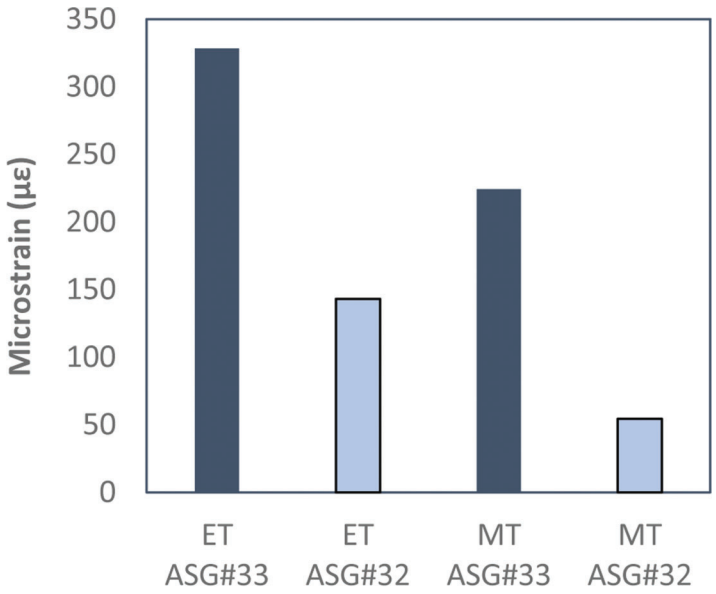

Figure 6.23 Maximum strain reached at 60 seconds of static load at Pt 2 (ET & MT).

test procedures. In this study, the traffic test was set to travel along the edge of the DWPT unit, 3 ft. away from the edge of the pavement section. The dual-axle wheel proceeds from the starting point to the end along the designated path, as illustrated in Figure 6.26. Upon reaching the endpoint, the wheel assembly is elevated, disengaging from the surface, and then it is repositioned back to the starting point to initiate another pass. To assess the extent of rutting from the traffic test on flexible pavement, the surface was scanned in 11 sections along the test area using a laser profile attached to the accelerated pavement testing machine. For the rigid pavement, the laser scanner was not used. The mechanical responses during the traffic test were captured by the embedded sensors during the first 20-wheel passes. After this phase, 960 passes were performed over the pavement, during which the sensors were not activated to manage the extensive data collection required over a period of about 4 hours. In the final stage of testing, the sensors were reactivated for the last 20 passes, culminating in a total of 1,000 passes per day. Only 40 passes were recorded in total by the strain gauges per testing day due to the large amount of storage required for each pass.

The data collected during the traffic application included strain, stress, temperature, and laser profile data. As load mechanism was calibrated on a weekly basis, and a constant pressure of 100 psi was verified throughout each test day, this report focuses only on the strain development, surface profile change in the flexible pavement, and thermal behavior of both pavements. The strain-time history response for the test sections under investigation paralleled the strain responses procedure noted in previous studies by (46–48).

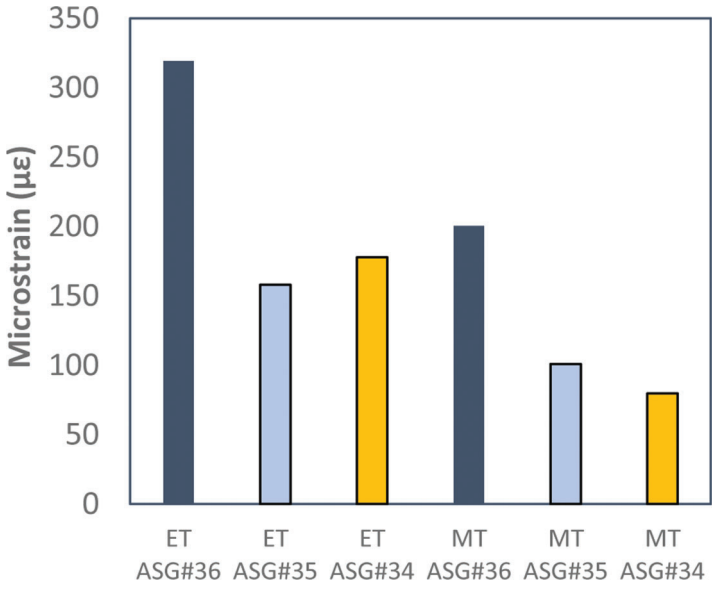

Figure 6.24 Maximum strain reached at 60 seconds of static load at Pt 3 (ET & MT).

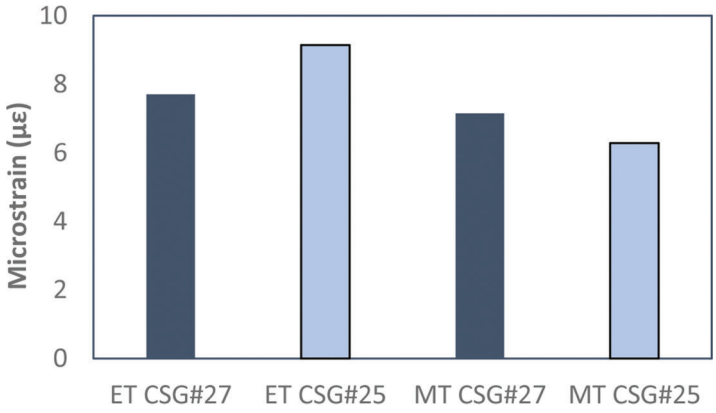

Figure 6.25 Maximum strain reached at 60 seconds of static load at Pt 4 (ET & MT).

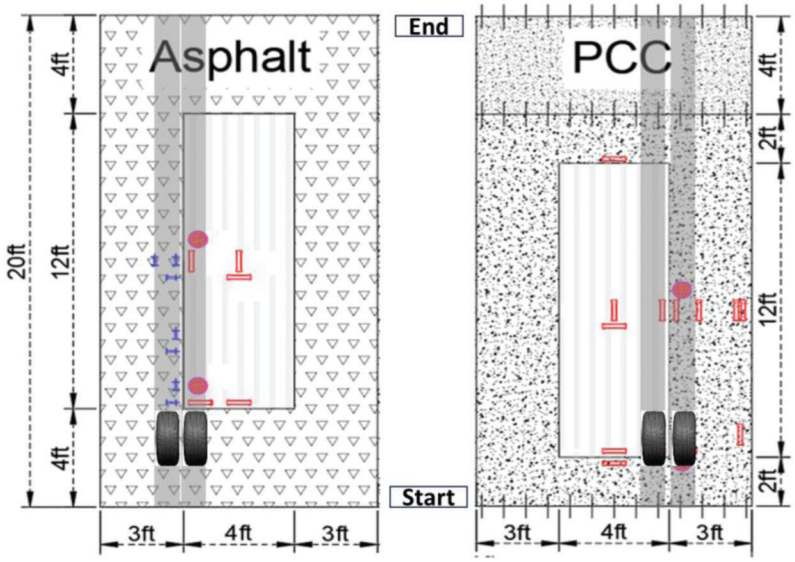

Figure 6.26 Traffic load trajectory.

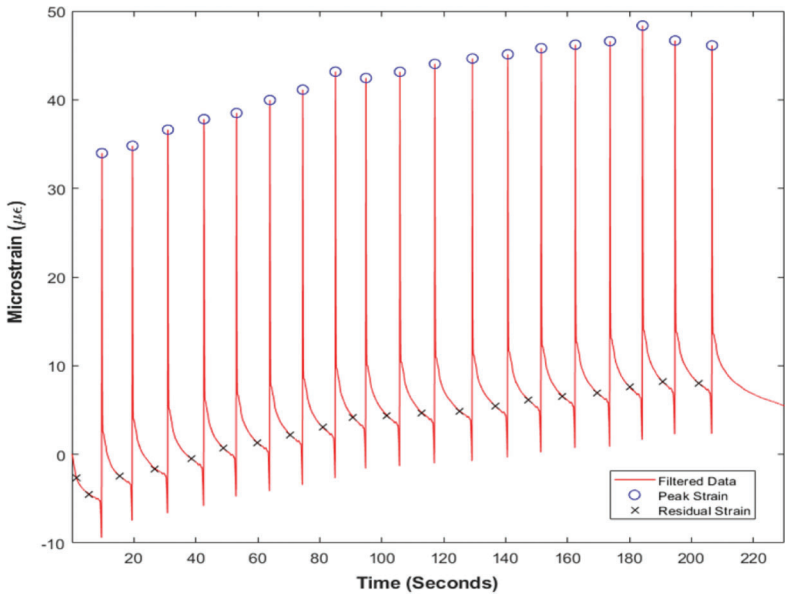

Figure 6.27 Strains measure by one sensor (ASG #36) during traffic.

The signal processing technique employed in this study consisted of the Savitzky-Golay filter, which reduces noise in data analysis and preserves a sharp response using a least-squares smoothing algorithm. The filter's implementation requires setting a frame length, which dictates the number of consecutive data points for each filtering step, and a polynomial order, defining the degree of the polynomial in the least-squares problem. Due to the higher noise levels in the data from the strain gauge sensors embedded in the concrete, a robust Savitzky-Golay filter with a frame length of 10,001 was used to enable clear data visualization while retaining all essential information.

6.6.1 Flexible Pavement

Figure 6.27 illustrate the filtered data for the first set of 20 passes. 20 peaks in tensile strain (positive increase) are depicted in the graph, representing the 20 passes for that specific set of data. The trend of increasing tensile strain observed with successive passes of the wheel over the sensors suggests a response of the pavement's base layer under load. This points to the material's recovery and rebound ability under the pressure and removal of the applied load. When the wheel load is applied to the pavement surface, it induces compressive strain. After the wheel passes, the material's strain response rebounds, resulting in tensile strain. The fact that this phenomenon is evident at the base of the asphalt slab implies that the load's effect is transmitting through the thickness of the pavement structure. The tensile strain denotes the pavement's elastic or resilient response, which allows it to recover and return to its original state after the load is removed. However, the trend of increasing tensile strain with each successive pass indicates an accumulation of permanent deformation, as not all strain is fully recovered. It is a manifestation of the pavement material undergoing both resilient and permanent deformation under repeated loading. The maximum strain experienced at this level is a critical aspect as it represents the limit of the pavement material's elasticity under the applied load before inducing irreversible damage. Notably, such strain tends to appear at the base of the asphalt layer where fatigue cracking, a common distress in flexible pavements, originates.

For each traffic pass, the maximum strain peak was identified by denoting the highest strain experienced per traffic pass. The identification of the residual peak, or the end of the initial compressive strain phase as the load approaches the sensor, relied on locating local maxima and minima procedure applied within the strain-time data. The resilient strain, a measure of the pavement's ability to rebound from the deformation induced by the load, was then calculated by determining the absolute difference between the maximum strain peak and the residual value that preceded it, providing an indicator of the strain recovery capability of the pavement material. A fifth-degree polynomial best-of-fit was applied to both the maximum strain peaks and the residual peaks, graphically illustrating the evolution of these critical points over the course of 25,000 passes, as noted in Figure 6.28.

Upon examining the data from the first and last 20 passes throughout the course of the 25,000 total passes, with an increase in traffic repetitions, both the permanent and maximum strain values increased, indicating progressive damage to the pavement due to repeated loading, as seen in Figure 6.29 and Figure 6.30. Meanwhile, resilient strain, indicative of the pavement's capacity to recover from deformation, demonstrated a downward trend, as expected with the escalating strain demands on the pavement structure, as shown in Figure 6.31. The observed pattern of strain

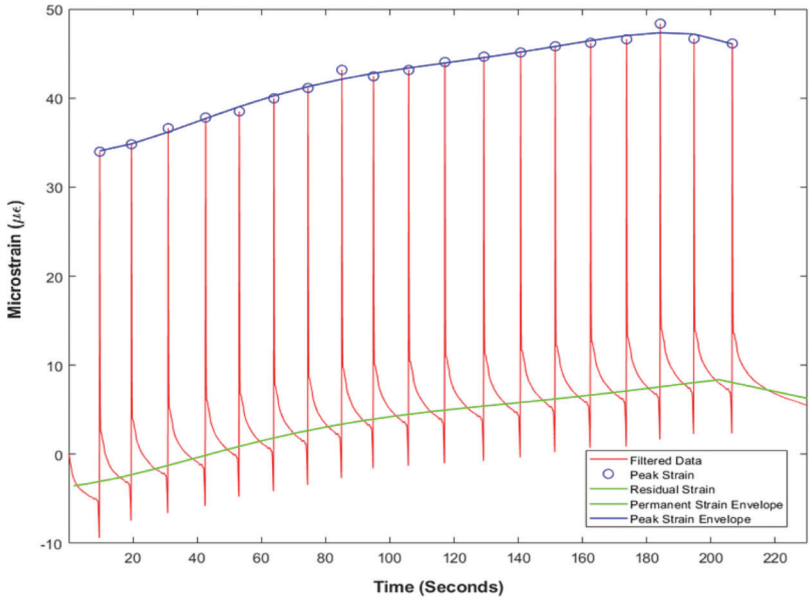

Figure 6.28 Strains measured by one sensor (ASG#36) during traffic (permanent and peak strain envelope).

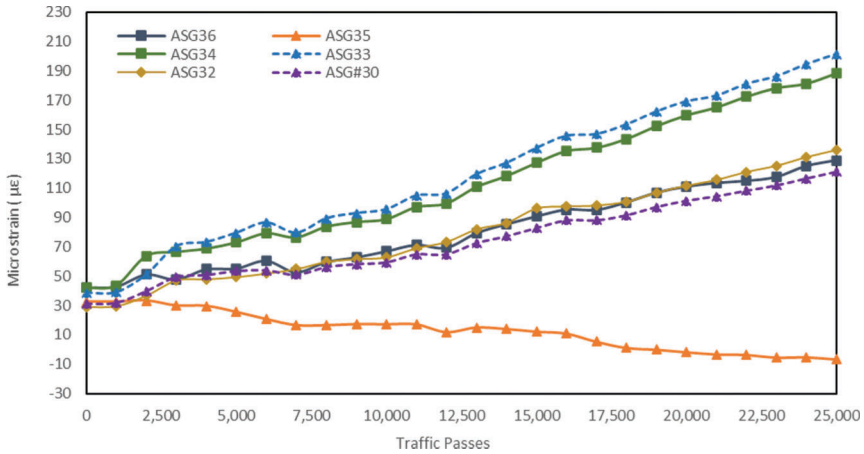

Figure 6.29 Permanent residual (deformation) for all strain sensors (25,000 passes).

behavior aligns with the characteristics outlined in (NCHRP, 2004) regarding the primary stage of the deformation process. The primary stage of the deformation process refers to the initial response of the pavement under loading, which is characterized by relatively higher strains compared to the long-term behavior. It is important to note that the number of traffic passes applied during the static and dynamic load tests, even when subjected to accelerated pavement testing, represents a relatively small quantity compared to the long-term traffic loads that typically cause substantial damage over time.

Permanent deformation or rutting of a pavement surface can be determined using the transverse profile of pavement surface. A laser scanner with a high resolution and accuracy of 0.00590 in. and 0.00630 in. per data point, was used to collect the surface profile data. In this laser profiler system, a motor moves the laser gauge horizontally and the wheel moves the system longitudinally. Once the transverse profile is set, the wheel travels to the desired longitudinal location and the motor drives the laser gauge to scan the requested transverse profile. Figure 6.32 shows the transverse profile when the laser scanner was placed above the middle of the flexible pavement section, 10 ft. away from both of its longitudinal edges, before the application of traffic and after 25,000 passes. A minimal amount of rutting was noted in the rest of testing days and laser profile placement locations. Thus, the center of the flexible pavement was chosen as a sample to denote this behavior. The influence of the dual-axle wheel on the vertical displacement measured by the laser can be observed on the x-axis between 15 to 24 in. and from approximately 28 to 38 in., as shown in Figure 6.32. Although the wheel placement is more evident in the plot after 25,000 passes, there was

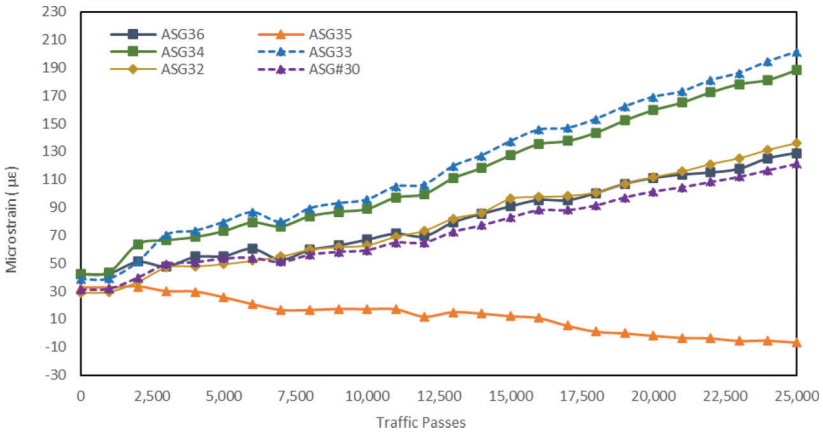

Figure 6.30 Maximum strain for all strain sensors (25,000 passes).

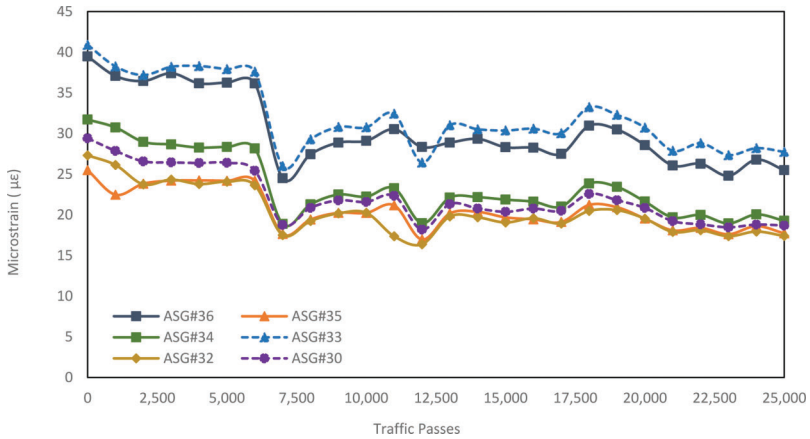

Figure 6.31 Resilient strain for all strain sensors (25,000 passes).

not a significant increase in rutting after 25,000 passes. The lowest vertical measurement for the laser measurements before traffic was approximately 9.68 in., while for the measurement after 25,000 passes was approximately 9.65 in., representing a decrease of approximately 0.3%.

6.6.2 Rigid Pavement

With only one exception, all the asphalt strain gauges exhibited a peak tensile strain behavior. On the other hand, the behavior of the concrete strain gauges varied based on their specific locations and placements. Thus, the algorithm was modified to accurately identify and locate the peak strains as the dual-axle wheel travels above the sensor, whether they occurred in compressive (downward peak) or tensile manner (upward peak). Just like with the asphalt sensors data analysis, a fifth-degree polynomial best-of-fit was employed to capture both the maximum strain peaks and the residual peaks evolution. This graphical representation demonstrates the behavior of these values throughout the 25,000 passes, as illustrated by a sensor denoting compressive peak behavior in Figure 6.33, and by a sensor denoting tensile peak behavior in Figure 6.34. The permanent strain envelope graphically represents the permanent deformation, while the peak strain envelope visually depicts the evolution of peak strains over 25,000 passes.

6.7 Thermal Behavior

During each traffic test day, encompassing 1,000 traffic daily passes, the DWPT coils were energized, enabling the constant transfer of current to the coils. Once the test was completed, the power supply was turned off. The typical duration for a traffic test was approximately 4 hours. The thermal data gathered during this period, across various test days, offers insight into the temperature distribution within the pavement when subjected to both traffic loading and the power transfer mechanism.

6.7.1 Flexible Pavement

The thermal results displayed a temperature rise associated with the energy transfer to the DWPT coils upon the power supply's activation. The temperature

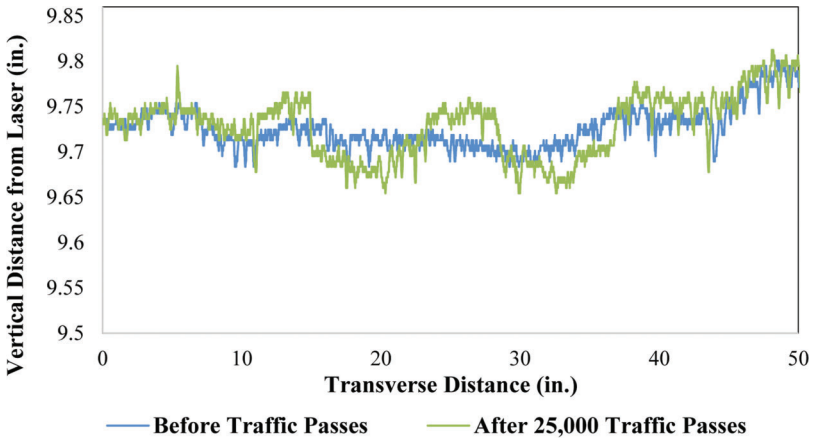

Figure 6.32 Transverse profile before and after 25,000 passes when the laser was placed in the middle of the flexible pavement (10 ft. away from longitudinal edges).

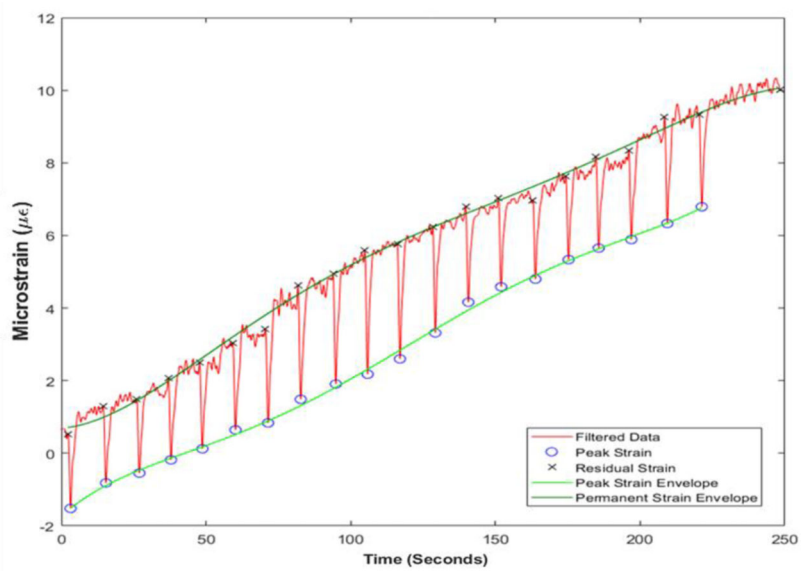

Figure 6.33 Strains measured by one sensor (CSG #5) during traffic denoting compressive behavior (permanent and peak strain envelope).

increase varied based on the depth at which each thermocouple was placed, with the highest average increase being approximately 12°F. Furthermore, the two-winding coil configuration in the flexible pavement contributes to more pronounced resistive losses and a higher temperature increase.

Figure 6.35 portrays the thermal behavior on 25th test day upon the completion of 25,000 passes. It's important to note that the initial temperature for each test was influenced by the ambient temperature of the APT facility. The APT facility was designed to control temperature, however, due to its lack of thermal insulation, the facility's temperature is slightly influenced by the environmental temperature, leading to minimal fluctuations in ambient temperature. The minimal fluctuations in ambient temperature observed could be further affected by the cycling of the cooling unit in the room. Throughout the duration of the flexible pavement traffic test, conducted between July and October of 2022, the facility's temperature was maintained within a range of 68°F to 83°F.

Thermocouples TC 14, TC 15, and TC 13, positioned at a depth of 3 in. from the surface, recorded the highest values. Among these, TC 13 and TC 15 displayed the most elevated temperatures, with TC 13 positioned centrally within the DWPT unit and TC 15 located at the lower edge of the DWPT unit. As the depth from the surface increased, the recorded temperature values correspondingly decreased. The lowest temperature reading was displayed by TC 4, located at a depth of 9 in. Higher temperatures are observed closer to the surface, a trend which is typical in pavement layers due to direct exposure to environmental factors and surface heating. This trend could also imply that these surface layers are influenced by the waste heat generated by the energy transfer mechanism of the DWPT system. Conversely,

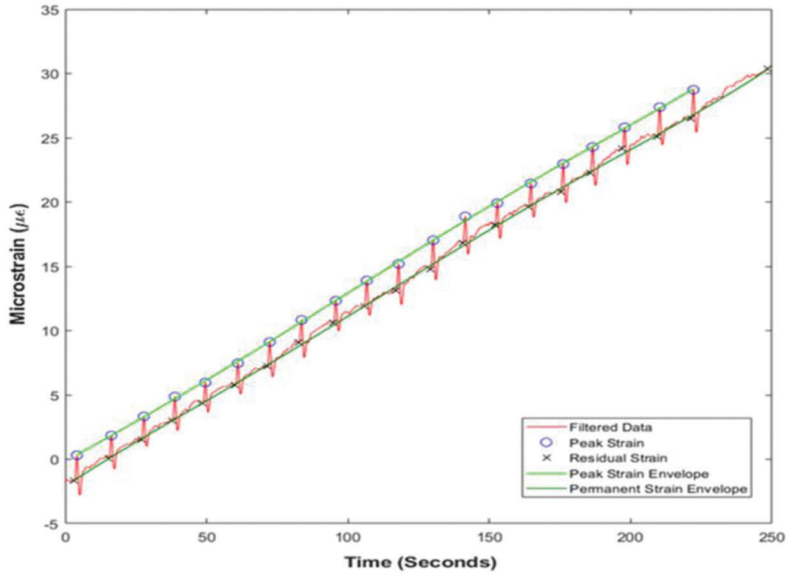

Figure 6.34 Strain measured by one sensor (CSG#13) during traffic denoting tensile strain behavior (permanent and peak strain envelope).

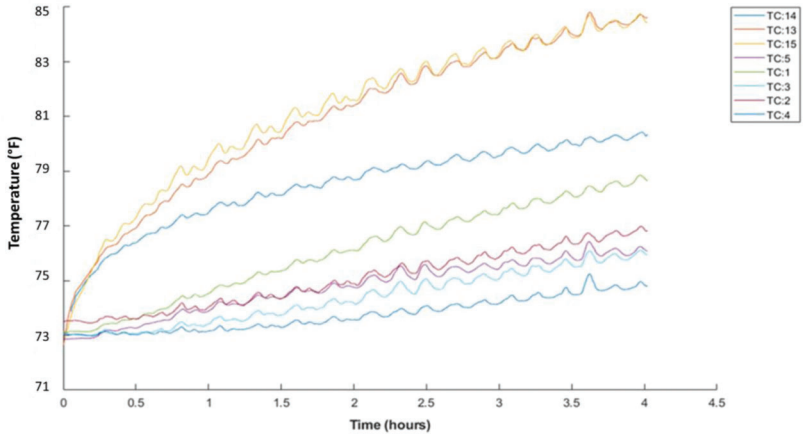

Figure 6.35 Thermal behavior of flexible pavement during test day 25 (25,000 passes).

lower temperatures at greater depths may reflect the insulating properties of the upper layers. Yet, while temperature increases were observed in correlation with the activation of the power supply, these changes were not markedly high, maintaining the overall thermal stability of the pavement.

6.7.2 Rigid Pavement

The thermal results show a trend similar to the thermal results from the flexible pavement section, denoting a temperature increase in relation to the activation of the power supply and subsequent energy transfer to the coils. The highest temperature increase was approximately 7°F Figure 6.36 displays the thermal behavior on the final test day upon completing 25,000 passes. Like in the flexible pavement traffic test, the initial temperature for each test was influenced by the control room's temperature. The rigid section testing took place between September and November 2022 and the facility temperature for the start of each test day was kept within a range of 61°F to 81°F.

The thermal results from the rigid pavement showed a correlation between thermocouple depth and thermal response. Thermocouples TC 18, TC 17, and TC 16, all located 3 in. beneath the surface, registered the highest temperature increase. In particular, TC 16, which is positioned on the upper section of the DWPT unit, near the joint, recorded an increase in temperature from 77°F to approximately 84°F. Thermocouples TC 18, TC 9, and TC 17, showed an increase from 77°F to approximately 80°F. Notably, TC 16 consistently marked a higher increase than other thermocouples throughout the entirety of the testing period.

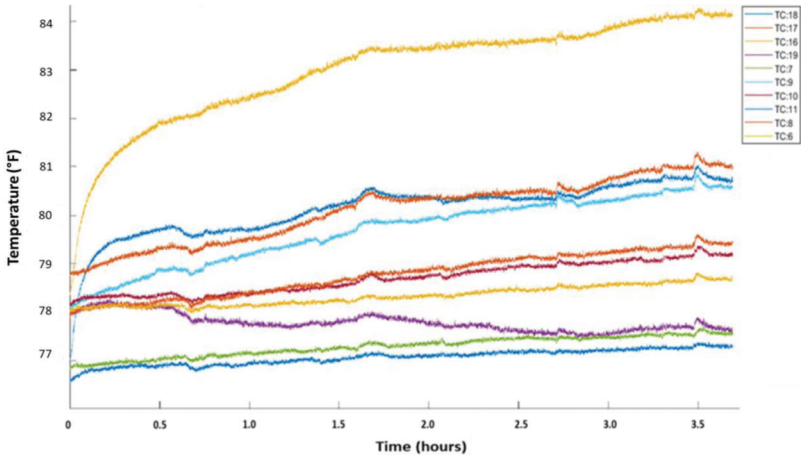

Figure 6.36 Thermal behavior of rigid pavement during test day 25 (25,000 passes).

Moreover, for thermocouples positioned 5 in. or deeper below the surface, the temperature increase was less pronounced. Ultimately, the temperature increase in the rigid pavement section was generally lower than in the flexible section, attributable to the inherent thermal properties and behavior of rigid materials, along with the fact that the flexible pavement's two-winding coil configuration generates higher resistive losses.

7. DISCUSSION

7.1 Electrical System

The team developed a three-phase planar DWPT topology that is relatively straightforward to implement in practice. A convenience of the design is that a roadway with the proposed design can deliver power to a wide range of vehicles. Specifically, power is scaled by the length of the receiver. The design approach has been validated through hardware experiment and has been used to generate specifications for the Indiana DWPT pilot testbed that will be installed on a quarter mile segment of US 231 in West Lafayette in 2024. It is recognized there are some electromagnetic advantages to using magnetic material within the roadway. Indeed, many stationary wireless charging systems employ ferrite sheets. In this effort, we considered magnetized concrete. In the end, the team found that at this point in time the potential benefits do not warrant the additional complications and cost of applying such materials. As a result, the design that we are pursuing further utilizes only conductive material (coils), judiciously placed, within the roadway. To facilitate relatively straightforward installation of the coils within a roadway, the team has developed an L-bracket strategy, shown in Figure 7.1. There, one can observe that the coil placement is kept using holes in the respective rungs. Tension is achieved through the rails, which also are used to maintain end-turn locations. We envision that this approach enables transmitters to be constructed off-site, simplifying the roadway construction process.

It is noted that safety is an important aspect of the design. In operation, no transmitter coil is energized unless a receiving coil is above it. In addition, part of the design process is to create transmitter/receiver geometries that limit human exposure to the fields generated to values below internationally accepted exposure limits.

Finally, it is recognized that DWPT system brings significant additional cost to a roadway. One of the most significant costs are the power electronics (inverters) and the vaults to house the electronics. In the pilot development, the team specified using an inverter per coil to minimize risk. Future advances are focusing on leveraging a single inverter to provide power to multiple coils.

7.2 Mechanical Behavior of Pavement

After 25,000 passes, only the rigid pavement section displayed notable damage from both test sections. A mid-panel crack originated in the center of the main slab, approximately 8 ft. away from the joint and 8 ft. away from the lower transverse edge, depicted by the red line drawn over the concrete, as shown in Figure 7.2. The blue lines denote the transverse edges of the DWPT unit, while the orange lines display the components near the locations of the cores retrieved for pull-off testing. The mid-panel crack fully penetrated the Class A concrete surrounding the DWPT unit but did not fully extend into the underlying magnetizable concrete, as of 25,000 passes. Several factors contributed to the formation of this mid-panel crack. These include construction issues, lack of adhesion between the Class A and magnetizable concrete interface, difference in material properties, uneven distribution of load, and nonuniform stress-strain patterns. It is important to acknowledge, before delving into further discussion, that the design of both pavement sections was constrained by the APT

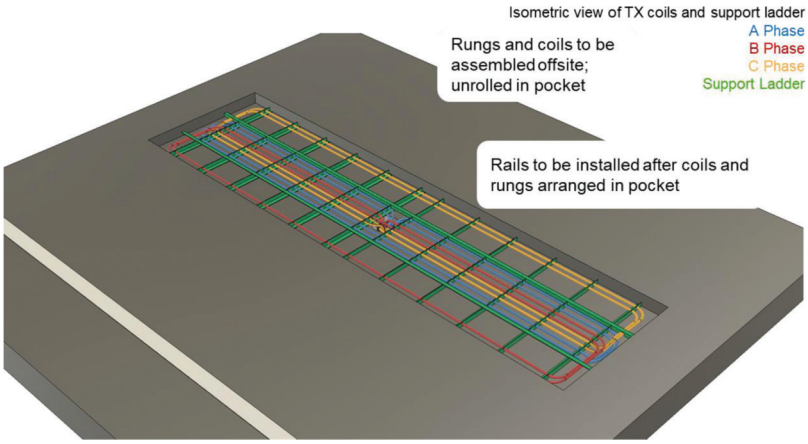

Figure 7.1 Transmitter coil installation approach.

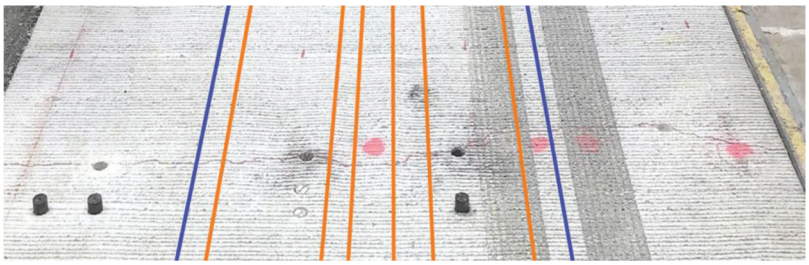

Figure 7.2 Mid-panel crack over rigid pavement (note: picture was taken after cores were retrieved for pull-off testing) (INDOT).

facility's pit area and the incorporation of the DWPT unit embedment. Additionally, as one of the first empirical attempts in the United States to introduce DWPT components into the pavement, this study highlights the need for further research and construction experience to address and optimize these challenges effectively.

The incorporation of magnetizable concrete used in a cast-in-place scenario for the first time introduced an additional challenge to the rigid pavement construction. The mixing and placement process, handled by a third party rather than the manufacturer, might have introduced potential discrepancies in material handling and consistency. Differences in mixing proportions, water content, or handling techniques could have impacted the concrete's strength, durability, and overall performance throughout its design life. Moreover, the construction process involved a time gap of 1 week between the pouring and hardening of the DWPT unit and the adjacent Class A concrete slab. This time gap influenced the adhesion strength between the two concrete interfaces. Differential curing and shrinkage between the slabs during this period could have also resulted in varying degrees of stress at the joint interface. As the adhesion between the slabs was not sufficient, it resulted in a compromised area prone to cracking and its subsequent propagation.

Extra caution was taken by the construction workers during the pouring process to avoid any disruption to the instrumentation or the embedded components. However, the manual consolidation performed by the workers could have affected the uniformity and

Figure 7.3 Pull-off adhesion tester (INDOT).

consolidation of the concrete. Inadequate consolidation can result in voids, air pockets, or segregation within the concrete, which may lead to reduced structural integrity and increase the likelihood of cracks appearing under repeated traffic loads. Considering the potential discrepancies in the handling and consistency of the magnetizable concrete, the 1-week interval between pouring the DWPT unit and the adjacent Class A concrete slab, and the manual consolidation process, these factors collectively contributed to the formation of cracks in the rigid pavement section. The combined effect of these factors can result in localized stress concentrations, reduced adhesion between the slabs, and compromised structural integrity, ultimately increasing the vulnerability of the pavement to cracks.

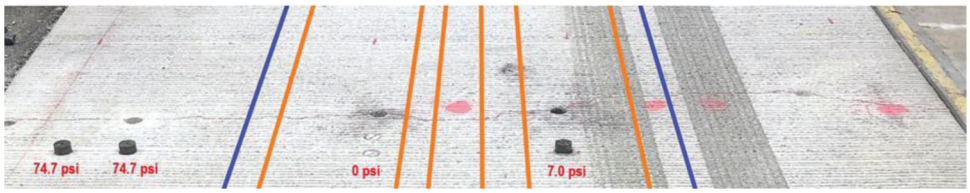

Figure 7.4 Tensile strength results from pull-off test (INDOT).

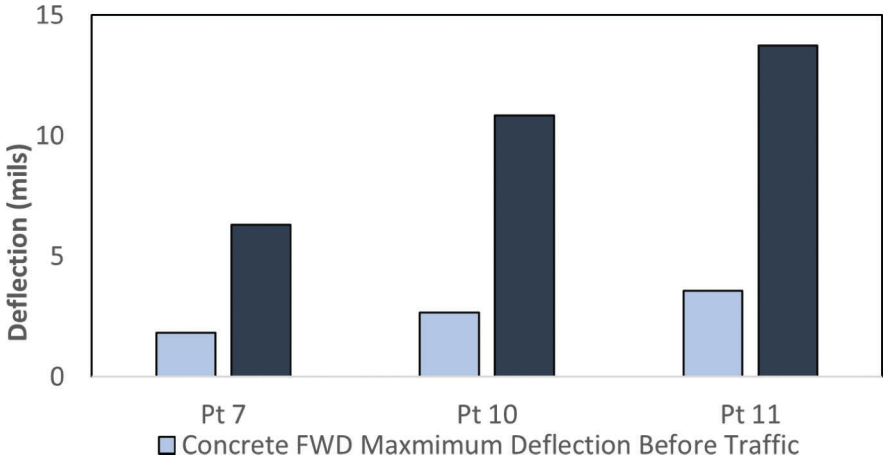

Figure 7.5 FWD deflections before and after 25,000 passes (points 7, 10, and 11).

The pull-off test, as outlined in (ASTM, 2022c), is a method used to evaluate the bond strength or adhesion between concrete interfaces. In this test, a portable adhesion tester, shown in Figure 7.3, is used to apply a tensile force to a small disc-shaped sample that is bonded to the concrete surface. The force is gradually increased until the sample detaches from the concrete, and the maximum force required for detachment is measured. Several cores were taken across the crack region concrete to perform the pull-off test. The locations and results from each core are shown in Figure 7.4. The blue lines represent the transverse edges of the DWPT unit, while the orange lines depict the components near the core area. Two of these cores were obtained from Class A concrete and exhibited a tensile breaking point of approximately 74.7 psi, indicating a relatively higher bond or adhesion in that material. On the other hand, only one core retrieved above the DWPT unit region remained intact during the drilling procedure, reflecting a tensile breaking point of approximately 7 psi. The rest of cores from the DWPT unit region didn't withstand the drilling process and detached from the concrete immediately as the drilling procedure took place. Both values, including the 74.7 psi respecting to Class A concrete, are substantially lower than the expected low standard value of approximately 180 psi, based on INDOT's previous pull-off test experience.

As mentioned in Section 6.5.2, the FWD data provided an insight into the deflection behavior of the rigid pavement before and after the crack. Figure 7.5 displays the results before and after traffic for the three points under the crack region: point 7 (center of DWPT unit), point 10, (Edge of DWPT unit), and point 11 (Class A concrete). The results highlight a pronounced increase in deflection values after traffic, typically indicative of reduced structural integrity, associated with the presence of the crack. In pavements with structural soundness, the applied load is evenly distributed over a wide area, minimizing the immediate impact on specific points. However, the elevated deflection values noted at points 7, 10, and 11 imply that this distribution mechanism may be compromised in the vicinity of the crack. Instead of efficiently spreading the load, the increased deflections observed suggest that the pavement's ability to distribute the applied traffic load has been compromised, likely due to the impaired structural integrity in the vicinity of the crack. This trend is not commonly expected in the absence of structural issues, indicating that the mid-panel crack potentially plays an influential role in altering the load-spreading capability of the concrete. point 7, located over the region of the DWPT unit where the crack has not yet fully penetrated, experienced lower deflections compared to point 10 and point 11. At point 10, located beside the edge of the DWPT unit, the deflections reflected the combined effects of the DWPT unit and the adjacent concrete Class A, resulting in higher deflections. Point 11, located within the Class A concrete section, showed the highest deflections among the three points. These observations align with the presence of a full-depth crack within the Class A concrete as it contributed to the increased deflection response.

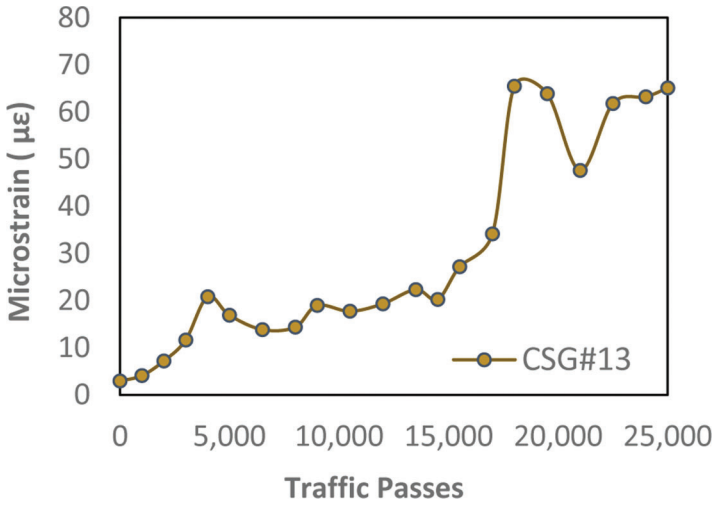

Figure 7.6 Maximum peak strain CSG#13 after 25,000 passes.

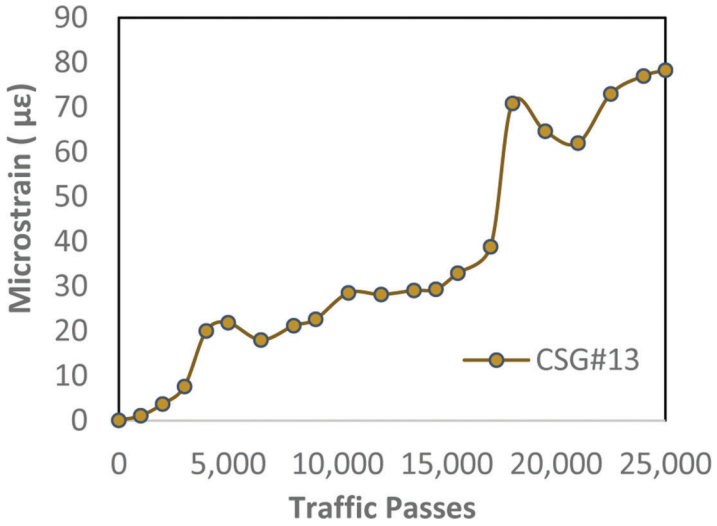

Figure 7.7 Permanent strain evolution for CSG#13 after 25,000 passes.

It is important to note that visual surveys of the pavement were conducted daily throughout the testing process, providing a reliable timeline of physical changes on the surface in conjunction with the sensor data. The crack was visually observed for the first time between the 18th and 19th days of testing (18,000 and 19,000 passes, respectively). CSG#13 and CSG#14, both longitudinal sensors under the region of the crack, are considered for the following analysis. Figure 7.6 and Figure 7.7 illustrate the evolution of maximum peak strain and permanent peak strain for the longitudinal sensor CSG#13, respectively. Figure 7.8 and Figure 7.9 illustrate the evolution of maximum peak strain and permanent peak strain for the longitudinal sensor CSG#14, respectively. The permanent and maximum strain development for both sensors denotes a consistent upward increase as passes increase. Corresponding with the initial visual indications of the mid-panel crack, a significant increase in permanent and maximum strain was measured by both sensors between 17,000 and 19,000 passes. Nonetheless, it is noteworthy that the strain responses in CSG#14 are higher compared to those in CSG#13. This difference can be attributed to the placement of CSG#14 next to the edge of the DWPT unit within the Class A concrete, whereas CSG#13 is located beside the edge of the DWPT unit but within the magnetizable concrete. Consistent with the results obtained from the Falling Weight Deflectometer (FWD), where deflections in Class A concrete are higher than those in magnetizable concrete, the strain results over the Class A concrete exhibited higher responses. This finding supports the presence of a full-depth crack over the Class A concrete but only a partial presence over the magnetizable concrete. Interestingly, the formation of the mid-panel crack happened relatively early in the lifespan of the pavement, before reaching 25,000 passes. In a broader context, 25,000 passes represent a relatively

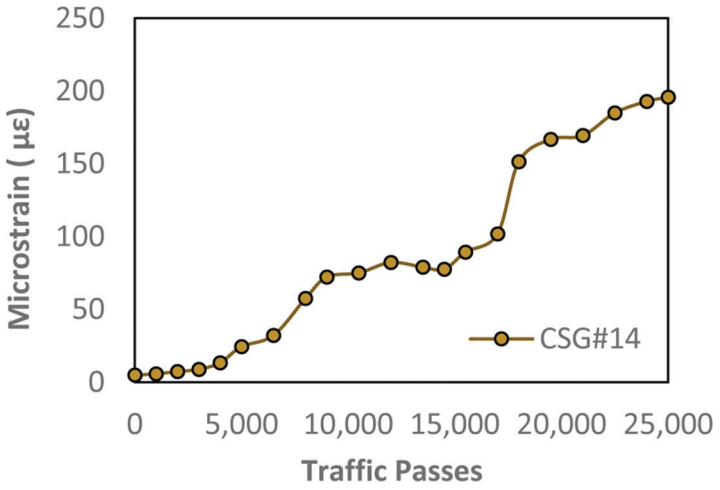

Figure 7.8 Maximum peak strain CSG#14 after 25,000 passes.

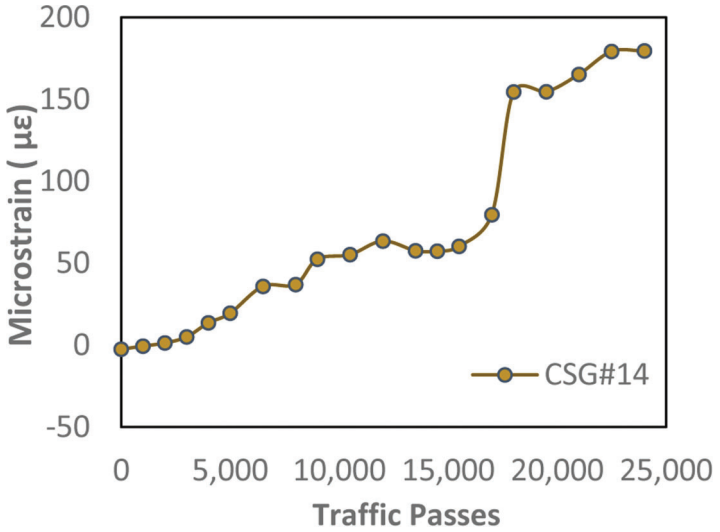

Figure 7.9 Permanent strain evolution for CSG#14 after 25,000 passes.

early stage for a pavement structure under normal traffic loads. Nevertheless, it should be considered that this data represents an accelerated testing scenario, where the pavement is subjected to an increased frequency of load repetitions compared to normal traffic conditions.

7.3 Thermal Behavior of Pavement

The thermal testing conducted at the APT facility reveals a discernible increase in pavement temperature upon energization. Nevertheless, this elevation seems to reach a point of stability over time across all thermocouples. This observation suggests that the pavement and coils effectively dissipate heat into the surrounding environment, ensuring sustained operation. The maximum temperature rise during the energization period was approximately 7°F for the rigid test section and 12°F for the flexible one.

It is worth noting that minor fluctuations in ground temperature at the facility, influenced by the natural temperatures of the day influencing surrounding ground temperatures, contribute to minor variations in thermal rise. Despite facility temperature control, these daily fluctuations impact the ground temperatures immediately outside the facility, which may somewhat influence ground temperatures within the facility as well. That said, a more in-depth investigation is imperative to comprehensively comprehend the thermal performance of the pavement in a real-world context outside of a temperature-controlled facility. This exploration should ideally take place in an environment that mimics the full spectrum of temperature and sunlight variations experienced throughout the day. Such a study is crucial to assess the technology's viability in real-world scenarios where it might be implemented.

8. PILOT PROJECT IMPLEMENTATION

Over the past 3 years, Purdue University, with support from the National Science Foundation (NSF) ASPIRE Engineering Research Center and INDOT, has pursued the development of DWPT systems that provide the power necessary to move fully loaded trucks at highway speeds. A significant result of the research is a practicable DWPT design that is relatively straightforward to construct and implement, not only for heavy-duty vehicles, but across all vehicle classes. The economic viability of DWPT systems for Indiana roadways has also been assessed and the team has found that implementing the DWPT system is attractive to both potential electrified roadway (ER) investors, who expect to see strong returns on investment over a 20 to 30-year timespan, and truck fleet owners/operators, who must select between electric and traditional vehicles (Haddad et al., 2022). Indeed, it is likely that the IN-based results on DWPT techno-economic feasibility would translate to roadways nationwide.

The DWPT design was validated at the APT facility and Purdue University's Vehicle Systems Laboratory (VSL). The validation included structural, thermal, and electromagnetic testing of the respective components to confirm that their performance matched expectations. DWPT coils were placed in both rigid and flexible pavements in the APT facility. The rigid pavement DWPT unit contains a ferrite/concrete mixture, while the flexible pavement unit does not, this latter unit being referred to as a coreless design. Both pavements have thus far sustained 25,000 passes of the 9,000 lbs accelerated pavement testing loading.

Purdue University developed plans to establish a Dynamic Wireless Power Transfer Testbed (DWPTT) along ¼-mile of an existing Indiana roadway. This testbed will serve as a critical platform for the transition of DWPT technology from small-scale pavement sections to a practical roadway environment. Through evaluation, testing, and data collection in this real-world setting, an enhanced understanding of the interactions between the DWPT system and the pavement structure will be achieved, contributing to the advancement of the technology, and enabling future large-scale implementation. The proposed roadway is shown in Figure 8.1. An electrical diagram that illustrates the component interconnections is shown in Figure 8.2. As shown, the DWPTT will consist of a continuous array of eighty-five 3-phase 12 ft. transmitter coils that are placed consecutively within the roadway at a depth of approximately 2 in. beneath the surface. Adjacent to the transmitter coils, placed in the asphalt shoulder and the fore slope adjacent to the shoulder, are 43 vaults containing the power electronics and compensation circuit components that are used to form the high-frequency AC voltages to the transmitter coils. All electrical boxes are intended to be within buried vaults that enable access for periodic maintenance and component upgrades.

The establishment of the pilot DWPT road section encompasses two key objectives. Firstly, it aims to develop and optimize efficient installation methods for the transmitter coils within a practical roadway context, with a particular focus on the milling-based installation approach employed in this project. Successful implementation of this approach has the potential to reduce DWPT installation costs and enhance acceptance within the electric vehicle community. Secondly, the pilot project will provide a comprehensive testing and validation platform for the transmitters and associated electronics under realistic conditions, allowing for the evaluation of the reliability, aging, and performance of the materials and system. Furthermore, the insights and data obtained from the testbed will be shared with industry members, including pavement, roadway, and vehicle manufacturers, facilitating their attempts to enhance and expand DWPT incorporation into pavements. In the initial phase of

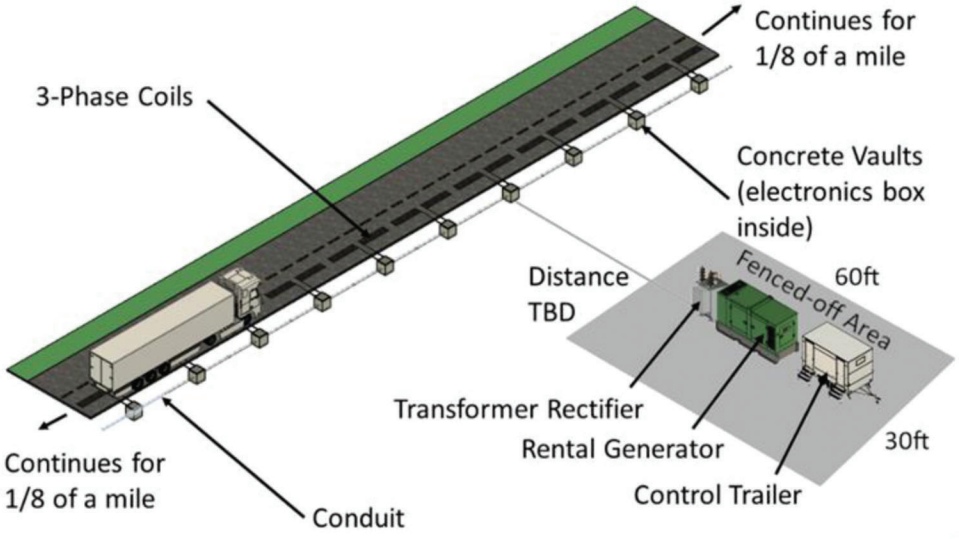

Figure 8.1 Proposed dynamic wireless power transfer testbed (DWPTT).

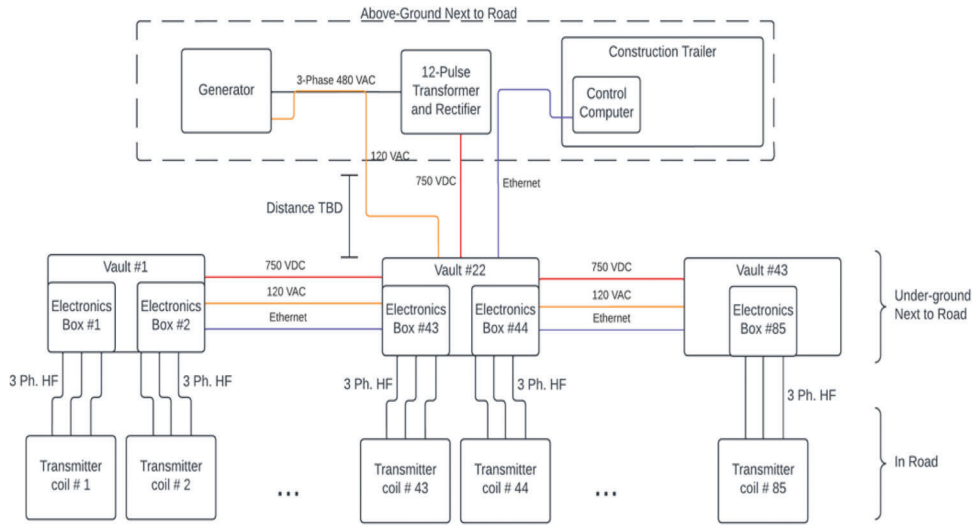

Figure 8.2 Electrical interconnection of DWPTT components.

DWPTT development, the plan is to power the electronics boxes with a 250-kVA portable generator, housed on a wheeled trailer for easy movement and placement. Contractors are expected to position the generator at a safe distance from the roadway, at a location agreed upon with INDOT. Nearby, a transformer/passive rectifier assembly will convert the 480V (AC) output from the generator to about 750V (DC). This will necessitate laying DC cable within buried conduit, extending from the rectifier's output to the electronics boxes at the road shoulder. Additionally, 120 VAC cable will need to run from the generator to these electronics boxes.

9. SUMMARY OF FINDINGS AND CONCLUSIONS

The objectives of this project were to (1) design and evaluate a transmitter-receiver topology for DWPT, (2) develop a better understanding of the interaction between the pavement and the embedded DWPT, and (3) support the design and installation of a 230-kW DWPT system pilot for HDEVs on an existing INDOT roadway. In view of the above, a simultaneous three-phase approach was coordinated to address the project objectives. Through detailed documentation, comprehensive investigation, and thorough evaluation, this project contributes to the ongoing research aimed at integrating DWPT components into pavement structures, thereby taking steps toward narrowing the knowledge gap related to the practical integration of embedded DWPT components into pavements and its impact on the mechanical and thermal performance of the structure.

Phase 1 focused on the laboratory testing of pavement materials and DWPT systems, aimed at developing an economically efficient power system architecture. This included the construction of inverters, compensation circuits, and rectifiers at Purdue University's Grainger Energy Conversion and Microgrid Laboratory (GECML). The team designed a three-phase transmitter-receiver topology for dynamic wireless power transfer. This configuration boasts a peak power output of 200 kW, catering to the requirements of standard Class-8 semi-tractor trailer trucks. The magnetizable-core transmitter is designed with a single turn, while the coreless transmitter incorporates two turns. This is done to maintain a comparable per-length mutual inductance for both configurations. Performance estimates indicate that the magnetized-based design demonstrates a smaller compensation circuit mass and volume as well as a slight increase in system efficiency. It was also observed that both designs have similar behavior within $\pm 20\%$ alignment. However, the magnetized-core design demonstrated more pronounced power reduction and sensitivity to misalignment beyond this range.

Phase 2 of this project focused on the embedment of DWPT components into two small-scale pavement test sections at the APT facility of INDOT in West Lafayette, Indiana. The test sections consisted of a flexible pavement and a rigid pavement, each incorporating a DWPT unit composed of Class C and magnetizable concrete, respectively. The construction of the flexible pavement section required milling down the surface course from the previous INDOT project and excavating the DWPT unit's cross-section. Conversely, for the rigid pavement section, the entirety of the previous flexible pavement was removed, leaving only the pit's subgrade consisting of A-6 soil. Embedding DWPT components introduced challenges in the conventional construction processes due to the altered geometric composition of the pavement. While manual techniques were employed for this small-scale project, such methods may prove unfeasible for large-scale implementation. Additionally, the different materials used for the DWPT unit, and the surrounding slab introduced variations in the load distribution within the pavement, potentially influencing the mechanical

behavior of the structure. The handling and transportation of the magnetizable concrete by the paving contractor rather than the manufacturer, coupled with its first-time use in an in-cast application, introduced complexity and heightened the possibility that any mixing or handling variances could impact its long-term performance.

The sensor instrumentation placement and critical locations for testing operations were based on the results from FEM, a product of research collaboration between Purdue University and the University of Texas, El Paso. The models predicted stress and strain distributions due to the application of static loads. Additionally, the models indicated that the tire's alignment, either mid-tire or edge, when positioned at the center or the edge of the DWPT unit, influenced load distribution and the mechanical interaction between the interfaces.

This report documented the mechanical and thermal assessment of both pavement sections before and after 25,000 passes. The testing procedures conducted in Phase 2 were divided into two main categories: pre-traffic evaluations and traffic tests. FWD was used to evaluate the stiffness of the pavement layers prior to the application of static or dynamic loads. The results of the FWD test on the flexible pavement presented atypical patterns. A decrease in deflections was observed after traffic, attributed to factors such as potential secondary compaction from traffic and the possible stiffening of the asphalt due to waste heat generated by the DWPT mechanism. The FWD test results from the rigid pavement were correlated with the formation of a mid-panel crack, evidenced by an FWD deflection increase observed after traffic, with this effect being more pronounced at the test points directly beneath the crack. The static load test was conducted to evaluate the strain distribution at the base of the flexible pavement before applying accelerated pavement testing traffic loads. Differences in strain distribution were noted in the flexible pavement at the interface between the embedded DWPT unit's Class C concrete and the surrounding full-depth asphalt, with higher strains occurring at the edge of the DWPT unit, within the asphalt, compared to the full-depth asphalt area. In line with the predictions of the FEM models, the alignment of the dual-axle wheel, whether centered or at the tire's edge, influenced load distribution. Strains were more pronounced when the dual-axle wheel was positioned at the edge, compared to mid-tire placement.

After 25,000 passes, only the rigid pavement section displayed notable damage, out of both test sections. A mid-panel crack originated in the center of the main slab, approximately 8 ft. away from the joint and 8 ft. away from the lower transverse edge. The mid-panel crack fully penetrated the Class A concrete surrounding the DWPT unit but did not fully extend into the underlying magnetizable concrete. Several factors contributed to the formation of this mid-panel crack. These include construction issues, inadequate bonding at the interfaces of the Class A and magnetizable concrete, segregation in the concrete mixes due to insufficient consolidation, different material properties between the interfaces, and uneven distribution of load.

The thermal results indicated an increase in temperature linked to the activation of the DWPT system's power supply. This temperature increase varied according to the depth at which each thermocouple was placed, with a maximum increase observed approximately reaching 12°F in the flexible pavement section and approximately 7°F in the rigid pavement section. Furthermore, the use of a two-winding coil configuration in the flexible pavement led to more noticeable resistive losses, resulting in a greater temperature escalation.

In Phase 3 of this project, Purdue University developed plans to establish a Dynamic Wireless Power Transfer Testbed (DWPTT) along a ¼-mile roadway in West Lafayette, IN. This testbed will serve as a critical platform for the transition of DWPT technology from small-scale pavement sections to a practical roadway environment.

9.1 Future Research Directions

The complexity of incorporating DWPT components into pavements, as documented in this report, highlights the multifaceted and challenging nature of embedding this technology into pavement structures. Careful design considerations, stringent construction procedures, and a thorough understanding of how the presence of a DWPT unit influences pavement behavior, are crucial to ensure the long-term durability, serviceability, and integrity of a pavement with embedded DWPT components. Moving forward, large-scale implementation of DWPT technologies into pavement structures will rely on continual and comprehensive research. Efforts should focus on refining design considerations, optimizing embedment procedures, and understanding the long-term impacts of DWPT components on pavement structures. Such diligence is crucial to ensure the reliability and longevity of this technology within the broader infrastructure context.

Further research should also investigate the development of standardized, scalable, and cost-effective construction methodologies for embedding DWPT into real-world pavement structures, considering factors like optimal embedding depth and load-bearing capabilities. Such research must encompass strategies for maintaining, rehabilitating, and conserving pavements with embedded DWPT components to ensure longevity and performance. Establishing procedural guidelines for construction workers, developing training modules, and creating best-practice manuals are essential, as these measures are crucial in creating a safe working environment, particularly when dealing with the complexities of integrating DWPT components into pavement structures. Additionally, a comprehensive cost-benefit analysis that incorporates both construction and maintenance procedures is essential.

REFERENCES

AASHTO. (n.d.). *AASHTO T 269: Standard test method for percent air voids in compacted dense and open asphalt mixtures*. American Association of State Highway and Transportation Officials.

AASHTO. (1993). *AASHTO guide for design of pavement structures*. American Association of State Highway and Transportation Officials.

AASHTO. (2022). *AASHTO T 342-22: Standard method of test for determining dynamic modulus of hot mix asphalt (HMA)*. American Association of State Highway and Transportation Officials. https://img.antpedia.com/standard/files/pdfs_ora/20230616/AASHTO/AASHTO%20T%20342-22.pdf

Alphones, A., Vilathgamuwa, D. M., Ong, A., Sampath, J. P. K., & Nguyen, X. B. (2014). *Coil enhancements for high efficiency wireless power transfer applications*. Institute of Electrical and Electronics Engineers.

ASTM. (2022a). *ASTM C39: Standard test method for compressive strength of cylindrical concrete specimens*. ASTM International.

ASTM. (2022b). *ASTM C78: Standard test method for flexural strength of concrete (using simple beam with third-point loading)*. ASTM International.

ASTM. (2022c). *ASTM D4541-22: Standard test method for pull-off strength of coatings using portable adhesion tester*. ASTM International.

Bi, Z., Kan, T., Chris Mi, C., Zhang, Y., Zhao, Z., & Keoleian, G. (2016). A review of wireless power transfer for electric vehicles: Prospects to enhance sustainable mobility. *Applied Energy*, *179*, 413–425.

Bosshard, R., & Kolar, J. (2016). *Inductive power transfer for electric vehicle charging: Technical challenges and tradeoffs*. Institute of Electrical and Electronics Engineers.

Brecher, A., & Arthur, D. (2014, August). *Review and evaluation of wireless power transfer (WPT) for electric transit application* (FTA Report No. 0060). https://www.transit.dot.gov/sites/fta.dot.gov/files/FTA_Report_No._0060.pdf

Brovont, A. D., Aliprantis, D., Pekarek, S. D., Agostino, A., & Haddad, D. (2022). Design and analysis of a three-phase dynamic wireless power transfer system for heavy-duty electric vehicles considering misalignment. *2022 Wireless Power Week (WPW)* (pp. 867–872).

Brovont, A., Aliprantis, D., Pekarek, S., Vickers, C., & Mehar, V. (2023). *Magnetic design for three-phase dynamic wireless power transfer with constant output power*. Institute of Electrical and Electronics Engineers.

Brown, W. C. (1996). The history of wireless power transmission. *Solar Energy*, *56*(1), 3–21.

Budhia, M., Boys, J. T., Covic, G. A., & Huang, C.-Y. (2011). *Development of a single-sided flux magnetic coupler for electric vehicle IPT charging systems*, *60*(1), 318–328. Institute of Electrical and Electronics Engineers.

Chen, F. (2016). *Sustainable implementation of electrified roads: Structural and material analyses* [Doctoral dissertation, KTH Royal Institute of Technology].

Chen, F., Baileu, R., Córdoba, E., & Kringos, N. (2019). Towards an understanding of the structural performance of future electrified roads: a finite element simulation study. *International Journal of Pavement Engineering*, *20*(2), 204–215.

Chen, F., Balieu, R., & Kringos, N. (2016). Potential influences on long term service performance of road infrastructure by automated vehicles. *Transportation Research Record Journal of the Transportation Research Board*, *2550*(1), 72–79.

Covic, G. A., & Boys, J. T. (2013). Inductive power transfer. *Proceedings of the IEEE*, *101*(6), 1276–1289. https://doi.org/10.1109/JPROC.2013.2244536

Cox, B., Mutel, C. L., Bauer, C., Beltran, A. M., & van Vuuren, D. P. (2018). Uncertain environmental footprint of current and future battery electric vehicles. *Environmental Science & Technology*, *52*(8), 4989–4995.

El-Shahat, A., Ayisire, E., Wu, Y., Rahman, M., & Nelms, D. (2019). Electric vehicles wireless power transfer state-of-the-art. *Energy Procedia*, *162*, 24–37.

Haddad, D., Konstantinou, T., Aliprantis, D., Gkritza, K., Pekarek, S., & Haddock, J. E. (2022). Analysis of the financial viability of high-powered electric roadways: A case study for the state of Indiana. *Energy Policy*, *171*, 113275.

Huang, Y. H. (1993). *Pavement analysis and design*. Pearson.

ICCS. (2014). *FABRIC (FeAsiBility analysis and development of on-road charging solutions for future electric vehiCles*. ICCS.

IEA. (2020). *Innovation needs in the sustainable development scenario* [Webpage]. International Energy Agency. https://www.iea.org/reports/clean-energy-innovation/innovation-needs-in-the-sustainable-development-scenario

IEA. (2021). *Global energy review 2021: Assessing the effects of economic recoveries on global energy demand and CO_2 emissions in 2021*. International Energy Agency. https://iea.blob.core.windows.net/assets/d0031107-401d-4a2f-a48b-9eed19457335/GlobalEnergyReview2021.pdf

IEA. (2022, May). *Global EV outlook 2022*. https://www.iea.org/reports/global-ev-outlook-2022

IEA. (2023, April). *Global EV outlook 2023*. International Energy Agency. https://www.iea.org/reports/global-ev-outlook-2023

Konstantinou, T., Haddad, D., Prasad, A., Wright, E., Gkritza, K., Aliprantis, D., Pekarek, S., & Haddock, J. E. (2021). *Feasibility study and design of in-road electric vehicle charging technologies* (Joint Transportation Research Program Publication No. FHWA/IN/JTRP-2021/25). West Lafayette, IN: Purdue University. https://doi.org/10.5703/1288284317353

Ledesma, E. C. (2015). *Analysis of effects and consequences of constructing inductive power transfer systems in road infrastructure* [Master's Thesis, KTH Royal institute of Technology]. https://kth.diva-portal.org/smash/get/diva2:902110/FULLTEXT01.pdf

Magment. (2016). *Concrete binded magnets for large power inductors*, *3*, 30–31. http://www.power-mag.com/pdf/feature_pdf/1466000647_Magment_Feature.pdf

Majhi, R., Ranjitkar, P., Sheng, M. S., & Covic, G. A. (2020). *A systematic review of dynamic wireless charging infrastructure location problem for electric vehicles*.

Miller, J. M., Jones, P. T., Li, J. M., & Onar, O. C. (2015). *ORNL experience and challenges facing dynamic wireless power charging of EVs*, *15*(2), 40–53.

Nantung, T. E., Lee, J., Haddock, J. E., Pouranian, M. R., Alvarez, D. B., Jeon, J., Shin, B., & Becker, P. J. (2021). *Structural evaluation of full-depth flexible pavement using APT* (Joint Transportation Research Program Publication No. FHWA/IN/JTRP-2021/17). West Lafayette, IN: Purdue University. https://doi.org/10.5703/1288284317319

NCHRP. (2004, March). *Guide for mechanistic-empirical design of new and rehabilitated pavement structures*. National Cooperative Highway Research Program.

Olson, O. (2013). *Slide-in electric road system, inductive project report, phase 1*. Viktoria Swedish ICT.

Paoli, L., & Gül, T. (2022, January 30). *Electric cars fend off supply challenges to more than double global sales.* International Energy Agency. https://www.iea.org/commentaries/electric-cars-fend-off-supply-challenges-to-more-than-double-global-sales

Peters, D. R., Schnell, J. L., Kinney, P. L., Naik, V., & Horton, D. E. (2020). Public health and climate benefits and trade-offs of U.S. vehicle electrification. *GeoHealth*, *4*(10). https://doi.org/10.1029/2020GH000275

Popovic, Z. (2017). *Near and far field wireless power transfer*. Institute of Electrical and Electronics Engineers.

Systems Control Technology, Inc. (1994). *Roadway powered electric vehicle project: track construction and testing program, Phase 3D*. California PATH Program.

Tesla, N. (1904, June 4). The transmission of electric energy without wires. *Scientific American Supplement*, *57*(1483), 23760–23763. https://www.scientificamerican.com/issue/supplements/1904/06-04/

Unplugged. (2015). *Unplugged: Wireless charging for electric vehicles* https://cordis.europa.eu/project/id/314126/reporting

U.S. Department of Energy. (2021). *Alternative fuels data center*. Energy Efficiency & Renewable Energy. https://afdc.energy.gov/vehicles/electric_emissions.html

U.S. EPA. (2024). *Sources of greenhouse gas emissions* [Webpage]. Retrieved on June 5, 2024, from https://www.epa.gov/ghgemissions/sources-greenhouse-gas-emissions

Van Mulders, J., Delabie, D., Lecluyse, C., Buyle, C., Callebaut, G., Van der Perre, L., & De Strycker, L. (2022, August). Wireless power transfer: Systems, circuits, standards, and use cases. *Sensors*, *22*(15), 5573.

Villa, J. L., Sallán, J., Llombart, A., & Sanz, J. F. (2009). Design of a high frequency inductively coupled power transfer system for electric vehicle battery charge. *Applied Energy*, *86*(3), 355–363.

Witczak, M. W., Kaloush, K., Pellinen, T., El-Basyouny, M., & Von Quintus, H. (2002). *Simple performane test for superpave mix design* (NCHRP Report 465). Transportation Research Board.

Yozwiak, M., Carley, S., & Konisky, D. M. (2022, June). *Clean and just: Electric vehicle innovation to accelerate more equitable early adoption.* Information Technology & Innovation Foundation. https://www2.itif.org/2022-accelerating-ev-adoption.pdf

About the Joint Transportation Research Program (JTRP)

On March 11, 1937, the Indiana Legislature passed an act which authorized the Indiana State Highway Commission to cooperate with and assist Purdue University in developing the best methods of improving and maintaining the highways of the state and the respective counties thereof. That collaborative effort was called the Joint Highway Research Project (JHRP). In 1997 the collaborative venture was renamed as the Joint Transportation Research Program (JTRP) to reflect the state and national efforts to integrate the management and operation of various transportation modes.

The first studies of JHRP were concerned with Test Road No. 1—evaluation of the weathering characteristics of stabilized materials. After World War II, the JHRP program grew substantially and was regularly producing technical reports. Over 1,600 technical reports are now available, published as part of the JHRP and subsequently JTRP collaborative venture between Purdue University and what is now the Indiana Department of Transportation.

Free online access to all reports is provided through a unique collaboration between JTRP and Purdue Libraries. These are available at http://docs.lib.purdue.edu/jtrp.

Further information about JTRP and its current research program is available at http://www.purdue.edu/jtrp.

About This Report

An open access version of this publication is available online. See the URL in the citation below.

Moncada, O. A., Imran, Z., Vickers, C., Gkritza, K., Pekarek, S., Aliprantis, D., Brovont, A., Jahangiri, B., & Haddock, J. E. (2024). *Full-scale dynamic wireless power transfer and pilot project implementation* (Joint Transportation Research Program Publication No. FHWA/IN/JTRP-2024/11). West Lafayette, IN: Purdue University. https://doi.org/10.5703/1288284317744